# Evidence for eccentricity in the population of binary black holes observed by LIGO-Virgo-KAGRA

Nihar Gupte,[1,2] Antoni Ramos-Buades,[3,1] Alessandra Buonanno,[1,2] Jonathan Gair,[1] M. Coleman Miller,[4] Maximilian Dax,[5] Stephen R. Green,[6] Michael Pürrer,[7,8] Jonas Wildberger,[5] Jakob Macke,[5] Isobel M. Romero-Shaw,[9,10] and Bernhard Schölkopf[5]

[1]*Max Planck Institute for Gravitational Physics (Albert Einstein Institute), Am Mühlenberg 1, Potsdam 14476, Germany*
[2]*Department of Physics, University of Maryland, College Park, Maryland 20742, USA*
[3]*Nikhef, Science Park 105, 1098 XG Amsterdam, The Netherlands*
[4]*Department of Astronomy and Joint Space-Science Institute, University of Maryland, College Park, Maryland 20742, USA*
[5]*Max Planck Institute for Intelligent Systems, Max-Planck-Ring 4, 72076 Tübingen, Germany*
[6]*School of Mathematical Sciences, University of Nottingham, University Park, Nottingham NG7 2RD, United Kingdom*
[7]*Department of Physics, East Hall, University of Rhode Island, Kingston, Rhode Island 02881, USA*
[8]*Center for Computational Research, Carothers Library, University of Rhode Island, Kingston, Rhode Island 02881, USA*
[9]*Department of Applied Mathematics and Theoretical Physics, Cambridge CB3 0WA, United Kingdom*
[10]*Kavli Institute for Cosmology Cambridge, Madingley Road, Cambridge CB3 0HA, United Kingdom*

(Received 6 June 2024; accepted 19 September 2025; published 17 November 2025)

Binary black holes (BBHs) in eccentric orbits produce distinct modulations in the emitted gravitational waves (GWs). The measurement of orbital eccentricity can provide robust evidence for dynamical binary formation channels. We analyze 57 GW events from the first, second, and third observing runs of the Laser Interferometer Gravitational-Wave Observatory (LIGO)-Virgo-Kamioka Gravitational Wave Detector (KAGRA) (LVK) Collaboration using a multipolar aligned-spin inspiral-merger-ringdown waveform model with two eccentric parameters: eccentricity and relativistic anomaly (assuming a quasicircular merger-ringdown). This is made computationally feasible with the machine-learning code Dingo, which accelerates inference by 2–3 orders of magnitude compared to traditional inference techniques. First, when using a uniform prior on the eccentricity, we find eccentric aligned-spin against quasicircular aligned-spin $\log_{10}$ Bayes factors of 1.84 to 4.75 (depending on the glitch mitigation) for GW200129, 3.0 for GW190701 and 1.77 for GW200208_22. We infer $e_{\mathrm{gw,10\ Hz}}$ ($e_{\mathrm{gw,20\ Hz}}$) to be $0.27^{+0.10}_{-0.12}$ ($0.16^{+0.04}_{-0.05}$) to $0.17^{+0.14}_{-0.13}$ ($0.1^{+0.05}_{-0.04}$) for GW200129, $0.54^{+0.12}_{-0.30}$ ($0.31^{+0.12}_{-0.13}$) for GW190701 and $0.39^{+0.23}_{-0.23}$ ($0.21^{+0.08}_{-0.08}$) for GW200208_22. Second, we find $\log_{10}$ Bayes factors between the eccentric aligned-spin versus quasicircular precessing-spin hypothesis between 1.43 and 4.92 for GW200129, 2.61 for GW190701 and 1.23 for GW200208_22. Third, our analysis does not show evidence for eccentricity in GW190521, which has an eccentric aligned-spin against quasicircular aligned-spin $\log_{10}$ Bayes factor of 0.04. Fourth, we estimate that if we neglect the spin-precession and use an astrophysically motivated prior on the rate of eccentric BBHs, the probability of one out of the 57 events being eccentric is greater than 99.5% or $(100 - 8.4 \times 10^{-4})\%$ (depending on the glitch mitigation). Fifth, we study the impact on parameter estimation when neglecting either eccentricity in quasicircular models or higher modes in eccentric models for GW events. These results underscore the importance of including eccentric parameters in the characterization of BBHs for the upcoming observing runs of the LVK Collaboration and for future detectors on the ground and in space, which will probe a more diverse BBH population.

DOI: 10.1103/vpyp-nvfp



## I. INTRODUCTION

Gravitational waves (GWs) have been a gold mine for astrophysical characterization and discovery since the first detection in 2015 [1–12]. They are a clean probe for binary black holes (BBHs) due to their weak interaction with matter.

GWs have been used to infer the masses, spins [13–19] eccentric parameters [20–24], and test general relativity (GR) [25–30]. BBH properties are important as they can give insight into the binary's formation channels [31–36].

While stellar-mass black holes (BHs) form from the collapse of stars with masses $\gtrsim 20M_\odot$ [37–39], and primordial BHs may form from overdense regions in the early Universe [40], the formation of a BBH is not trivial. One cannot assume that all stellar binaries will become BBHs. If the initial separation of two $\sim 10M_\odot$ compact objects in a quasicircular orbit is greater than $\sim 20R_\odot$, then they will not merge in a Hubble time ($\sim$14 Gyr) from gravitational radiation alone [41]. However, if the initial separation of this binary is less than $\sim 20R_\odot$, the stars merge before forming BHs (see, e.g., Figs. 1 and 2 in Ref. [42]).

Thus, to explain the formation of BBHs, two classes of formation mechanisms of BBHs have been proposed in the literature: isolated binary evolution and dynamical formation. Within these categories, the former has subchannels including common-envelope evolution [39,43–49], chemically homogenous evolution [50,51] and Population III stars [52]. Similarly, the dynamical channel has subchannels, e.g., binaries arising from triple interactions [53–57], von Zeipel-Lidov-Kozai oscillations [58–63], binary-binary interactions [64], and binary-single interactions [65,66]. These possibilities were proposed in Refs. [67–74], and further investigated in Refs. [75–82]

It is unclear what fraction of BBHs arise from each formation channel. Multiple channels may operate simultaneously, making the origin of BBHs even harder to pinpoint. But measuring eccentricity in a BBH can serve as a reliable indicator of a dynamical formation channel [63]. This is because isolated binaries that are initially eccentric would circularize by the time they enter the LIGO-Virgo-KAGRA (LVK) band [41]. So by studying the effect of eccentricity, we can help discriminate what fraction of BBHs originate from dynamical interactions or isolated binary (IB) evolution [31].

There is also good reason to believe we may observe a few eccentric events in the LVK observing runs [7,11,12] or future GW observatories, such as the Einstein Telescope [83], Cosmic Explorer [84] and Laser Interferometer Space Antenna (LISA) [85]. For instance, there have been robust simulations performed to determine the expected number of BBHs from the dynamical-formation channel. Simulations which include the post-Newtonian (PN) description of the orbital dynamics in globular star clusters show that $\approx 5\%$ of dynamical mergers have eccentricities greater than 0.1. This estimate refers to an astrophysical definition of eccentricity [63,86], not the quasi-Keplerian definition at 10 Hz (in the detector frame) [65,87,88]. Estimates from galactic nuclei predict higher rates of eccentricity with up to 70% of mergers predicted
to have eccentricities larger than 0.1 at 10 Hz [89–91]. These high eccentricity mergers could be detected by upcoming runs of the LVK Collaboration. It is then important to have an eccentric waveform model to analyze the data.

Taking eccentricity into account is also important, as ignoring it can lead to systematic biases in parameter estimation [24,92–103]. So far, eccentric waveform models have not been used for analysis of the LVK GW transient catalogs [1–4]. This limitation may cause biases and have implications on hierarchical BBH population studies and tests of GR [104–109].

Several parameter-estimation studies that included one eccentric parameter in the waveform model have been carried out in the last few years [20–23,95,97,100,110–112]. There have also been parameter estimation studies that use two parameters to explore the effect of eccentricity [24,94,113]. In particular, the authors of Ref. [94] performed inference by fixing the binary at apastron and sampling on the initial eccentricity and the average starting frequency between apastron and periastron. On the other hand, Ref. [24] fixes the orbit averaged starting frequency and samples directly on the relativistic anomaly and the eccentricity. We note that sampling on starting frequency and eccentricity at fixed relativistic anomaly may not be equivalent to sampling on eccentricity and relativistic anomaly at a fixed starting frequency. In principle, these methods can probe the same parameter space. However, if sampling on the starting frequency, one has to choose arbitrary prior bounds on the starting frequency. If there are templates with a better match to the GW outside of these bounds, this method does not cover the same parameter space as the method which fixes the starting frequency and samples on the relativistic anomaly and eccentricity. In addition, sampling on the starting frequency will change the reference point where the binary properties, such as the reference phase, are measured. Finally, Ref. [113] samples on the energy and angular momentum of the binary at a fixed instantaneous starting frequency. We note that whereas Ref. [24] deals with (bound) eccentric orbits, Ref. [113] focuses on hyperbolic orbits. During the referee period of this paper, there have been even more studies with eccentric waveform models, including Refs. [114–116].

Due to the computational cost, the aforementioned analyses were restricted to either sampling on noneccentric parameters and reweighting with eccentric models, or to a small number of GW events when using Bayesian methods that sample directly on the eccentric parameters. Here, we employ the Deep INference for Gravitational-wave Observations (Dingo) code to sample a large number of GW events. As in Refs. [24,94], we perform inference on the two eccentric parameters: eccentricity and relativistic anomaly. This is important, as ignoring the relativistic anomaly can lead to biases in parameter estimation [24,117]. Dingo has already been used to analyze a subset of the spin-precessing BBHs in the first and third observing runs [118]. Remarkably, Dingo yields posterior distributions within $\mathcal{O}$(min-hours) without sacrificing accuracy [118,119]. However, it is currently limited to GW signals shorter than 16 sec.

In this study, we employ a set of waveform models from the effective-one-body (EOB) family SEOBNR. We use the multipolar aligned-spin quasicircular model SEOBNRv4HM [120,121] and the multipolar aligned-spin eccentric model SEOBNRv4EHM [122,123] to analyze 57 GW events from the first (O1), second (O2) and third (O3) observing runs of the LVK Collaboration [4,124,125]. We find $\log_{10}$ Bayes factors, between the eccentric against quasicircular hypothesis, greater than 1 for three events. We also do a comprehensive study to understand the impact of glitch subtraction for one of the GW events (GW200129), which happens to be the BBH with the largest evidence for eccentricity. Confirming the recent results in Ref. [24], we do not find evidence for eccentricity in GW190521, which previous analyses had suggested to be eccentric [21,110].

It has been suggested that for some regions of the parameter space, and at certain stages of the coalescence, spin-precession can be mistaken for eccentricity in parameter-estimation studies [126,127]. Thus, for comparison, we also employ two multipolar spin-precessing waveform models for quasicircular orbits. One is from the EOB waveform family, SEOBNRv4PHM [128–131], and the other is from the numerical-relativity surrogate family, NRSur7dq4 [132]. Unfortunately, inspiral-merger-ringdown waveform models with spin-precession and eccentricity are not yet available, with the exception of the recent Ref. [133], whose code is not available to us. We also explore the impact of ignoring eccentricity and higher harmonics in parameter estimation.

When trying to determine if a BBH is eccentric, we must also consider the relative merger rates of eccentric and quasicircular BBHs. This can be done by incorporating astrophysical knowledge from N-body simulations or semianalytic calculations. We can also directly infer the rates from the GW data. In this paper, we combine both approaches to first generate a prior on the rate of eccentric and quasicircular BBHs based on results from the literature, and then incorporate GW information. This results in a new way to quantify the probability that a GW comes from an eccentric BBH, similar to the $p_{\rm astro}$ reported in LVK analyses [134]. This approach also allows us to quantify the probability of eccentricity in the population of BBHs.

The paper is organized as follows: in Sec. II, we give an overview of the Bayesian inference techniques used in this study. In particular, in Sec. II A we discuss Bayes theorem and how to compute odds ratios, in Sec. II B we compute the probability a GW signal is eccentric based on the ensemble of events, and in Sec. II C we review the machine-learning code Dingo. In Sec. III, we introduce the waveform models used in this paper, and review the method introduced in Refs. [135,136] to infer eccentricity directly from the waveform. Furthermore, in Sec. IV A we discuss the settings of the trained networks and priors employed in the Dingo analysis, while in Sec. IV B we validate the neural networks with zero-noise synthetic signals and comparisons to parallel Bilby (pBilby) [137]. From Secs. IV C through IV F, we present the analysis of 57 GWs and discuss in depth the events that support eccentricity. In Secs. V A and V B, we investigate the impact on parameter estimation of neglecting eccentricity and higher modes in waveform models, respectively. In Sec. VI A, we incorporate astrophysical BBH merger-rate estimates of eccentric and quasicircular events into our analysis, while in Sec. VI B, we estimate the probability of GW signals being eccentric and the probability that eccentricity exists in the population of GWs analyzed. In Sec. VII, we summarize our main conclusions, comparing our results with the literature and suggesting future work. In Appendix A, we perform analyses of GW200129 using either only the LIGO-Hanford or the LIGO-Livingston detector. In Appendix B, we describe a method to compute the probability there exists an eccentric event in the ensemble of GWs analyzed. In Appendix C, we do full parameter estimation and recover the Bayesian evidence of more than 500 injections drawn from an astrophysical distribution to assess the significance of our Bayes factors. In Appendix D, we show agreement between Dingo and pBilby for an eccentric injection in simulated Gaussian noise. In Appendix E, we present the kick velocity posterior distribution of GW200129 when using the multipolar aligned-spin eccentric model SEOBNRv4EHM, and compare it to results using the multipolar spin-precessing quasicircular model NRSur7dq4. In Appendix F, we explore the effect of the Occam penalty when comparing eccentric aligned-spin and quasicircular spin-precessing approximants. Lastly, in Appendix G, we present the results of synthetic-signal injections aimed at determining if eccentricity could be mistaken for spin-precession in GW200129. In Appendix H, we show a table of the events analyzed along with their Bayes factors and probabilities of being eccentric.

In this paper, we use natural units, and set $G = c = 1$ unless otherwise specified. Individual component masses are denoted $m_1$, $m_2$, while the total mass is $M \equiv m_1 + m_2$, and the chirp mass is $\mathcal{M} = (m_1 m_2)^{3/5} M^{-1/5}$. We use the convention, $q \equiv m_2/m_1 \leq 1$, and define $\mu \equiv m_1 m_2/M$ and $\nu \equiv \mu/M$. We quote the masses in both the source and detector frame denoting them as $M_{\rm src} \equiv M$ and $M_{\rm det} \equiv M(1+z)$, respectively. Here $z$ is the redshift of the source.

Although we mostly consider BHs with spins $\boldsymbol{S_{1,2}}$ aligned (or antialigned) with the direction perpendicular to the orbital plane, we also carry out a few studies with spin-precessing BHs. Thus, generically, we introduce the dimensionless spin

$$\chi_i \equiv \frac{\boldsymbol{S_i} \cdot \hat{\boldsymbol{L}}}{m_i^2} i = 1, 2, \tag{1.1}$$

which takes values in the range $[-1, +1]$, where $\hat{\boldsymbol{L}}$ is the unit vector pointing in the direction perpendicular to the instantaneous orbital plane. In parameter estimation, one often uses $\chi_{\rm eff}$, as it is better constrained [138–141]. This is defined as

$$\chi_{\rm eff} \equiv \frac{m_1\chi_1 + m_2\chi_2}{M}. \tag{1.2}$$

Similarly, we use the effective precession parameter $\chi_p$ defined in Ref. [142]:

$$\chi_p \equiv \frac{\max(A_1 S_{1,\perp}, A_2 S_{2,\perp})}{A_1 m_1^2}, \tag{1.3}$$

where $A_1 = 2 + 3/(2q)$ and $A_2 = 2 + 3/(2q)$, and $S_{i,\perp}$ is the magnitude of the in plane spins. That is, $S_{i,\perp} = |\boldsymbol{S_i} - \boldsymbol{S_i}\cdot\boldsymbol{L}|$, where $\boldsymbol{L}$ is the orbital angular momentum. We also introduce the total angular momentum $\boldsymbol{J} = \boldsymbol{L} + \boldsymbol{S}_1 + \boldsymbol{S}_2$.

We denote $\boldsymbol{\vartheta}$ as the set of all GW parameters, including intrinsic parameters of the source and the extrinsic parameters related to projection of the waveform onto the detector. In the case of eccentric aligned-spin binaries, we have 13 parameters $\boldsymbol{\vartheta} = \{\mathcal{M}, q, \chi_1, \chi_2, e, \zeta, \alpha, \delta, d_{\rm L}, t_{\rm coal}, \iota, \psi, \phi_{\rm coal}\}$. In the case of quasicircular precessing-spin binaries, we have 15 parameters $\boldsymbol{\vartheta} = \{\mathcal{M}, q, |\chi_1|, |\chi_2|, \theta_1, \theta_2, \phi_{\rm JL}, \phi_{12}, \alpha, \delta, d_{\rm L}, t_{\rm coal}, \theta_{\rm JN}, \psi, \phi_{\rm coal}\}$.

We indicate with $e$ the eccentricity and with $\zeta$ the relativistic anomaly, which are defined more precisely in Sec. III. The parameters $\{|\chi_1|, |\chi_2|, \theta_1, \theta_2, \phi_{\rm JL}, \phi_{12}\}$ describe the (dimensionless) spin values, spin tilts, the angle between the total and orbital angular momentum, and the angle between the spins of the BHs, respectively [143]. The rest are extrinsic parameters with $\alpha$ the right ascension, $\delta$ the declination, $d_{\rm L}$ the luminosity distance, $t_{\rm coal}$ the time of coalescence, $\theta_{\rm JN}$ the angle between the total angular momentum and the line of sight of the observer, $\iota$ the angle between the orbital angular momentum and the line of sight of the observer, $\psi$ the polarization angle between the GW and detectors, and $\phi_{\rm coal}$ the orbital reference phase at coalescence (e.g., see Figs. 1–3 in Ref. [144] for a diagram, and Eqs. (17)–(20) in Ref. [145] for how the extrinsic parameters enter the detector projections).

In the following, we assume the *Planck* 2015 cosmology [146].

## II. BAYESIAN INFERENCE

In this section, we outline how Bayesian inference can be used to determine if a detected GW event is more likely to be described by a BBH moving on an eccentric or quasicircular orbit. The approach is to first compute posterior distributions for individual events, then to use these posteriors to compute Bayes factors and finally weight these Bayes factors by astrophysical information to calculate the probability that a BBH is eccentric.

### A. Bayes theorem, Bayes factor, and odds ratios

Here, we summarize the basics of the Bayesian inference formalism used in GW astronomy. In doing so, we also introduce the concepts of Bayes factors and odds ratios.

Our hypothesis, $\mathcal{H}_a$, is that in the detector data, $d$, an observed GW signal is described by a waveform model, $a$, with parameters $\boldsymbol{\vartheta}_a$. The posterior probability distribution on the parameters of the model, $\boldsymbol{\vartheta}_a$, given the hypothesis, $\mathcal{H}_a$, is obtained using Bayes' theorem, as follows:

$$p(\boldsymbol{\vartheta}_a|d,\mathcal{H}_a) = \frac{p(d|\boldsymbol{\vartheta}_a,\mathcal{H}_a)p(\boldsymbol{\vartheta}_a|\mathcal{H}_a)}{p(d|\mathcal{H}_a)}. \tag{2.1}$$

Here, $p(\boldsymbol{\vartheta}_a|\mathcal{H}_a)$ is the prior probability distribution, $p(d|\boldsymbol{\vartheta}_a,\mathcal{H}_a)$ is the likelihood function, and $p(d|\mathcal{H}_a)$ is the evidence of the hypothesis $\mathcal{H}_a$. In this study, we compute most of the posterior distributions with Dingo (see Sec. II C). We also compute a few posteriors with pBilby [137] for validation and comparison.

For a detector with stationary, Gaussian noise, we use the likelihood function

$$p(d|\boldsymbol{\vartheta}_a,\mathcal{H}_a) \propto \exp\left[-\frac{1}{2}\langle d - h_a(\boldsymbol{\vartheta}_a)|d - h_a(\boldsymbol{\vartheta}_a)\rangle\right], \tag{2.2}$$

where $h_a$ is the GW signal generated by waveform model $a$, and the brackets denote the noise-weighted inner product,

$$\langle A|B\rangle = 2\int_{f_{\rm low}}^{f_{\rm high}} df \frac{\tilde{A}^*(f)\tilde{B}(f) + \tilde{A}(f)\tilde{B}^*(f)}{S_n(f)}. \tag{2.3}$$

Here, $\tilde{A}(f)$ is the Fourier transform of $A(t)$, the asterisk denotes the complex conjugation, and $S_n(f)$ is the one-sided power spectral density (PSD) of the detector. The integration limits $f_{\rm low}$ and $f_{\rm high}$ are set by the bandwidth of the detector's sensitivity.

When trying to estimate whether the GW event is eccentric or quasicircular, we compute the odds ratio $\mathcal{O}_{a/b}$ between the two hypotheses, $\mathcal{H}_a$ and $\mathcal{H}_b$, which is given by

$$\mathcal{O}_{a/b} = \frac{p(\mathcal{H}_a)}{p(\mathcal{H}_b)}\frac{p(d|\mathcal{H}_a)}{p(d|\mathcal{H}_b)} \equiv \frac{R_a}{R_b}\mathcal{B}_{a/b}. \tag{2.4}$$

The first ratio in the product is the *priors odds*, which represent our belief about the Universe prior to observing any GW data. It can be determined through astrophysical simulations or other non-GW observations.[1] The second term is the *Bayes factor*, which is the odds of the hypotheses given the data.[2]

[1] If we were only analyzing a subset of GW events, we could also use the rate estimates from previous GW observing runs to determine the rates (and thus) prior odds.

[2] Note these Bayes factors are defined differently from Ref. [20] and cannot directly be compared. The Bayes factor in Eq. (2.4) will be conservative (smaller) compared to the $e_{10\ \rm Hz} < 0.05$ versus $e_{10\ \rm Hz} > 0.05$ Bayes factor considered in Ref. [20].

In this study, we consider the eccentric aligned-spin (EAS) versus quasicircular aligned-spin (QCAS) odds ratio ($\mathcal{O}_{\mathrm{EAS/QCAS}}$), for which we need to compute the merger rate of eccentric events $R_{\mathrm{E}}$ and quasicircular events $R_{\mathrm{QC}}$. We do not consider the eccentric aligned-spin versus quasicircular precessing odds ratio as to our knowledge no rate estimates (and thus prior odds) for this fraction exist in the literature.

### B. Probability a GW event is eccentric

To determine the odds ratio (2.4), one needs to include the priors odds, i.e., some astrophysical information. But the odds ratio does not account for the fact that we have analyzed many GW events, and therefore have information about the rates directly from GW observations. Therefore, we propose an alternate way to measure the probability that an event is eccentric. This method is analogous to the way that the LVK Collaboration reports the probability that a GW detection is of astrophysical origin, with the so-called $p_{\mathrm{astro}}$ [134]. It relies on the formalism derived in Ref. [134]. This method has three advantages over just computing the odds ratio.

(1) When computing the merger rates in Eq. (2.4), we are essentially drawing from a prior distribution, $p(R_{\mathrm{E}}, R_{\mathrm{QC}})$, which is motivated by astrophysics. However, the astrophysical prior has a large variance. With an increasing number of GW events, we can begin constraining the prior on the rates from observations.
(2) We can naturally incorporate selection effects which are not included when considering the ratio between eccentric and quasicircular BBH rates in Eq. (2.4).
(3) We can compute the probability that eccentric events exist in the population of GWs analyzed so far without referring to a specific event.

We now review the formalism of Ref. [134] and show how it can be used to derive the probability that an event is eccentric. Let $\{d_i\}$ be the collection of strain data segments of GW triggers. We assign each event a flag, $g_i$, which is 1 if the event is eccentric and 0 if the event is quasicircular. Our goal is to obtain the probability distribution over the set of flags, $\{g_i\}$. Let $N$ be the number of events. According to Bayes' theorem, the posterior distribution over the flags is

$$p(\{g_i\}, R_{\mathrm{E}}, R_{\mathrm{QC}}|\{d_i\}, N) = \frac{p(\{d_i\}|\{g_i\}, N, R_{\mathrm{E}}, R_{\mathrm{QC}})\, p(\{g_i\}, N, R_{\mathrm{E}}, R_{\mathrm{QC}})}{p(\{d_i\}, N)}. \tag{2.5}$$

Let us recover an expression for the likelihood term, $p(\{d_i\}|\{g_i\}, N, R_{\mathrm{E}}, R_{\mathrm{QC}})$. The probability that the data segment $d_i$ is from an eccentric BBH is

$$Z_{\mathrm{E}}(d_i) \equiv p(d|\mathcal{H}_{\mathrm{E}}) = \int d\boldsymbol{\vartheta}\, p(d|\boldsymbol{\vartheta}, \mathcal{H}_{\mathrm{E}})\, p(\boldsymbol{\vartheta}|\mathcal{H}_{\mathrm{E}}). \tag{2.6}$$

Here the "E" subscript indicates that an eccentric model is being used. Similarly, $Z_{\mathrm{QC}}(d_i)$ is the probability that $d_i$ is generated by from a quasicircular BBH. This is given by Eq. (2.6), but using the quasicircular waveform, which we denote as "QC." Thus, we can write the likelihood as

$$p(\{d_i\}|\{g_i\}, N, R_{\mathrm{E}}, R_{\mathrm{QC}}) = \left[\prod_{\{i|g_i=1\}}^{N_{\mathrm{E}}} Z_{\mathrm{E}}(d_i)\right]\left[\prod_{\{i|g_i=0\}}^{N_{\mathrm{QC}}} Z_{\mathrm{QC}}(d_i)\right]. \tag{2.7}$$

Here, the conditioning on the rates does not enter the expression for the rate likelihood. Note that we are only using aligned-spin evidences in the above rate likelihood and not considering spin-precessing evidences. We leave extending these results to the spin-precessing case for future work.

The prior distribution in Eq. (2.5) can be factorized exactly the same way as Eqs. (13)–(17) in Ref. [134]. For completeness, we include the final expression here:

$$p(\{g_i\}, R_{\mathrm{E}}, R_{\mathrm{QC}}, N) = R_{\mathrm{E}}^{N_{\mathrm{E}}} R_{\mathrm{QC}}^{N_{\mathrm{QC}}} \frac{e^{-(R_{\mathrm{E}}+R_{\mathrm{QC}})}}{N!}\, p(R_{\mathrm{E}}, R_{\mathrm{QC}}), \tag{2.8}$$

where $N_{\mathrm{E}} = \sum_i g_i$ and $N_{\mathrm{QC}} = \sum_i (1 - g_i) = N - N_{\mathrm{E}}$. The last term in Eq. (2.8) is the prior over the rates. This can either be a uniform prior or an astrophysical prior from the literature. We discuss the derivation of an astrophysical prior on the rates in Sec. VI A. The exponential term comes from the Poisson uncertainty on the number of events [125]. Substituting the likelihood and prior term into Eq. (2.5), our posterior over the flags and rates becomes

$$p(\{g_i\}, R_{\mathrm{E}}, R_{\mathrm{QC}}|\{d_i\}, N) \propto \left[\prod_{\{i|g_i=1\}}^{N_{\mathrm{E}}} R_{\mathrm{E}} Z_{\mathrm{E}}(d_i)\right]\left[\prod_{\{i|g_i=0\}}^{N_{\mathrm{QC}}} R_{\mathrm{QC}} Z_{\mathrm{QC}}(d_i)\right] \times e^{-(R_{\mathrm{E}}+R_{\mathrm{QC}})}\, p(R_{\mathrm{E}}, R_{\mathrm{QC}}), \tag{2.9}$$

where we have dropped the evidence term and the factorial, and replaced them with a proportionality. If we are only interested in an estimate for the rates, we can marginalize over the flags to get

$$p(R_{\mathrm{E}}, R_{\mathrm{QC}}|\{d_i\}, N) \propto \left[\prod_i R_{\mathrm{E}} Z_{\mathrm{E}}(d_i) + R_{\mathrm{QC}} Z_{\mathrm{QC}}(d_i)\right] e^{-(R_{\mathrm{E}}+R_{\mathrm{QC}})}\, p(R_{\mathrm{E}}, R_{\mathrm{QC}}). \tag{2.10}$$

To obtain the normalization of Eq. (2.10) we can numerically integrate over $R_{\rm E}$ and $R_{\rm QC}$.

Finally, we can compute the probability that the $m$th event is eccentric by marginalizing over the rates and all flags except the $m$th flag. This results in the expression

$$\begin{aligned} p_{\rm ecc}(m) &= p(g_m = 1|\{d_i\}, N) \\ &= \int dR_{\rm E} dR_{\rm QC} R_{\rm E} Z_{\rm E}(d_m) \\ &\quad \times \frac{p(R_{\rm E}, R_{\rm QC}|\{d_i\}, N)}{R_{\rm E} Z_{\rm E}(d_m) + R_{\rm QC} Z_{\rm QC}(d_m)}. \end{aligned} \tag{2.11}$$

We can gain intuition on this statistic by considering a limiting case which relates to the odds ratio. Suppose that the set of GW observations holds no information on $R_{\rm E}$ and $R_{\rm QC}$. This means that $p(R_{\rm E}, R_{\rm QC}|\{d_i\}, N) = p(R_{\rm E}, R_{\rm QC})$. We can define $(\tilde{R}_{\rm E}, \tilde{R}_{\rm QC}) = \text{argmax}\{p(R_{\rm E}, R_{\rm QC})\}$. That is, the pair $(\tilde{R}_{\rm E}, \tilde{R}_{\rm QC})$ are the merger rates for which the function $p(R_{\rm E}, R_{\rm QC})$ is maximized. In this context, $\tilde{R}_{\rm E}$ and $\tilde{R}_{\rm QC}$ are the rates we would use to estimate the odds ratio in Eq. (2.4). If we draw one sample from $p(R_{\rm E}, R_{\rm QC})$ to estimate Eq. (2.11), we will find the most likely estimate for $p_{\rm ecc}$ is

$$\begin{aligned} \tilde{p}_{\rm ecc}(m) &\equiv \frac{\tilde{R}_{\rm E} Z_{\rm E}(d_m)}{\tilde{R}_{\rm E} Z_{\rm E}(d_m) + \tilde{R}_{\rm QC} Z_{\rm QC}(d_m)} \\ &= \frac{\mathcal{O}_{\rm EAS/QCAS}}{1 + \mathcal{O}_{\rm EAS/QCAS}}. \end{aligned} \tag{2.12}$$

Thus, if we use the prior instead of the rate posterior in Eq. (2.11), $p_{\rm ecc}$ can be thought of as a mapping of the odds ratio to the interval [0, 1]. As more events are observed, $p(R_{\rm E}, R_{\rm QC}|\{d_i\}, N)$ becomes tighter than $p(R_{\rm E}, R_{\rm QC})$. This means we lose the large uncertainty due to the astrophysical uncertainty on the rates and get a better estimate on $p_{\rm ecc}$.

We can also compute the probability that there exists at least one eccentric event in the population of GW events analyzed so far. This can be done by defining

$$p_{\rm ecc,pop} \equiv 1 - p(\{g_i = 0\}|\{d_i\}, N). \tag{2.13}$$

That is, the probability there exists eccentricity in the population is one minus the probability that all events are quasicircular. This can be computed by marginalizing Eq. (2.9) over the rates and normalizing by the integral over the rates and flags. Explicitly,

$$p(\{g_i = 0\}|\{d_i\}, N) = \frac{\int dR_{\rm E} dR_{\rm QC} R_{\rm QC}^N \prod_i Z_{\rm QC}(d_i) e^{-(R_{\rm E}+R_{\rm QC})} p(R_{\rm E}, R_{\rm QC})}{\int dR_{\rm E} dR_{\rm QC} \prod_j [R_{\rm QC} Z_{\rm QC}(d_j) + R_{\rm E} Z_{\rm E}(d_j)] e^{-(R_{\rm E}+R_{\rm QC})} p(R_{\rm E}, R_{\rm QC})}. \tag{2.14}$$

To compute the normalizing factor (denominator) exactly we need to integrate over a product with many terms. We can instead compute the dominant terms of this integral to place a lower bound on the normalizing factor. This allows us to place an upper bound on $p(\{g_i = 0\}|\{d_i\}, N)$ thereby allowing us to place a lower bound on $p_{\rm ecc,pop}$. We discuss a method to compute the dominant terms in this integral in Appendix B.

Finally, we can incorporate selection effects into this framework. Selection effects occur because we do not observe every BBH in our prior. Low mass or high distance events may not have a high enough SNR to be seen by ground-based detectors. This has two effects on the likelihood in Eq. (2.7), which are derived in Ref. [147].

We define $\alpha_{\rm E}$ and $\alpha_{\rm QC}$ as the fraction of events in the Universe which would be detected under the eccentric and quasicircular hypotheses, respectively. Explicitly, $\alpha_E$ can be computed as

$$\alpha_{\rm E} = \int d\boldsymbol{\vartheta} p_{\rm E,det}(\boldsymbol{\vartheta}) p(\boldsymbol{\vartheta}|\mathcal{H}_E), \tag{2.15}$$

where $p_{\rm E,det}(\boldsymbol{\vartheta})$ is the probability of detecting a GW event with parameters $\boldsymbol{\vartheta}$ under the eccentric hypothesis. The computation for $\alpha_{\rm QC}$ is analogous except using $p_{\rm QC,det}(\boldsymbol{\vartheta})$ (the probability to detect an event with parameters $\boldsymbol{\vartheta}$ under the quasicircular hypothesis). We can compute $p_{\rm QC,det}$ and $p_{\rm E,det}$ using a threshold SNR and error functions [134].

In general, $p_{\rm E,det}$ and $p_{\rm QC,det}$ are different. This is because eccentric waveforms are not usually used for GW searches (see however, Refs. [148–151]). To compute $p_{\rm E,det}$ to a high accuracy, one would need to perform a suite of synthetic eccentric injections into the LVK detection pipelines and count the number of observed triggers [13]. Alternatively, one could compute the overlap between the eccentric signal and a quasicircular waveform maximizing over the parameters of the system. This was done in Ref. [31] for an eccentric nonspinning fiducial injection with $d_L = 1$ Gpc and $\mathcal{M} = 28M_\odot$ using the waveform model from Refs. [152–154]. The authors of Ref. [31] find that the deviation between $p_{\rm E,det}$ and $p_{\rm QC,det}$ is less than 0.05 at $e_{10\ \rm Hz}$ for this injection. However, we must exercise caution as $p_{\rm E,det}$ and $p_{\rm QC,det}$ will be different for different injection configurations. One could imagine GWs whose SNR is near the boundary of the threshold SNR for detection causing larger differences between $p_{\rm E,det}$ and $p_{\rm QC,det}$. However, as a detailed computation of $p_{\rm E,det}$ has

not been done, we use the approximation $p_{\mathrm{E,det}} = p_{\mathrm{QC,det}}$ for this paper and leave a more robust computation for future work.

According to Ref. [147], to incorporate selection effects we replace $R_{\mathrm{E}}$ with $\alpha_{\mathrm{E}} R_{\mathrm{E}}$ and $R_{\mathrm{QC}}$ with $\alpha_{\mathrm{QC}} R_{\mathrm{QC}}$. We need to also replace $Z_{\mathrm{E}}$ with $Z_{\mathrm{E}}/\alpha_{\mathrm{E}}$ and $Z_{\mathrm{QC}}$ with $Z_{\mathrm{QC}}/\alpha_{\mathrm{QC}}$. This amounts to replacing $\exp(R_{\mathrm{E}} + R_{\mathrm{QC}})$ with $\exp(\alpha_{\mathrm{E}} R_{\mathrm{E}} + \alpha_{\mathrm{QC}} R_{\mathrm{QC}})$ in Eqs. (2.7)–(2.10). Thus our posterior over the rates including selection effects is

$$\begin{aligned} &p(\{g_i\}, R_{\mathrm{E}}, R_{\mathrm{QC}}, |\{d_i\}, N) \\ &\propto \left[\prod_{\{i|g_i=1\}}^{N_{\mathrm{E}}} R_{\mathrm{E}} Z_{\mathrm{E}}(d_i)\right]\left[\prod_{\{i|g_i=0\}}^{N_{\mathrm{QC}}} R_{\mathrm{QC}} Z_{\mathrm{QC}}(d_i)\right] \\ &\quad \times e^{-(\alpha_{\mathrm{E}} R_{\mathrm{E}} + \alpha_{\mathrm{QC}} R_{\mathrm{QC}})} p(R_{\mathrm{E}}, R_{\mathrm{QC}}). \end{aligned} \tag{2.16}$$

This can then be propagated into Eqs. (2.10) and (2.11).

### C. Dingo

We now summarize the main features of the machine-learning code Dingo [155–157]. In the following paragraphs, we give a summary of the method used to generate the posteriors of GWs in this paper, in particular, its use of normalizing flows [158,159] and importance sampling [118,160].

In many practical applications, obtaining $p(\boldsymbol{\vartheta}|d)$ in Eq. (2.1) is analytically impossible. But one can use techniques such as nested sampling [161] or Markov chain Monte-Carlo (MCMC) [162] to sample from $p(\boldsymbol{\vartheta}|d)$. The LVK Collaboration has developed tools such as `LALInference` [163] and Bilby [164–166] for this task. However, these methods must evaluate the likelihood $\mathcal{O}(10^{7-8})$ times per event. Thus, for time-domain waveform models produced by solving ordinary differential equations, parameter estimation can be expensive. For example, SEOBNRv4EHM takes $\mathcal{O}(100\text{–}700\ \mathrm{ms})$ per likelihood evaluation, meaning inference can take $\mathcal{O}(\mathrm{week})$ per event even parallelizing over 320 cores [24]. It is then very computationally expensive to analyze the catalog of GW events with such a waveform model.

We can instead use likelihood-free approaches to amortize the inference [156,167,168]. Here we use Dingo [156], which has been shown to achieve results with the same accuracy as standard samplers [118]. We pay the upfront cost of training a neural network for $\mathcal{O}(\mathrm{week})$, but then we can do inference on any events within the trained priors in $\mathcal{O}(\mathrm{hour})$.

Dingo learns a mapping $f_{d,S_n}: u \to \boldsymbol{\vartheta}$ from a simple-base distribution $p(u) = \mathcal{N}(0,1)^D$ to the complex target GW posterior $p(\boldsymbol{\vartheta}|d)$ (it is implied this is also conditioned on $\mathcal{H}_a$). This mapping is learned through a series of composable functions parametrized by neural networks (a normalizing flow). For each data sample $d$, the forward model is given by

$$\begin{aligned} q(\boldsymbol{\vartheta}|d, S_n) &= [f_{d,S_n}]_* \mathcal{N}(0,1)^D \\ &= \mathcal{N}(0,1)^D (f^{-1}_{d,S_n}(\boldsymbol{\vartheta}))\left|\frac{\partial f^{-1}_{d,S_n}}{\partial \boldsymbol{\vartheta}}\right|, \end{aligned} \tag{2.17}$$

where $D$ is the number of GW parameters and $(\cdot)_*$ denotes the push-forward operator. The $d$ and $S_n$ on the subscript of $f_{d,S_n}$ indicate that the mapping uses $d$ and $S_n$ as context to the neural network. The Jacobian in the last term of Eq. (2.17) is a normalization factor to account for the fact that in general $f_{d,S_n}$ is not a volume preserving operation [159].

Dingo is unique from other flow approaches, as the inference is aided by conditioning the networks on the arrival times of GWs in the interferometers. We train two separate networks: one to learn the distribution $q(t_i|d)$ and one to learn the distribution $q(\boldsymbol{\vartheta}|d, S_n, \hat{t}_i)$. Here, $t_i$ are the arrival times of the GW in each detector and can be computed from $\boldsymbol{\vartheta}$. Then $\widehat{t_i}$ are "blurred" versions of the arrival times. That is, $p(\widehat{t_i}|t_i) = \mathrm{Unif}(t_i - 1\ \mathrm{ms}, t_i + 1\ \mathrm{ms})$. The process is to start with an initial guess for $t_i \sim q(t_i|d)$, then, using $t_i$, sample $\widehat{t_i} \sim p(\widehat{t_i}|t_i)$ and get an initial guess for $\boldsymbol{\vartheta} \sim q(\boldsymbol{\vartheta}|d, S_n, \widehat{t_i})$. After obtaining initial guesses, we can Gibbs sample [169] the distributions $p(\widehat{t_i}|t_i)$ and $q(\boldsymbol{\vartheta}|d, S_n, \widehat{t_i})$ to obtain $q(\boldsymbol{\vartheta}, \widehat{t_i}|d, S_n)$. Finally, we can drop $\widehat{t_i}$ from $q(\boldsymbol{\vartheta}, \widehat{t_i}|d, S_n, )$ to obtain $q(\boldsymbol{\vartheta}, |d, S_n)$. The advantage in this process is that the network learning $q(\boldsymbol{\vartheta}|d, S_n, \widehat{t_i})$ never sees a GW with the merger greater than 1 ms away from the start of the data segment. To summarize, by conditioning on the blurred arrival times, we standardize the data, allowing for smoother training.

Dingo also uses an embedding network to compress the high dimensional Fourier domain strain data into a feature vector of length 128 for each detector. This embedding network is trained as part of the mapping $f_{d,S_n}$.

After performing inference with the network, we need to have a guarantee that the distribution $q(\boldsymbol{\vartheta}|d, S_n)$ produced by Dingo, is a good approximation to the true posterior distribution, $p(\boldsymbol{\vartheta}|d, S_n)$. To achieve this, we can importance sample the generated proposal distribution to obtain samples from the true distribution [160]. Explicitly, we first sample $\boldsymbol{\vartheta}_i \sim q(\boldsymbol{\vartheta}|d, S_n)$ and then weight each sample according to

$$w(\boldsymbol{\vartheta}_i) \propto \frac{p(d|\boldsymbol{\vartheta}_i, S_n) p(\boldsymbol{\vartheta}_i)}{q(\boldsymbol{\vartheta}|d, S_n)}. \tag{2.18}$$

Here, we only need to evaluate the likelihood for as many points as there are in the proposal posterior, which is orders of magnitude lower than a nested sampling or MCMC run. Since we only need to compute the likelihood during importance sampling, this can be parallelized across an arbitrary number of cores. In addition, since Dingo is trained on a forward Kullback-Leibler (KL) divergence objective, it tends to cover regions of high density. This is preferred in

scientific domains, as we want to ensure a conservative as possible estimate before importance sampling.

The *effective sample size*, $n_{\rm eff}$, can be computed from the importance weights using

$$n_{\rm eff} = \frac{(\sum_i w_i)^2}{\sum_i w_i^2}. \tag{2.19}$$

This represents the number of samples drawn from the true posterior distribution $p(\boldsymbol{\vartheta}|d)$ [160]. Thus, any test statistic computed with the weighted samples is equivalent to using $n_{\rm eff}$ samples from the true posterior. The importance weights can also be used to compute the evidence, $p(d)$; see Eqs. (2)–(8) in Ref. [118]. When reporting results with importance sampling, we label the result Dingo-IS.

Finally, in this paper we often compute the Jensen-Shannon divergence (JSD) between posterior distributions as a comparison statistic. For example, this is used to compare Dingo-IS with pBilby. The JSD is defined as a symmetrized version of the KL divergence that is between 0 and 1 bits. It is defined as a divergence between two distributions $p(\boldsymbol{\vartheta})$ and $q(\boldsymbol{\vartheta})$, as follows:

$$D_{\rm JS} = \frac{D_{\rm KL}(p|q) + D_{\rm KL}(q|p)}{2}, \tag{2.20}$$

where the KL divergence is

$$D_{\rm KL}(p|q) = \int d\boldsymbol{\vartheta} p(\boldsymbol{\vartheta}) \log_2\left(\frac{p(\boldsymbol{\vartheta})}{q(\boldsymbol{\vartheta})}\right). \tag{2.21}$$

The KL divergence expresses the information loss we would accumulate if using distribution $p$ to approximate a test statistic when $q$ was the true underlying distribution.

## III. ECCENTRIC AND QUASICIRCULAR WAVEFORM MODELS

In this paper, we use mostly multipolar eccentric and quasicircular aligned-spin waveform models, but for some applications also quasicircular spin-precessing models. Several nonspinning and aligned-spin, eccentric inspiral-merger-ringdown models have been proposed in the literature [152,170–178]. During the referee period of this paper, even more more eccentric waveform models were developed [179–186]. Here, we employ the (time-domain) eccentric aligned-spin model SEOBNRv4EHM, developed in Refs. [122,123], the quasicircular aligned-spin model SEOBNRv4HM [120,121], and the quasicircular spin-precessing model SEOBNRv4PHM [121,128–131]. For some studies, we also use the quasicircular spin-precessing numerical relativity (NR) surrogate model NRSur7dq4 [132].

The (EOB) formalism [128,138,187–189] maps the two-body dynamics onto the one of a test body in a deformed Kerr metric, the deformation being the symmetric mass ratio $\nu$. It relies on three key ingredients: (i) a Hamiltonian that describes the conservative dynamics, (ii) a radiation-reaction force, and (iii) the gravitational modes. These three components are built by resumming PN calculations. Furthermore, the EOB approach also provides the full inspiral-merger-ringdown waveforms using physically motivated *Ansätze* for the merger, and results from BH perturbation theory for the ringdown. Finally, EOB waveforms are made highly accurate through calibration to NR simulations [131,190–193], and more recently from the gravitational self-force approach [194].

To fully characterize GWs from eccentric BBHs, one needs to include two additional parameters compared to the quasicircular case. The SEOBNRv4EHM [24,122,123] model adds two new parameters to the quasicircular spin-aligned model, SEOBNRv4HM [120,121]: the initial orbital eccentricity $e$ and relativistic anomaly $\zeta$. The model employs the quasi-Keplerian parametrization to express the relationship between the radial separation $r$ and these parameters [24,122], as follows:

$$r = \frac{p}{1 + e\cos\zeta}, \tag{3.1}$$

where $p$ is the semilatus rectum. In order to integrate the EOB Hamilton equations, one needs to specify initial conditions; see Eqs. (12)–(14) in Ref. [24]. In SEOBNRv4EHM, the eccentricity and relativistic anomaly are part of these initial conditions, and they are specified at an orbit-averaged frequency. We note that one could specify the initial conditions at an instantaneous reference frequency. However, this strongly affects the time to merger and creates a rapidly varying log-likelihood surface, which can cause difficulties for parameter-estimation pipelines, as pointed out in Ref. [24]. In addition, unlike the instantaneous frequency, the orbit-averaged GW frequency is related to twice the orbit-averaged orbital frequency [136] for eccentric orbits. Thus, we can use it to uniquely specify the point along the orbit where we infer the eccentricity and relativistic anomaly. We denote the quasi-Keplerian eccentricity and relativistic anomaly measured at orbit-averaged GW frequency of 10 Hz in the detector frame as $e_{10\ \rm Hz}$ and $\zeta_{10\ \rm Hz}$.

The dynamics of the BBH is used to construct the waveform modes, $h_{\ell m}$. The SEOBNRv4EHM model contains the $(\ell, |m|) = (2,2), (2,1), (3,3), (4,4), (5,5)$ multipoles. The inspiral waveform modes contain 2PN eccentric corrections derived in Ref. [123], and are enhanced during the late inspiral and plunge with nonquasicircular terms that are fitted to quasicircular NR simulations; see Eqs. (7)–(10) in Ref. [122]. Note that in this model, the radiation-reaction force does *not* have eccentric corrections, and the merger-ringdown modes are assumed to be quasicircular [121]. This latter assumption is used by all the current eccentric waveform models, and it is supposed to hold for mild eccentricities [112,195,196].

The waveform modes can be used to construct the gravitational polarizations, as follows:

$$h_+ - ih_\times = \sum_{l=2}^{\infty} \sum_{m=-l}^{m=l} {}_{-2}Y_{lm}(\varphi, \iota) h_{lm}(m_{1,2}, \chi_{1,2}, e, \zeta; t), \tag{3.2}$$

where for aligned spins $(\varphi, \iota)$ are the azimuthal and polar angles to the observer in the source frame. Without loss of generality, $\varphi = \phi_{\rm coal}$ [197].

We remark that the SEOBNRv4EHM model has been tested against (mainly) nonspinning NR simulations up to $e_{20\ \rm Hz} = 0.3$ [136], finding good agreement. Since we are generating waveforms with a starting frequency of 10 Hz, we use Ref. [41] to map the maximum allowed eccentricity to $e_{10\ \rm Hz} \leq 0.5$. Thus, we cannot say anything about the accuracy of the waveform model for events that have eccentricities greater than $e_{10\ \rm Hz} > 0.5$. We stress also that SEOBNRv4EHM does not simultaneously model spin-precession and eccentricity[3] and thus we cannot address the possibility that an event is both eccentric and precessing.

Regarding the quasicircular spin-precessing waveform model SEOBNRv4PHM [121,131], it integrates the time-domain EOB dynamics in a coprecessing frame using the EOB spin-precession equations and a Hamiltonian calibrated to aligned-spin NR simulations. In such a frame, it contains the $(\ell, |m|) = (2,2), (2,1), (3,3), (4,4), (5,5)$ multipoles. Then, the waveform in the coprecessing frame is rotated to the inertial frame [129,130]. In contrast, NRSur7dq4 directly interpolates 1528 precessing NR waveforms with mass ratios $q \geq 1/4$ with $\chi_{1,2} \leq 0.8$ [198]. The model can also be used in the extrapolation region with $q \geq 1/6$ and $\chi_{1,2} \leq 1$. This model is typically used for heavier mass systems in parameter estimation studies, as it is restricted by the length of the training waveforms. This model includes all $\ell \leq 4$ modes.

Before we end the section, we briefly comment on the eccentricity parameter. Since eccentricity is not uniquely defined in GR, there are multiple ways to parametrize the orbit [199]. Waveform models may use orbital parameters, compact object trajectories, energy and angular momentum, or other parametrizations to define eccentricity [122,123,152,178,200–210].

It is, however, possible to use a definition of eccentricity that can be extracted from the waveform. This was proposed in Refs. [135,136] (see also Ref. [211]), where this new eccentricity is denoted $e_{\rm gw}$. This $e_{\rm gw}$ is extracted by interpolating the instantaneous GW frequency of the (2, 2) mode, $\omega_{22}$, along the pericenter and apocenter points. This is calculated as

$$e_{\rm gw} = \cos(\psi/3) - \sqrt{3}\sin(\psi/3), \tag{3.3}$$

with

$$\psi = \arctan\left(\frac{1 - e_{\omega_{22}}^2}{2e_{\omega_{22}}}\right), \tag{3.4}$$

and

$$e_{\omega_{22}} = \frac{\omega_{22,p}^{1/2} - \omega_{22,a}^{1/2}}{\omega_{22,p}^{1/2} + \omega_{22,a}^{1/2}}, \tag{3.5}$$

where $\omega_{22,p}$ and $\omega_{22,a}$ are the GW frequency of the 22 mode at periastron and apocenter.

We can similarly interpolate the GW mean anomaly

$$l_{\rm gw} = 2\pi \frac{t - t_i^p}{t_{i+1}^p - t_i^p}. \tag{3.6}$$

Here, $t$ is the time at which we are measuring the mean anomaly and $t_i^p$ is the time of the $i$th periastron passage measured using the (2, 2) mode frequency.

We compute $e_{\rm gw}$ using parallelized version of the `gw_eccentricity` package [24,135].[4] We choose to infer the eccentricity at a dimensionless frequency of $M_{\rm det} f_{\rm ref}$, where $M_{\rm det}$ is the detector frame total mass of the system and $f_{\rm ref} = 10$ Hz. The reason to multiply by the total mass is because we do not want our reported eccentricity to depend on the redshift of the source. When reporting the GW eccentricity at 10 Hz, we denote this as $e_{\rm gw,10\ Hz}$.

## IV. ZERO-NOISE SYNTHETIC-DATA AND REAL EVENTS

### A. Trained networks and priors

We train 25 Dingo networks on 80 GB NVIDIA-A100 GPUs each for 11 days. We train 11 networks for the eccentric aligned-spin case, 11 networks for quasicircular aligned-spin case and four networks for the quasicircular precessing-spin case. The number of networks corresponds to the fact that one has to train a separate network for each observing run (noise curve), detector configuration, waveform model, choice of gravitational modes, mass prior, and distance prior. The mass and distance prior range is optional, but we find that training two separate networks for the regimes $d_{\rm L} < 3$ Gpc and $d_{\rm L} < 6$ Gpc leads to increased sample efficiency. Similarly, if we train a network with a smaller mass prior, we achieve higher sample efficiency in the prior. But we also want to analyze heavy BBHs, so we train a separate network increasing the upper bound of the mass prior. Since there are some GW events that only occur in one detector in the third-observing run, we also train networks for LIGO-Hanford and LIGO-Livingston only. This is also useful for doing single-detector analyses of events

[3]This is also true of other inspiral-merger-ringdown waveform models in the literature, with the exception of Ref. [133].

[4]We use the "Amplitude" method in `gw_eccentricity` and set `num_orbits_to_exclude_before_merger = 1`.

with glitches. We train the networks in the range $(f_{\min}, f_{\max}) = (20\ \text{Hz}, 1024\ \text{Hz})$. To condition the data, we use a Tukey window with a 0.4 second roll-off. We train the networks using an 8-sec data stream, which implies a $\Delta f = 0.125$. We whiten the signals by sampling over 4152 Welch PSDs estimated from 128 seconds of data obtained from the GW Open Science Center using the `DCS-CALIB_STRAIN_CLEAN_C01` channel. The networks were trained assuming Gaussian detector noise. The networks and their settings have been made publicly available on Zenodo at Ref. [212].

While we trained a large number of networks, it is important to realize that the inference is amortized. This means the computational speedup compared to traditional samplers will scale as the number of events increases. For example, in O1, where we analyzed only one GW event, there is no speedup compared to a traditional sampler. However, in O3, where we analyzed 51 events, the speedup is on the order of 6 months. Another subtle point is that in GW science, we rarely perform parameter estimation for each event once. We may want to change the prior, $f_{\min}$, $f_{\max}$ or in the case of a traditional sampler boost the sampler settings. We also may want to study maximum likelihood injections for consistency. For example, in this study, we obtained more than 300 posteriors across different waveform models before generating the final catalog of 57 events. Thus, while we trained a large number of networks, the speedup is still significant and scales well with a large number of GW events.

We now discuss the subset of events we do not analyze. We do not analyze events with a chirp mass below $15M_{\odot}$. This includes neutron-star events (although this is being addressed in an upcoming work [213]). This is because low-mass systems have rapid Fourier-domain oscillations at low frequencies. As a consequence, if we want to represent the data, we need to use a much larger embedding network, which leads to significant computational cost. As a low chirp mass corresponds to a longer signal, this constraint implies we do not analyze events longer than 8 seconds.

We also do not report on events for which we were unable to obtain 5,000 effective samples. Note that we have purposely set this to a very high threshold in order to be indistinguishable from other samplers like pBilby, and have a smooth posterior. We see that reducing this threshold leads to spikes in the posterior density, which can lead to JSDs with pBilby larger than 0.002 bits (the expected stochastic deviation from identical nested sampling runs [165]).

We set an isotropic in component spin prior with $|\chi_{1,2}| < 0.9$. We also set a uniform prior in $\zeta_{10\ \text{Hz}} \in [0, 2\pi]$, a uniform prior in $e_{10\ \text{Hz}} \in [0, 0.5]$ and a uniform in component mass prior on the mass ratio $q \in [0.125, 1]$. The upper bound in the $e_{10\ \text{Hz}}$ is set by the restriction of the waveform model (see Sec. III). Other than this, the priors are the same as in Ref. [118].

We use a uniform prior on eccentricity as opposed to a log-uniform prior informed by astrophysics. We instead incorporate the astrophysics information by folding it into our computation of the prior odds (see Eq. (2.4)) or $p_{\text{ecc}}$ [see Eq. (2.11)]. Having a uniform prior is also useful because if we perform a population study in the future, we can importance sample to a multitude of different priors [13]. In contrast, if we use a light-tailed log-uniform prior, we could not easily convert to a different prior. This is because there would be many high-weight points at high eccentricities leading to low sample efficiency. A separate reason to adopt a uniform prior instead of an astrophysical log-uniform one is so that we do not have to decide where to place the lower bound of a log-uniform prior. Changing this lower bound can strongly affect Bayes factors, as it gives high weight to low eccentricities in the evidence integral.

However ultimately, a feature of a good Bayesian analysis is using multiple reasonable priors. For completeness, we also compute Bayes factors with a log-uniform prior on $e_{10\ \text{Hz}} \in (10^{-4}, 0.5)$ for GW200129, GW190701 and GW200208_22. We display the results in Table I and Fig. 2. We note that because these events are likelihood dominated, there is very little shift in the posterior, but the Bayes factors for eccentricity do decrease.

When performing the analysis with the quasicircular spin-precessing SEOBNRv4PHM and NRSur7dq4 models, we utilize the same priors as in the previous paragraph except for the dimensionless spin magnitudes. As stated above, for the eccentric model, we restrict the dimensionless spin magnitudes to $|\chi_{1,2}| < 0.9$. However, in the case of GW200129 with NRSur7dq4, there is support for $a_{1,2} > 0.9$. Thus we perform the spin-precessing analysis with and without the spin-prior restriction and take the higher evidence. This is to avoid artificially lowering the evidence for precession [214]. For the spin angles, we use the same priors as in Ref. [118].

### B. Zero-noise synthetic injection

To validate the use of Dingo with eccentric waveform models, we first perform two synthetic signal (injections) in zero-noise using two independent samplers, pBilby and Dingo. Due to the expensive nature of doing SEOBNRv4EHM runs with pBilby, we use only the $(\ell, |m|) = (2, 2)$ modes in the injection and recovery.

We need to make some modifications to allow Dingo to work with zero noise. Dingo is trained on Gaussian detector noise. Thus we cannot simply inject a zero-noise signal into the data, as it will be flagged as out of distribution, and give a low effective sample size. Instead, we first run Dingo on 100 Gaussian noise realizations while fixing the injected parameters. We then pool the results. The idea is that when we average the Dingo posterior over infinite noise realizations, this should be close (though generally broader) than the true zero-noise posterior.

However, with this method we no longer have an estimate for the probability density of each sample, as there is no guarantee the set of pooled samples are drawn from a normalized distribution. Thus, we train an unconditional density estimator on the set of pooled samples in order to

TABLE I. Bayes factors of the three GW events with $\log_{10}\mathcal{B}_{\mathrm{EAS/QCAS}} > 1$. The first column indicates which glitch mitigation algorithm is used (see text). The second column indicates whether the prior on $e_{10\ \mathrm{Hz}}$ is is uniform between [0.0, 0.5] or log-uniform between $[10^{-4}, 0.5]$. The third column indicates the Bayes factors between the eccentric aligned-spin $(\ell, m) = (2, 2)$ mode only model (SEOBNRv4E) and quasicircular aligned-spin $(\ell, m) = (2, 2)$ mode only model (SEOBNRv4E). The fourth through sixth columns indicate the Bayes factors between the eccentric aligned-spin model (SEOBNRv4EHM) against the quasicircular aligned-spin (SEOBNRv4HM) or quasicircular precessing-spin (SEOBNRv4PHM or NRSur7dq4) models. The last two columns indicate the mean and 90% highest density interval of the SEOBNRv4EHM posterior for $e_{10\ \mathrm{Hz}}$ and $e_{\mathrm{gw},10\ \mathrm{Hz}}$, respectively. The errors in each $\log_{10}$ Bayes factor are less than 0.04. For entries with dots, we do not compute Bayes factors due to a lack of networks that cover the appropriate prior.

| Glitch subtraction | $e$ prior | SEOBNRv4 $\log_{10}\mathcal{B}$ | SEOBNRv4HM $\log_{10}\mathcal{B}$ | SEOBNRv4PHM $\log_{10}\mathcal{B}$ | NRSur7dq4 $\log_{10}\mathcal{B}$ | $e_{10\ \mathrm{Hz}}$ | $e_{\mathrm{gw},10\ \mathrm{Hz}}$ |
|---|---|---|---|---|---|---|---|
| | | | GW200129 | | | | |
| `gwsubtract` | Uniform | 4.57 | 4.75 | 4.92 | 4.0 | $0.34^{+0.11}_{-0.06}$ | $0.27^{+0.10}_{-0.12}$ |
| `BayesWave A` | Uniform | 1.7 | 1.84 | 2.20 | 1.53 | $0.24^{+0.10}_{-0.10}$ | $0.17^{+0.14}_{-0.13}$ |
| `BayesWave B` | Uniform | 2.92 | 3.08 | 3.43 | 2.35 | $0.28^{+0.09}_{-0.11}$ | $0.22^{+0.12}_{-0.13}$ |
| `BayesWave C` | Uniform | 2.85 | 2.93 | 2.63 | 1.43 | $0.27^{+0.09}_{-0.10}$ | $0.22^{+0.13}_{-0.14}$ |
| `gwsubtract` | Log-uniform | 4.02 | 3.98 | 3.99 | 3.23 | $0.33^{+0.07}_{-0.11}$ | $0.28^{+0.11}_{-0.12}$ |
| `BayesWave A` | Log-uniform | 1.79 | 1.26 | 1.61 | 0.94 | $0.22^{+0.13}_{-0.15}$ | $0.17^{+0.14}_{-0.13}$ |
| `BayesWave B` | Log-uniform | 2.28 | 2.43 | 2.78 | 1.70 | $0.27^{+0.09}_{-0.11}$ | $0.22^{+0.13}_{-0.12}$ |
| `BayesWave C` | Log-uniform | 2.22 | 2.27 | 1.97 | 0.76 | $0.26^{+0.10}_{-0.11}$ | $0.22^{+0.13}_{-0.13}$ |
| | | | GW190701 | | | | |
| `BayesWave` | Uniform | 2.72 | 3.0 | 2.61 | ⋯ | $0.46^{+0.04}_{-0.04}$ | $0.54^{+0.30}_{-0.12}$ |
| `BayesWave` | Log-uniform | 1.86 | 2.11 | 1.71 | ⋯ | $0.45^{+0.05}_{-0.04}$ | $0.53^{+0.31}_{-0.11}$ |
| | | | GW200208_22 | | | | |
| Unmitigated strain | Uniform | 1.25 | 1.77 | 1.23 | ⋯ | $0.4^{+0.08}_{-0.15}$ | $0.39^{+0.23}_{-0.23}$ |
| Unmitigated strain | Log-uniform | 0.54 | 1.05 | 0.48 | ⋯ | $0.35^{+0.15}_{-0.33}$ | $0.37^{+0.19}_{-0.20}$ |

recover the density of $q_{\mathrm{ZN}}(\boldsymbol{\vartheta}|h(f))$. We use $1 \times 10^6$ pooled samples as a training dataset for the unconditional density estimator.

Now that we have the density of each sample, we importance sample the set of pooled samples, but using a zero-noise likelihood, $p_{\mathrm{ZN}}(h|\boldsymbol{\vartheta})$, when computing the importance weights. Thus, we have an exact reconstruction of the zero-noise posterior distribution.

We present the analysis of two injections in Fig. 1 (note the result which should be used for comparison is the orange curve labeled Dingo-IS). The injection parameters are $\chi_{\mathrm{eff}} = -0.23$, $\mathcal{M}_{\mathrm{det}} = 28M_\odot$, $q = 1/3$ and $e = 0.1$ or $e = 0.2$. The JSD between the one-dimensional marginals of pBilby and Dingo-IS are all less than 0.002 bits (the expected stochastic variation from GW sampling algorithms [165]). We note that while Dingo and pBilby have a disagreement, after importance sampling this disagreement disappears. We can also see that the proposal density generated by Dingo is broader than the true posterior, a desirable property for importance sampling. These two facts give us confidence that Dingo-IS and pBilby have comparable results. We comment that for both samplers, there is some bias in the recovered chirp mass and eccentricity, which is reminiscent of the behavior in Ref. [98].

In order to further verify the accuracy of Dingo-IS with eccentric signals, we also perform a injection with simulated Gaussian noise and compare to pBilby. This test is shown in Appendix D.

### C. GW200129

There has been considerable interest around GW200129 due to the fact that it has shown signs of orbital precession [214], evidence for a measurable kick velocity [215], false violations of GR due to waveform systematics [25], and a glitch [216,217]. Therefore, to analyze this event, we follow the treatment of Refs. [214,216,217]. Namely, we incorporate multiple glitch variations and analyze this event also for precession using both SEOBNRv4PHM and NRSur7dq4.

When analyzed with SEOBNRv4EHM, GW200129 is an intermediate-mass BBH consistent with zero effective spin. In particular, we find $M_{\mathrm{det}} = 78.3^{+4.2}_{-3.1}$, $M_{\mathrm{src}} = 69.4^{+4.2}_{-3.1}$, and $\chi_{\mathrm{eff}} = 0.02^{+0.12}_{-0.11}$. We infer $e_{\mathrm{gw},10\ \mathrm{Hz}} = 0.27^{+0.10}_{-0.12}$, $e_{\mathrm{gw},20\ \mathrm{Hz}} = 0.16^{+0.04}_{-0.05}$, and $\log_{10}\mathcal{B}_{\mathrm{EAS/QCAS}}$ in the range 1.84–4.75.

There is a striking variation in the Bayes factors when using different glitch mitigation techniques. In particular, `gwsubtract` [216,218] favors eccentricity over `BayesWave` [219,220] by 2+ orders of magnitude (see Table I and Figs. 2, 3, and 6). This makes interpreting the analysis challenging, as one has to decide which glitch mitigation technique to trust.

The `gwsubtract` mitigation technique uses a witness time series from an auxiliary channel in the interferometers to linearly subtract the noise. In particular, one uses the witness time series and the strain data to compute a transfer function between the auxiliary channel and true strain

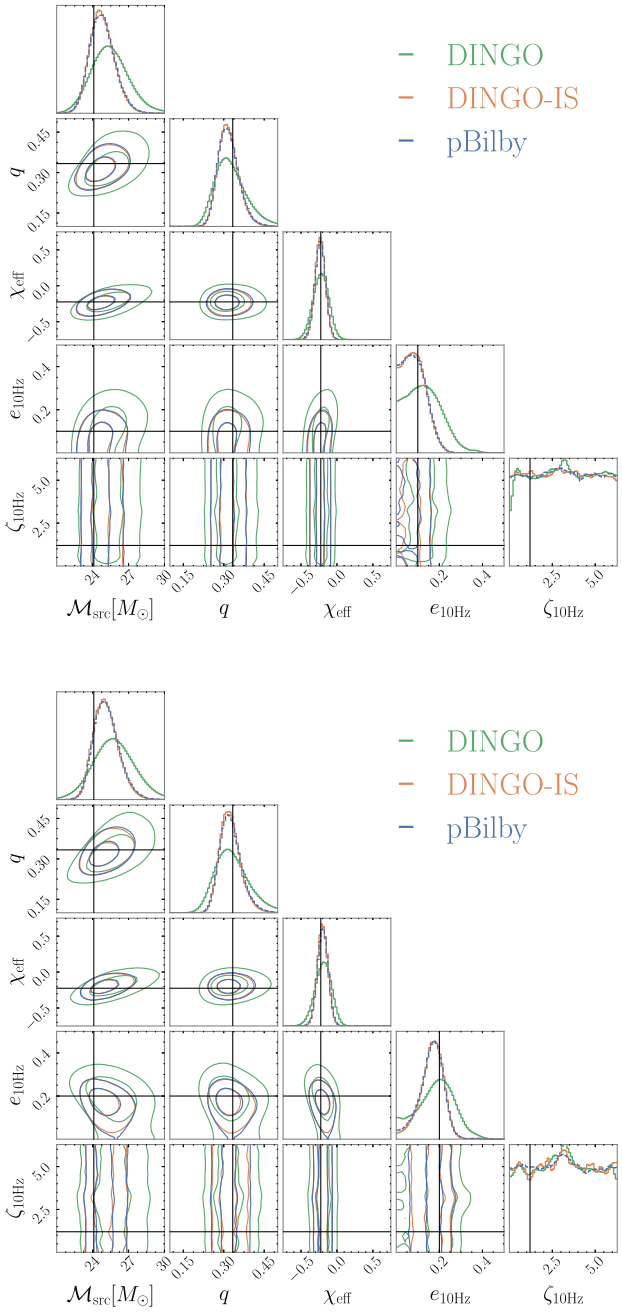


FIG. 1. Zero-noise injections of SEOBNRv4EHM with parameters $\chi_{\rm eff} = -0.23$, $\mathcal{M}_{\rm det} = 28M_\odot$, $q = 1/3$ and initial eccentricities $e_{10\,\rm Hz} = 0.1$ and $e_{10\,\rm Hz} = 0.2$ for the top and bottom figures, respectively. The injections are recovered with both Dingo, Dingo-IS (Dingo with importance sampling) and pBilby.

[218]. This transfer function is then used to estimate the deglitched strain data. This method was used by the LVK Collaboration to mitigate the glitch in LIGO-Livingston during the official analysis. This is because the witness function was well estimated by the modulation control system at the time of the detection (see Sec. 3 in Ref. [216]). We also note that there have recently been additional studies of the impact of glitch mitigation on GW200129 in Refs. [222,223], indicating that `gwsubtract` may undersubtract the glitch.

`BayesWave`, on the other hand, takes a data-driven approach. It models the astrophysical signal with a GW model[5] and incoherent non-Gaussian noise with sine-Gaussian wavelets. It also models the PSD with a combination of cubic splines and Lorentzians. It then runs a transdimensional reversible-jump MCMC to infer a posterior distribution over the signal, glitch, and PSD. Finally, one takes a fair draw from the inferred glitch distribution and subtracts it from the detector strain. We can then run inference on the glitch subtracted strain data. Often in LVK analyses, only one glitch draw from the posterior is used (and we indeed follow this standard for most events analyzed). However, it is more accurate to draw several glitches from the glitch posterior and marginalize over them. This is in effect what is done in Ref. [217] where they take three glitch draws, labeled "A," "B," and "C," and run inference on each mitigated frame. For this paper, we utilize the same glitch draws as Ref. [217].

We run the analysis on both mitigation techniques for completeness.[6] We also run the analysis using only LIGO-Hanford or only LIGO-Livingston. While there is a positive Bayes factor for eccentricity regardless of which detector combination is used, the evidence for eccentricity is dominated by LIGO-Livingston (see Appendix A). We default to reporting results of GW200129 using `gwsubtract` glitch subtracted data, as this is what is used by official LVK analyses of this event. However, we explicitly indicate in the captions which glitch mitigation is being applied. There is very strong evidence for eccentricity in the `gwsubtract` case ($\log_{10}\mathcal{B}_{\rm EAS/QCAS} > 3.5$), but we cannot rule out the possibility that `gwsubtract` undersubtracts the glitch or `BayesWave` over-subtracts the glitch. Since the conclusive evidence of eccentricity is contingent on the systematic uncertainty of glitch mitigation, we do not claim this event to be a bona fide eccentric event. However, we note that greater than zero evidence for eccentricity is present irrespective of the glitch mitigation (see Figs. 3 and 2 and Table I).

For visualization, we display the 90% highest density interval of the projected waveforms of GW200129 in LIGO-Hanford and LIGO-Livingston in Fig. 4. We use the posterior obtained with the `BayesWave C` glitch mitigation. We also show the location of the `BayesWave C` glitch. To generate this figure, we draw samples from the 90% highest density

[5]Notably, the quasicircular aligned-spin `IMRPhenomD` [224,225] is used, but more generally one should use an eccentric waveform model. However, this is computationally expensive (see Ref. [220]).

[6]We also experimented with truncating the glitch by setting the $f_{\rm min} = 50$ Hz. However, we note that the majority of waveform difference from eccentricity with GW200129-like parameters is contained in the 20–50 Hz regime so this type of test is inconclusive.

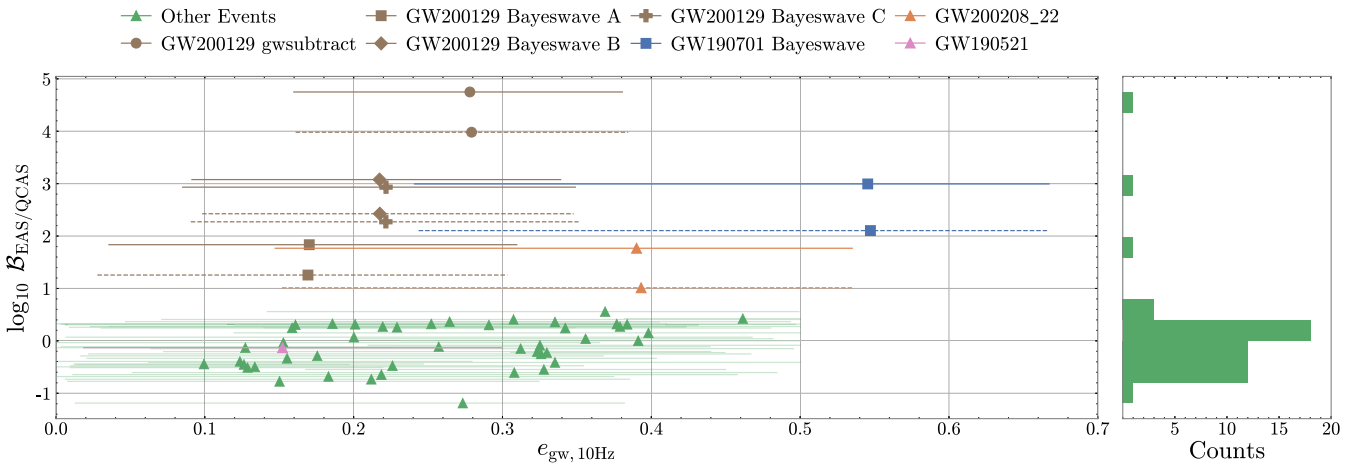


FIG. 2. Left: $\log_{10} \mathcal{B}_{\mathrm{EAS/QCAS}}$ and 90% highest-density intervals on $e_{\mathrm{gw,10\ Hz}}$ for the 57 events analyzed. Many events have $\log_{10} \mathcal{B}_{\mathrm{EAS/QCAS}} < 1$, and we color these green and reduce their opacity. However, there are three events (GW200129, GW190701, and GW200208_22) which have $\log_{10} \mathcal{B}_{\mathrm{EAS/QCAS}} > 1$ and are labeled in the legend. We compute $e_{\mathrm{gw,10\ Hz}}$ only for these three events, since for events with low support for eccentricity, $e_{\mathrm{gw,10\ Hz}} \approx e_{\mathrm{10\ Hz}}$ [135]. We also color in pink GW190521, which has shown signs of eccentricity in previous papers, but not in our analysis and the one in Ref. [24]. For GW190521, we report the eccentricity at 5.5 Hz. The different symbol shapes indicate variations on the glitch mitigation algorithm employed in the analysis (see text). The solid lines indicate a uniform prior on $e_{\mathrm{10\ Hz}}$ from [0, 0.5] while the dashed lines indicate a log uniform prior on $e_{\mathrm{10\ Hz}}$ from $[10^{-4}, 0.5]$. Right: histogram of $\log_{10}$ Bayes factors.

interval of the SEOBNRv4EHM and SEOBNRv4HM posteriors, and project them onto the detector. We then whiten the waveform, glitch, and strain. By whitening, we mean that we set the noise variance in each frequency bin to one using the PSD (see Ref. [226] for further details). We plot the strain data with a rolling window average with a window size of 1 ms for visualization purposes. In Fig. 5, we show the radial separation as a function of the coordinate angle of a binary with parameters corresponding to the maximum likelihood of the SEOBNRv4EHM analysis of GW200129 with `BayesWave C` glitch mitigation.

Due to the possibility that GW200129 is precessing, we additionally compute the Bayes factor against the quasicircular precessing-spin case. This test is also important as for short signals, it is possible that spin-precession can mask the effect of eccentricity [126,127]. We first compute the Bayes factors against SEOBNRv4PHM and find that the $\log_{10} \mathcal{B}_{\mathrm{EAS/QCP}}$ lies in the range 2.20–4.92. We also compute the Bayes factor against NRSur7dq4 and find $\log_{10} \mathcal{B}_{\mathrm{EAS/QCNRP}}$ in the range 1.43–4.0. When using the `gwsubtract` glitch mitigation, we find the difference between the maximum $\log_{10}$ likelihoods of SEOBNRv4EHM and NRSur7dq4 is 5.7.

The range of Bayes factors is again due to using different glitch mitigation algorithms. One needs to interpret the $\log_{10} \mathcal{B}_{\mathrm{EAS/QCNRP}}$ with caution since eccentricity and precession are not the only differences between `SEOBRv4EHM` and NRSur7dq4. In particular, the underlying quasicircular model of SEOBNRv4EHM is different from NRSur7dq4. Nonetheless, there is evidence of eccentricity irrespective

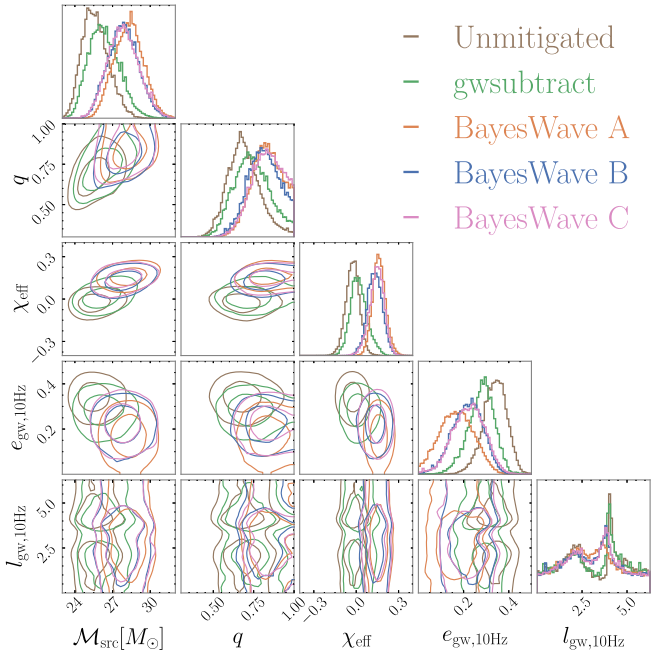


FIG. 3. Posteriors of GW200129 using different glitch mitigation techniques. In green is the analysis with `gwsubtract`, which uses auxiliary detector channels and transfer functions to subtract glitches. Shown in orange, blue, and pink is the analysis carried out using `BayesWave` deglitching. This method involves generating a posterior of glitches using and then drawing individual glitches from this "glitch posterior." A, B, and C indicate different fair draws from the glitch distribution and are publicly available at Ref. [221].

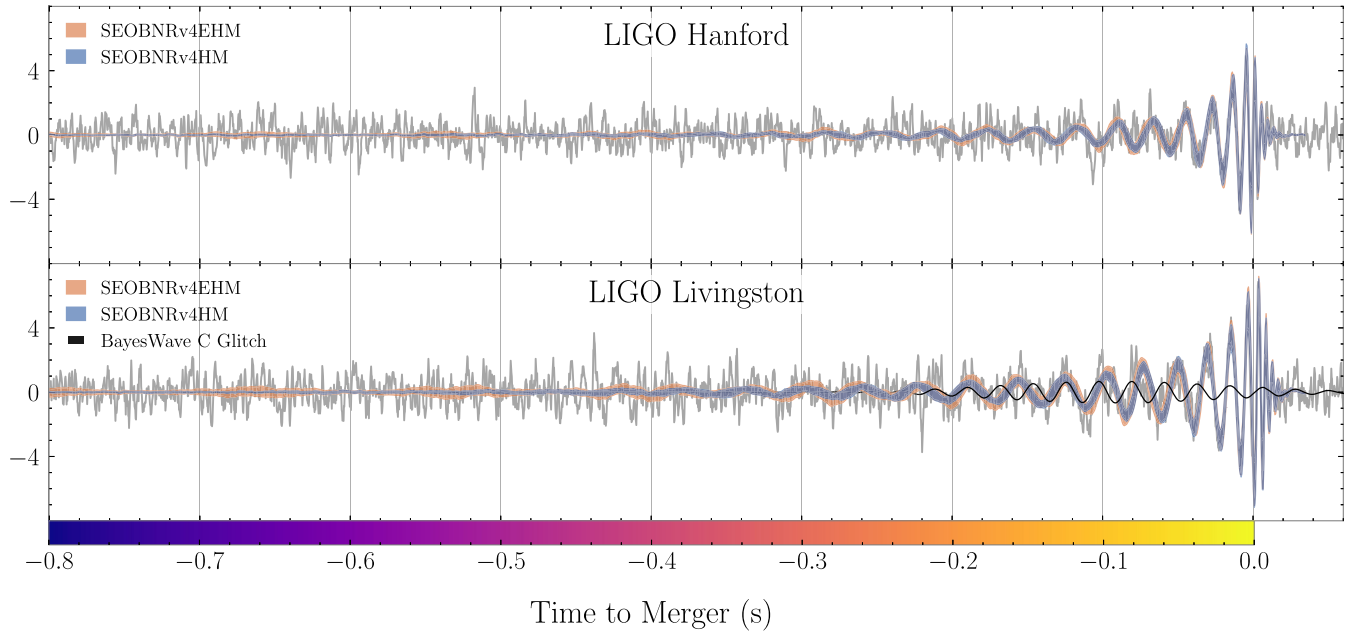


FIG. 4. 90% credible interval of the projected waveforms of GW200129 analyzed with SEOBNRv4EHM (orange) and SEOBNRv4HM (blue) in LIGO-Hanford (top) and LIGO-Livingston (bottom). The posterior was obtained using `BayesWave C` mitigated data. Shown in light gray is the whitened strain data without any glitch mitigation. We also overplot the location of the `BayesWave C` glitch in the Livingston detector in black. On the bottom of the plot, we show a color bar that corresponds to the trajectory represented in Fig. 5. The regions in the inspiral where the SEOBNRv4EHM waveform deviates from SEOBNRv4HM waveform are due to periastron passages of the BBH.

of the spin-precessing waveform model used. Despite the eccentric aligned-spin hypothesis being preferred over the quasicircular spin-precessing hypothesis, we do not exclude the possibility that GW200129 is spin-precessing (it could be both eccentric and spin-precessing).

As another check if spin-precession can mimic the eccentricity in this event, we also perform injections of the maximum likelihood waveform of NRSur7dq4 and recover with SEOBNRv4EHM (and vice versa). We conclude for the maximum likelihood parameters of this event, injected precession cannot mimic the effect of eccentricity. Additionally, injected eccentricity does not mimic the effect of precession. The result of this systematic study can be seen in Fig. 15 in Appendix G.

Since SEOBNRv4EHM is preferred over NRSur7dq4, this has important implications for the kick velocity of this event. In particular, Ref. [215] showed evidence for a measurable kick velocity in GW200129. However, when using an eccentric aligned-spin model, the evidence for a measurable kick velocity substantially decreases (see Appendix E).

### D. GW190701

We also see signs for eccentricity in GW190701. To our knowledge, GW190701 has not shown signs of eccentricity in previous studies. When analyzed with SEOBNRv4EHM,

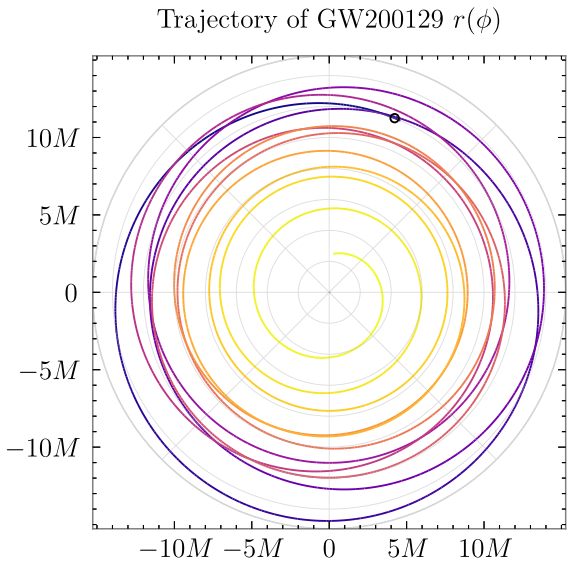


FIG. 5. Radial separation as a function of the coordinate angle of a binary with parameters corresponding to the maximum likelihood of the SEOBNRv4EHM analysis. The color of the orbit corresponds to the time to merger, and can be compared with the color bar in Fig. 4. The separation is reported in units of the total mass of the system $M$. We mark the start of the orbit with a circle, which is chosen to be $t = -0.8$ seconds before merger.

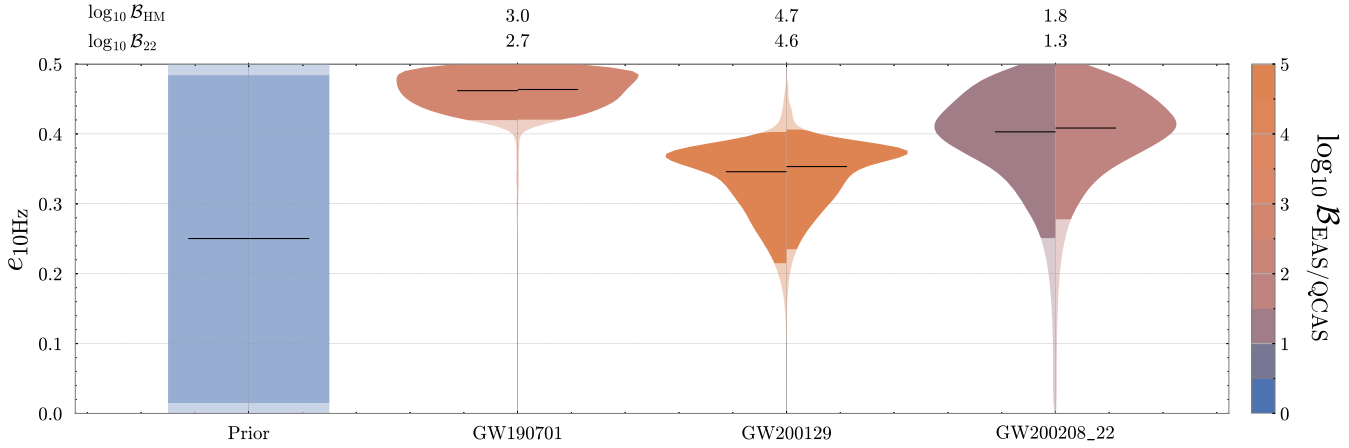


FIG. 6. Eccentric violin plots for all events with $\log_{10}\mathcal{B}_{\mathrm{EAS/QCAS}} > 1$ from the first through third observing runs of the LVK. The posterior distributions are obtained with Dingo and then importance sampled. The eccentricity is measured at 10 Hz in the detector frame using the quasi-Keplerian parametrization [see Eq. (3.1)]. For each event, the left violins are the posterior distributions using only the $(\ell, |m|) = (2, 2)$ mode, and the right violins are the posteriors using higher modes [see Eq. (3.2)]. Each violin is colored according to the $\log_{10}$ Bayes factor between the eccentric aligned-spin and quasicircular aligned-spin hypotheses. Above the plot, we report the $\log_{10}$ Bayes factor when using higher modes ($\log_{10}\mathcal{B}_{\mathrm{HM}}$) and when only using the $(\ell, m) = (2, 2)$ mode ($\log_{10}\mathcal{B}_{22}$). The dark-shaded regions indicate the 90% credible interval of the distribution and the black lines indicate the median value of the eccentricity.

GW190701 is a heavy BBH with $M_{\mathrm{det}} = 183.5^{+40.7}_{-39.1}$, $M_{\mathrm{src}} = 131.9^{+18.0}_{-17.7}$ and $\chi_{\mathrm{eff}} = -0.04^{+0.21}_{-0.26}$. We find that $e_{\mathrm{gw,10\ Hz}} = 0.54^{+0.12}_{-0.30}$, $e_{\mathrm{gw,20\ Hz}} = 0.31^{+-0.12}_{-0.13}$ with Bayes factors of $\log_{10}\mathcal{B}_{\mathrm{EAS/QCAS}} = 3.0$ and $\log_{10}\mathcal{B}_{\mathrm{EAS/QCP}} = 2.61$ (Table I). We find the difference between the maximum $\log_{10}$ likelihoods of SEOBNRv4EHM and SEOBNRv4PHM is 5.2. Critically, the eccentricity rails against the upper bound of the prior (see Fig. 6). Thus, this Bayes factor is a conservative lower bound, since there is likelihood support above $e_{10\ \mathrm{Hz}} > 0.5$. Like GW200129, this event also contains a glitch, which is subtracted using one fair draw of a `BayesWave` glitch model. However, we do not have access to the glitch distribution in this case, so we perform the analysis using only one fair draw of the glitch posterior.

We tried to train a Dingo network in the regime $e_{10\ \mathrm{Hz}} < 0.8$, to investigate the high eccentricity of GW190701. However, the gradients of the network increase dramatically in the first five epochs. This indicates that the additional hyperparameters of the network, such as the learning rate, need to be further modified. Another possibility is that artifacts in the waveform due to high eccentricity and spins [122] affect substantially the learning process. These issues could be potentially addressed in the future with improved waveform models [227] and network architectures [119].

The maximum likelihood of GW190701 only has 3 to 4 inspiral cycles in band. This is primarily due to the high masses. The signal length is further shortened due to the high value of $e_{10\ \mathrm{Hz}}$. This means one needs to interpret conclusions with caution (since the eccentric waveform model used assumes a quasicircular merger ringdown). We note that, independently of the number of cycles, confidently measuring eccentricity in such high mass events would require incorporating eccentric effects in the merger ringdown, which we leave for future work.

Furthermore, we need to back evolve the waveform in order to have enough cycles to compute $e_{\mathrm{gw,10\ Hz}}$. However, this means evolving to values where $e_{10\ \mathrm{Hz}} > 0.5$. Here, the waveform model has not been tested against NR. Thus, one needs to interpret the $e_{\mathrm{gw,10\ Hz}}$ for this event with additional caution. With waveform models which probe and are tested against higher initial eccentricities, this issue can be mitigated [227].

### E. GW200208_22

We also see signs for eccentricity in GW200208_22. The evidence for eccentricity in GW200208_22 has been seen previously in Refs. [20,23]. When analyzed with SEOBNRv4EHM, we observe GW200208_22 is an intermediate-mass BBH with support for positive effective spin ($M_{\mathrm{det}} = 94.7^{+28.9}_{-12.5}$, $M_{\mathrm{src}} = 66.3^{+17.5}_{-12.5}$ and $\chi_{\mathrm{eff}} = 0.12^{+0.30}_{-0.29}$). We find that $e_{\mathrm{gw,10\ Hz}} = 0.39^{+0.23}_{-0.23}$, $e_{\mathrm{gw,20\ Hz}} = 0.21^{+0.08}_{-0.08}$, $\log_{10}\mathcal{B}_{\mathrm{EAS/QCAS}} = 1.77$ and $\log_{10}\mathcal{B}_{\mathrm{EAS/QCP}} = 1.23$. We find the difference between the maximum $\log_{10}$ likelihoods of SEOBNRv4EHM and SEOBNRv4PHM is 3.1.

Importantly, this event has a relatively low value of $p_{\mathrm{astro}}$ of 0.7 and high false alarm rate (FAR) of 4.8 $\mathrm{yr}^{-1}$ (recovered by `pycbc-bbh` [228]). Therefore, it sits just above the detection threshold set by the LVK. We note that these values are obtained using quasicircular templates. (though see Ref. [229], which uses eccentric templates and was released during the referee period of this paper.)

We identify railing of the mass ratio on the lower bound of $q = 0.125$ with SEOBNRv4HM, SEOBNRv4PHM, and SEOBNRv4EHM. However, due to the lower bound

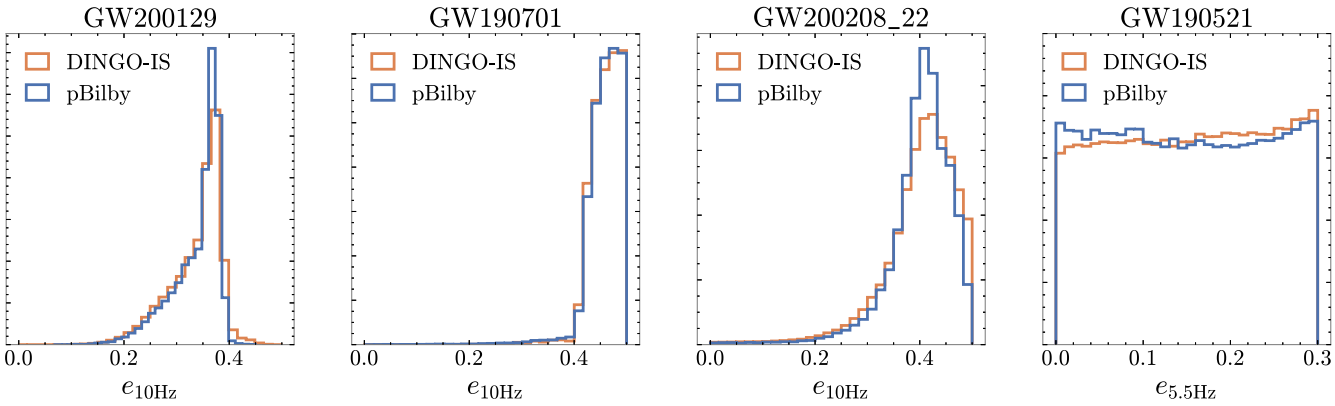


FIG. 7. Dingo-IS versus pBilby marginal eccentricity distributions for four of the events analyzed in the main text. We show that the presence of eccentricity is also found by nested samplers. Note that while there are are slight differences between Dingo-IS and pBilby in the GW200208_22 posterior, this can be attributed to the railing of the eccentricity distribution at 0.5. When extending the prior of the pBilby run, we again find better agreement.

mass restriction set by Dingo, we do not relax this lower bound. Instead, we perform pBilby runs extending the lower bound on $q$ to 0.05 to explore the possibility of a secondary mode at low mass ratios. We do not see evidence for such a mode, and the Bayes factors do not change significantly. We also see railing of eccentricity against the eccentricity upper bound of $e_{10\,\mathrm{Hz}} = 0.5$. But due to the model restriction of SEOBNRv4EHM (i.e., $e < 0.5$), we do not increase this upper bound. Like in the case of GW190701, $\log_{10}\mathcal{B}_{\mathrm{EAS/QCAS}}$ are then only conservative lower bounds of the Bayes factor.

### F. GW190521

We also train specialized SEOBNRv4EHM and SEOBNRv4HM networks to analyze GW190521. This event is interesting as it only has four cycles in the detectors' bandwidth (assuming $f_{\mathrm{min}} = 11$ Hz), and the SNR is dominated by the merger and ringdown. It has been suggested that this event is a head-on collision with exotic compact objects [230], a nonspinning hyperbolic capture [113], a merger within an active galactic nucleus [90,231,232], and eccentric [21,110]. It has also been suggested that this event has an electromagnetic counterpart detected by the Zwicky Transient Facility [231].

In order to analyze GW190521, we train a specialized network with a larger upper bound on the detector frame component masses ($m_{1,2} < 180M_{\odot}$). The network also has a starting frequency of $f_{\mathrm{start}} = 5.5$ Hz. This is to make sure the higher modes, and in particular the (4, 4) mode, are in band at the minimum frequency, which we set to $f_{\mathrm{min}} = 11$ Hz. Thus the eccentricity is sampled at 5.5 Hz ($e_{5.5\,\mathrm{Hz}}$). Accordingly, we adjust the prior in the eccentricity to be uniform between (0, 0.3).

When using SEOBNRv4EHM, we recover $e_{\mathrm{gw},5.5\,\mathrm{Hz}} = 0.12^{+0.12}_{-0.12}$ for GW190521 with a posterior very close to the prior. We find a $\log_{10}\mathcal{B}_{\mathrm{EAS/QCAS}}$ of 0.04. This is likely due to the same reasons described in Ref. [24]. Notably, GW190521 is a merger-ringdown dominated signal, but the eccentric SEOBNRv4EHM waveform is the same as the quasicircular SEOBNRv4HM waveform during the merger ringdown. Thus it is difficult to measure eccentricity in the merger. So while we do not see signs of eccentricity in this analysis, the high eccentricity limit near merger is fairly unconstrained. We highlight that this is a common feature for all current eccentric waveform models in the literature.

Finally, to ensure the analyses of GW200129, GW190701, GW200208_22, and GW190521 do not depend on the sampler, we perform additional pBilby analyses using SEOBNRv4E (SEOBNRv4EHM but turning off the higher modes) of these events in Fig. 7.

### G. Events with mild eccentricity support

We find marginal evidence for eccentricity in GW190620_030421. When analyzed with SEOBNRv4EHM, we observe this is a heavy BBH with support for a positive effective spin with $M_{\mathrm{src}} = 168.3^{+36.4}_{-34.9}$, $M_{\mathrm{det}} = 126.6^{+18.7}_{-17.9}$ and $\chi_{\mathrm{eff}} = 0.20^{+0.26}_{-0.27}$. Unlike the previously discussed events in this paper, GW190620_030421 was only detected in LIGO-Livingston. We find that $\log_{10}\mathcal{B}_{\mathrm{EAS/QCAS}} = 0.56$ with $e_{\mathrm{gw},10\,\mathrm{Hz}} = 0.30^{+0.19}_{-0.19}$. Due to the low Bayes factor, we do not consider it as having significant evidence for eccentricity. This event has shown similar Bayes factors for eccentricity in Refs. [20,23].

We also analyze GW191109_010717, which has shown signs of eccentricity, in Ref. [20]. When analyzed with SEOBNRv4EHM, we find this is a heavy BBH with $M_{\mathrm{src}} = 175.6^{+34.0}_{-30.0}$, $M_{\mathrm{det}} = 137^{+14.0}_{-14.4}$, and $\chi_{\mathrm{eff}} = -0.25^{+0.24}_{-0.27}$. We find $\log_{10}\mathcal{B}_{\mathrm{EAS/QCAS}} = 0.07$ with $e_{\mathrm{gw},10\,\mathrm{Hz}} = 0.26^{+0.24}_{-0.22}$

for this event. Interestingly, the posterior does rail against the upper bound of the prior, but due to the eccentricity limit enforced by SEOBNRv4EHM, we do not increase the upper bound. This event also has two peaks in the eccentricity posterior with one at $e_{\mathrm{gw,10\ Hz}} = 0.27$ and the other and the edge of the prior $e_{\mathrm{gw,10\ Hz}} = 0.50$. This was also noted in Ref. [20].

While these two events individually do not have a high $\mathcal{B}_{\mathrm{EAS/QCAS}}$, they do contribute to the population level analysis (see Sec. II B).

## V. WAVEFORM SYSTEMATICS

### A. Biases from neglecting eccentricity

When inferring source parameters with a waveform model that does not include the effect of eccentricity, one can bias the inferred source parameters. This effect is particularly pronounced in the three events that show signs for eccentricity where biases in the chirp mass and effective spin are observed. The results of this analysis are shown in Fig. 8. One of the main effects is that the eccentricity

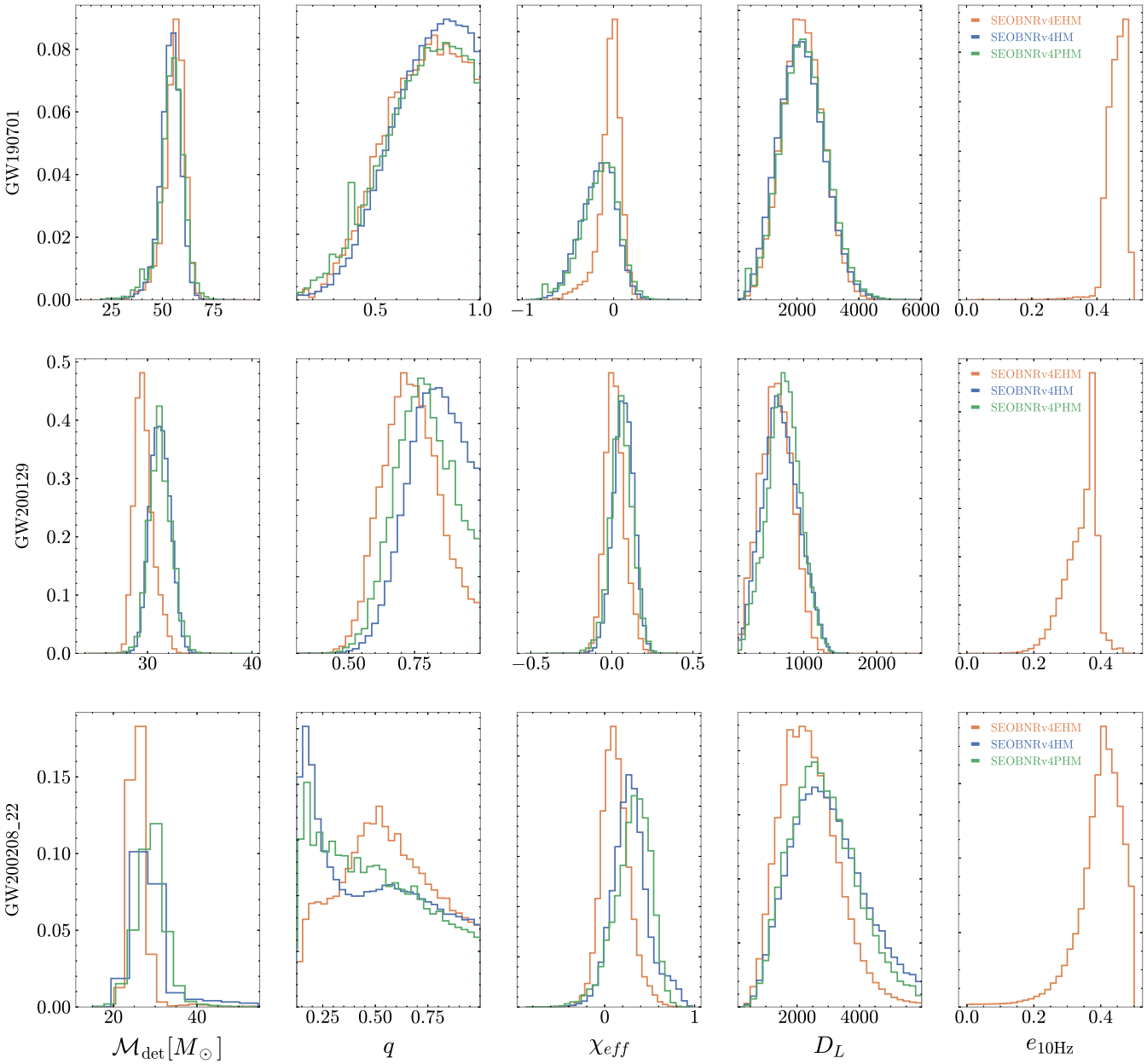


FIG. 8. Posterior distributions for the three candidate eccentric events analyzed with SEOBNRv4EHM, SEOBNRv4PHM, and SEOBNRv4HM. The posteriors were obtained by Dingo and then importance sampled (see Sec. II C). We note the SEOBNRv4PHM posteriors are in qualitative agreement with the LVK results [125]. When ignoring the effects of eccentricity, we see large differences in the $\mathcal{M}_{\mathrm{det}}$ and $\chi_{\mathrm{eff}}$. Noting that eccentricity decreases the time to merger with respect to quasicircular templates, the biases can be understood as compensations by $\mathcal{M}_{\mathrm{det}}$ and $\chi_{\mathrm{eff}}$ to keep the time to merger fixed.

reduces the time to merger. To compensate for this, other parameters must change, keeping the true time to merger fixed. In the cases of GW200129 and GW200208_22, the chirp mass decreases to keep a fixed time to merger. We observe mean chirp-mass differences between SEOBNRv4EHM and SEOBNRv4HM of 5.2% ($-1.54M_\odot$) for GW200129, 3.6% ($2.00M_\odot$) for GW190701, and 11.8% ($-3.08M_\odot$) for GW200208_22. This corresponds to a JSD differences of $3.78 \times 10^{-1}$ bits, $4.01 \times 10^{-2}$ bits, and $1.99 \times 10^{-1}$ bits for GW200129, GW190701, and GW20028_22, respectively. We observe chirp-mass differences between SEOBNRv4EHM and SEOBNRv4PHM of 5.2% ($-1.56M_\odot$) for GW200129, 2.4% ($1.32M_\odot$) for GW190701, and 11.6% ($-3.03M_\odot$) for GW200208_22. This corresponds to JSD differences of $3.55 \times 10^{-1}$ bits, $2.21 \times 10^{-2}$ bits, and $3.03 \times 10^{-1}$ bits for GW200129, GW190701, and GW200208_22, respectively.

There is also a bias in $\chi_{\rm eff}$ across the events. Comparing SEOBNRv4EHM and SEOBNRv4HM we observe differences of $-0.04$, 0.12, and $-0.19$ in the mean $\chi_{\rm eff}$ for GW200129, GW190701, and GW200208_22, respectively. This corresponds to JSD differences of $1.27 \times 10^{-1}$ bits, $1.50 \times 10^{-1}$ bits, and $1.58 \times 10^{-1}$ bits for GW200129, GW190701, and GW200208_22, respectively. In conclusion, when including the effect of eccentricity in these events, the $\chi_{\rm eff}$ distribution tends towards 0.

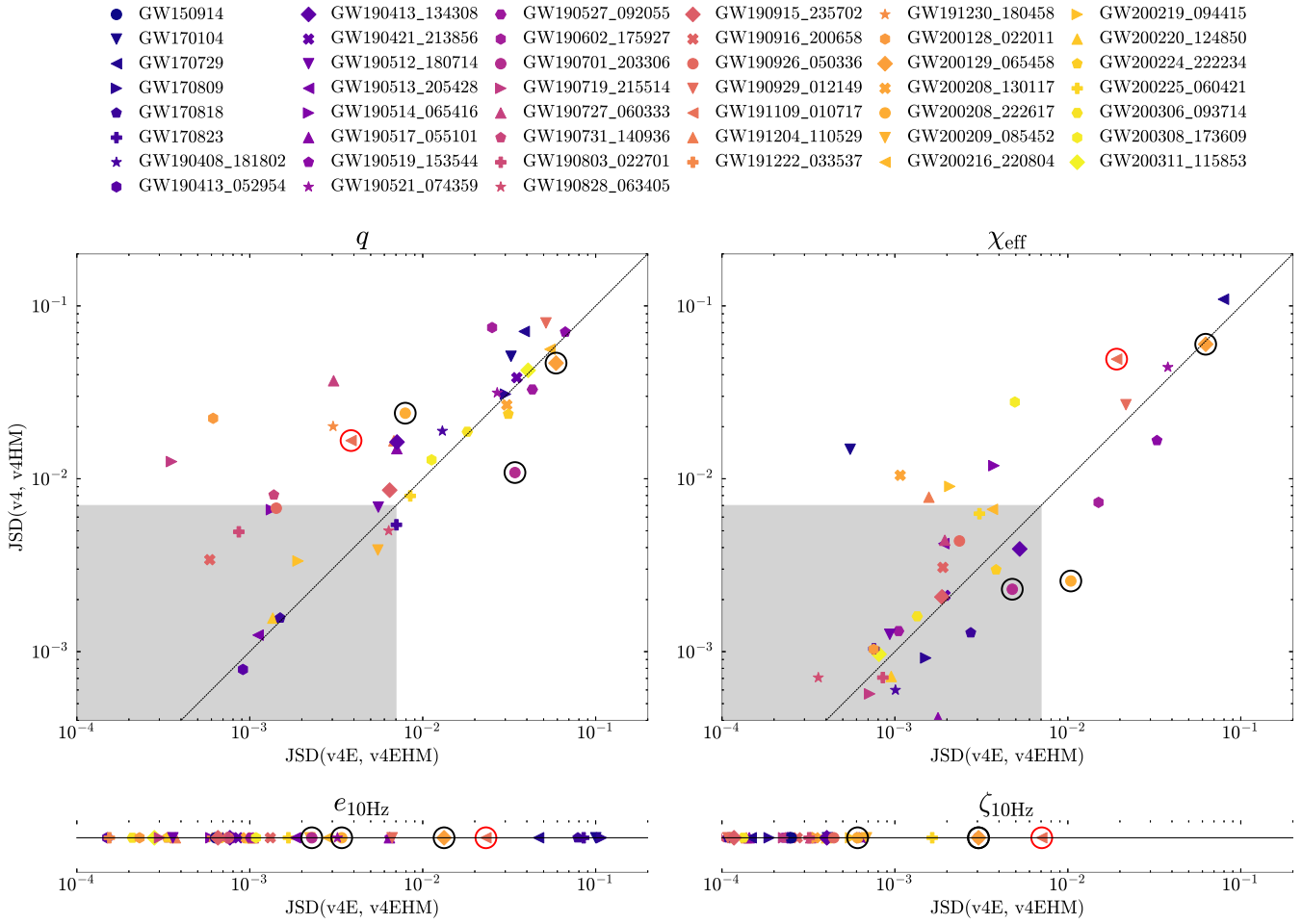


FIG. 9. JSDs of one-dimensional marginals when including or not including higher modes in GWs. Each point represents a GW event and contains four (top) or two (bottom) posterior distributions. In the top plot, the $y$-axis shows the JSD between SEOBNRv4 and SEOBNRv4HM in bits. On the top and bottom plots, the $x$-axis shows the JSD between SEOBNRv4 and SEOBNRv4EHM in bits. The title of the plots indicate which one-dimensional marginal is being compared (in order, mass ratio, effective spin, eccentricity, and relativistic anomaly). The gray section indicates the region in which the JSD is less than 0.007 bits. For a Gaussian, this corresponds to a 20% shift in the mean measured in standard deviations of the Gaussian. Events to the right of the diagonal line represent events for which the eccentric higher modes are important. For events like GW190701, GW200208_22, and GW200129 (circled in black), which show signs of eccentricity, there are larger JSDs between SEOBNRv4 and SEOBNRv4EHM than SEOBNRv4 and SEOBNRv4HM. In addition, higher modes are important for the analysis of GW191109_010717 (circled in red), as they cause large deviations in the eccentricity and relativistic anomaly posterior.

### B. Biases from neglecting higher modes in eccentric waveforms

We investigate the impact of neglecting higher modes beyond the $(\ell, |m|) = (2, 2)$ mode in the estimation of source parameters. It has been shown that neglecting them in quasicircular models can lead to biases in parameter estimation [2,233–237]. Here we extend the study to eccentric waveforms. We quantify this by calculating the JSD between the analysis performed with SEOBNRv4E and SEOBNRv4EHM. For comparison, we also compute the JSDs for SEOBNRv4 and SEOBNRv4HM. We follow Ref. [2] and consider deviations beyond 0.007 bits as significant biases. For a Gaussian, this corresponds to a 20% shift in the mean measured in standard deviations of the Gaussian. (We remark that 0.002 bits is the expected stochastic variation from GW sampling algorithms [165]).

First, we find that there are biases in the eccentricity distribution when not including higher modes. This is especially true for GW191109_010717, which can be seen in Fig. 9. In particular, we see that $e_{10\,\mathrm{Hz}}$ is boosted to higher values and leads to a JSD of 0.025 bits when using only the $(\ell, |m|) = (2, 2)$ mode. To rephrase, neglecting eccentricity results in increasing the mean eccentricity by 0.034. For this event, neglecting higher modes also leads to larger Bayes factors. When only using the $(\ell, |m|) = (2, 2)$ mode, $\log_{10} \mathcal{B}_{\mathrm{EAS/QCAS}} = 0.32$, but when using higher modes, $\log_{10} \mathcal{B}_{\mathrm{EAS/QCAS}} = 0.07$.

Furthermore, neglecting higher modes in eccentric waveforms can lead to biases in source parameters other than the eccentricity. For example, the inclusion of higher modes in eccentric waveforms for GW190701 leads to a bias (0.03 bits) in the mass ratio. In contrast, when neglecting higher modes in the quasicircular waveforms (that is, comparing SEOBNRv4 to SEOBNRv4HM), we see lower difference (0.01 bits). This is also true of the $\chi_{\mathrm{eff}}$ distribution of GW200208_22, where neglecting higher modes in eccentric waveforms leads to a 0.01 bit difference, whereas neglecting higher modes in quasicircular waveforms only leads to a 0.002 bit difference.

## VI. ODDS RATIOS AND $p_{\mathrm{ecc}}$

### A. Prior odds and odds ratio

We now turn our attention to computing the odds ratio in Eq. (2.4) by taking into account the effect of astrophysical prior odds on our observations. This is important, as the current prior (uniform in eccentricity) and prior odds (equal odds) assume that each event is equally likely to be eccentric or not. To do this, we first put a prior on the rate of eccentric BBHs, $R_{\mathrm{E}}$, and quasicircular BBHs, $R_{\mathrm{QC}}$, that we expect. We then take the maximum probability of this prior to estimate the prior odds.

We define $R_{\mathrm{E}}$ as the number of events with $e_{10\,\mathrm{Hz}} > 0.05$ per year within a luminosity distance of 6000 Mpc ($z < 0.9$) [96]. The reason we select $z < 0.9$ is because this is the maximum distance we consider in the analysis. Similarly, we define $R_{\mathrm{QC}}$ as the number of events with $e_{10\,\mathrm{Hz}} < 0.05$, again within $z < 0.9$.

The first step is to place a prior on the merger rate of eccentric and quasicircular events based on theoretical predictions.[7] We consider four binary formation environments that may lead to BBHs. The principal difference between these formation environments is the cluster escape speed, which increases the number of dynamical encounters [68]. We consider nuclear-star clusters (NSCs), globular clusters (GCs), young-star clusters (YSCs) and isolated binaries. We assume that each channel is independent and contributes some rate of eccentric events, $R_{\mathrm{E}}^{c}$, and some rate of quasicircular events, $R_{\mathrm{QC}}^{c}$. The superscript $c$ denotes the name of the channel. Each of these channels contribute to the total rate of eccentric or quasicircular events, as follows:

$$\begin{aligned} R_{\mathrm{E}} &= R_{\mathrm{E}}^{\mathrm{GC}} + R_{\mathrm{E}}^{\mathrm{NSC}} + R_{\mathrm{E}}^{\mathrm{YSC}} + R_{\mathrm{E}}^{\mathrm{IB}} \\ R_{\mathrm{QC}} &= R_{\mathrm{QC}}^{\mathrm{GC}} + R_{\mathrm{QC}}^{\mathrm{NSC}} + R_{\mathrm{QC}}^{\mathrm{YSC}} + R_{\mathrm{QC}}^{\mathrm{IB}}. \end{aligned} \tag{6.1}$$

We can then write the prior over the total rates as a convolution over the channel rates, as follows:

$$\begin{aligned} p(R_{\mathrm{E}}, R_{\mathrm{QC}}) = p(R_{\mathrm{E}}^{\mathrm{GC}}, R_{\mathrm{QC}}^{\mathrm{GC}}) * p(R_{\mathrm{E}}^{\mathrm{NSC}}, R_{\mathrm{QC}}^{\mathrm{NSC}}) \\ * p(R_{\mathrm{E}}^{\mathrm{ysc}}, R_{\mathrm{QC}}^{\mathrm{ysc}}) * p(R_{\mathrm{E}}^{\mathrm{IB}}, R_{\mathrm{QC}}^{\mathrm{IB}}). \end{aligned} \tag{6.2}$$

In the literature, the total rates from each channel (denoted $R^{c}$) and the fraction of the total rate that have $e_{10\,\mathrm{Hz}} > 0.05$ (denoted $\gamma^{c}$) are reported [88,91,238,239]. Thus, we place a prior on $R^{c}$ and $\gamma^{c}$ and do a change of variables to obtain $p(R_{\mathrm{E}}^{c}, R_{\mathrm{QC}}^{c})$. Explicitly, this change of variables is

$$p(R_{E}^{c}, R_{QC}^{c}) = p(R^{c}, \gamma^{c}) \left[ \frac{1}{\gamma^{c} R^{c}} - \frac{1}{(1-\gamma^{c}) R^{c}} \right], \tag{6.3}$$

where the term in the brackets is the Jacobian transformation between $(R_{\mathrm{E}}^{c}, R_{\mathrm{QC}}^{c})$ and $(R^{c}, \gamma^{c})$.

We first discuss the priors on the fractional rates, $\gamma^{c}$. NSCs can host BBH mergers due to the high density ($2 \times 10^{4}$ pc$^{-1}$) of BHs [70–73,77,89,240–243]. Mergers can also be induced by dynamical friction in the galactic disc [244–250]. The high BH density in NSCs leads to GW captures, which lead to high eccentricities ($e_{10\,\mathrm{Hz}} > 0.1$) [77,80,81,239,251–253]. If binary-single BH interactions are constrained to the nuclear disc, 10%–70% of mergers have $e_{10\,\mathrm{Hz}} > 0.1$, whereas if interactions are isotropic, then 8%–30% of mergers have $e_{10\,\mathrm{Hz}} > 0.03$ [89].

[7] An important caveat is that the $e_{10\,\mathrm{Hz}}$ reported in astrophysical studies is *not* the same as the $e_{10\,\mathrm{Hz}}$ in the quasi-Keplerian parametrization [Eq. (3.1)] [86]. Since the point which we use to define the rate is $e_{10\,\mathrm{Hz}} \approx 0.05$ and the discrepancy between the two definitions becomes relevant at $e_{10\,\mathrm{Hz}} \geq 0.2$, we do not expect this to be a significant issue for defining the heuristic prior.

TABLE II. Priors on the fractional rate of eccentric BBH mergers, $\gamma^c$ and total rate of BBH mergers $R^c$ in each formation channel within $z < 0.9$. Here Unif$[a, b]$ is a uniform distribution with upper and lower bound of $a$ and $b$, respectively. $\tilde{\mathcal{N}}[c, d]$ is a truncated normal distribution with mean and standard deviation $c$ and $d$, respectively, with truncation bounds of 0 and 1.

| Formation environment | $p(\gamma^c)$ | $p(R^c)$ mergers/yr |
|---|---|---|
| Nuclear-star cluster | Unif$[0.08, 0.7]$ | Unif$[119, 292]$ |
| Globular cluster | $\tilde{\mathcal{N}}(0.06, 0.03)$ | Unif$[375, 1492]$ |
| Young-star cluster | $\delta(0)$ | Unif$[502, 2325]$ |
| Isolated binary | $\delta(0)$ | Unif$[639, 31939]$ |

Thus, we place a uniform prior on $\gamma^{\rm NSC}$ with a minimum of 8% and a maximum of 70%.

GC environments can also host BBH mergers due to the high density of BHs [70–73]. Reference [87] finds $\gamma_{\rm GC} \sim 6\%$; Ref. [239] finds similar results with a PN calculation. This method includes PN corrections to encounters between BHs and BBHs using techniques developed in Refs. [88,254,255], which lead to non-negligible eccentricity. Thus, we place a truncated Gaussian prior around $\gamma^{\rm GC} = 6\%$ with a standard deviation of 3%, which comes from the variation in the cluster escape velocity (see Fig. 3 of Ref. [239]).

Studies on the rate of eccentric mergers in YSCs are less common than NSCs or GCs (see however, Refs. [82,238]). Reference [238] finds less than 0.08% of mergers in YSCs have $e_{10\ \rm Hz} > 0.1$ from binary-single interactions. Thus, we neglect this effect and set $p(\gamma^{\rm YSC}) = \delta(0)$. Similarly, in IBs, we expect $p(\gamma^{\rm IB}) = \delta(0)$ as the binaries circularize before merger [41,195].

We now turn to placing a prior over the total rates from each channel, $p(R^c)$. There have been a number of studies estimating the rate density of NSCs [256,257], GCs [87,258–260], YSCs [261–263], and IBs [18,263–265]. In the following, we use the rate estimates from Ref. [266], as they model the IB and NSC, GC, and YSC pathways with the same input physics/assumptions. See Table 1 in Ref. [266] for the initial conditions/priors of the simulations. Since we are interested in the merger rate of BBHs within $z < 0.9$ and not the merger rate density as a function of redshift, which is computed in Ref. [266], we may write $R^c$ as

$$R^c = \int_0^{0.9} dz \mathcal{R}(z) \frac{dV}{dz} \frac{1}{1+z}. \tag{6.4}$$

Here, $\mathcal{R}(z)$ is the volumetric rate density in units of mergers Gpc$^{-3}$ yr$^{-1}$ as a function of redshift and $dV/dz$ is the differential comoving volume. The $\frac{1}{1+z}$ accounts for the fact that $\mathcal{R}(z)$ is in the source frame, whereas we want $R^c$ in the observer frame. We can perform the integration for the set of simulations listed in Ref. [266] and set lower and upper bounds on the rates. Then, we assume that $R^c$ is drawn from uniform distribution between these bounds. The final priors on $\gamma^c$, $R^c$ are summarized in Table II. The prior can be seen in one-dimensional marginals on the left plot in Fig. 10.

The maximum probability of the prior occurs when $R_{\rm E}/R_{\rm QC} = 0.023$, and thus we quote this value for our prior

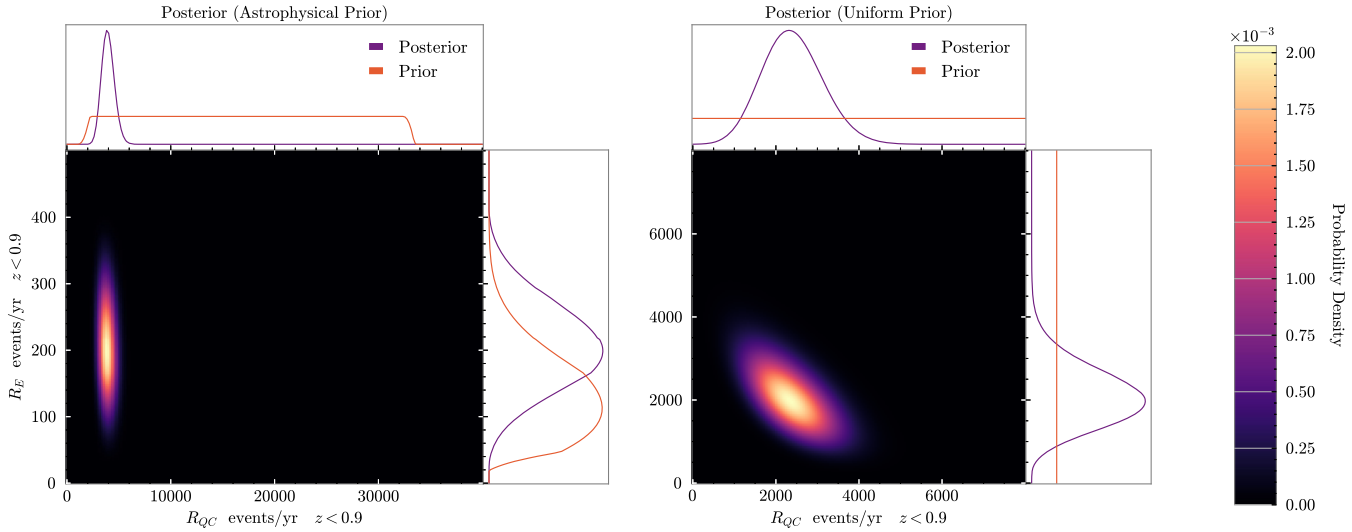


FIG. 10. Posterior distribution for the rate of eccentric $R_{\rm E}$ and quasicircular $R_{\rm QC}$ events per year within $z < 0.9$. This is computed using the formalism of Ref. [134] (see Sec. II B). Left: rate estimate combining the astrophysical prior with the GW data. One can see that the posterior on $R_{\rm E}$ shifts towards higher values of compared to the prior on $R_{\rm E}$. Right: rate distribution estimated from GWs when using a uniform prior for $R_{\rm E}$ and $R_{\rm QC}$. In this case, the quasicircular and eccentric rates are similar, since for the majority of event, we cannot distinguish if $e_{10\ \rm Hz} < 0.05$ or $e_{10\ \rm Hz} > 0.05$ from the data alone. Note the scales on the plots are different.

odds. Now using Eq. (2.4), we obtain

$$\begin{aligned}\log_{10}\mathcal{O}_{\mathrm{EAS/QCAS}} &= 0.2-3.11 \quad \text{for GW200129},\\ &= 1.36 \quad \text{for GW190701},\\ &= 0.13 \quad \text{for GW200208\_22}.\end{aligned}$$

### B. Computing $p_{\mathrm{ecc}}$ for three events

We now compute the rate of eccentric and quasicircular events using GW observations. We then use these rates to estimate the probability an event is eccentric for the three GW events considered in Sec. IV. This is done by using the formalism in Eqs. (2.5)–(2.16). The rates obtained with this analysis using an astrophysical prior and a uniform prior over the rates is shown in Fig. 10.

We also include selection effects in this estimate. To do so we compute $\alpha_{\mathrm{QC}}$ and $\alpha_{\mathrm{E}}$ with Eq. (2.15). For the prior, we use a power-law–peak distribution with hyperparameters of the maximum-likelihood point of the LVK analysis [13]. In addition, for any parameters that are outside the prior, ($m_1 < 10M_\odot$, $m_2 < 10M_\odot$, $q < 0.125$, or $d_L > 6,000$ Mpc), we set $p_{\mathrm{QC,det}}(\vartheta) = p_{\mathrm{E,det}}(\vartheta) = 0$. Due to the fact that the selection function also depends on the PSD, we compute $\alpha_{\mathrm{QC}}$ and $\alpha_{\mathrm{E}}$ for each observing run. We then take a weighted average of the $\alpha$'s where the weights are determined by the joint duty cycle of LIGO-Hanford and LIGO-Livingston for each observing run (49 days, 118 days, 107 days, and 96 days for O1, O2, O3a, and O3b, respectively). We also computed $\alpha_{\mathrm{QC}}$ and $\alpha_{\mathrm{E}}$ by marginalizing over the population uncertainty. That is, we also sampled over the population posterior when computing Eq. (2.15). However, given that there is only a 2% error compared to the maximum-likelihood estimate, we use the maximum-likelihood estimate of $\alpha_{\mathrm{QC}}$ and $\alpha_{\mathrm{E}}$ in the rest of the calculations.

There are a few interesting observations to make about Fig. 10. First, there is a large difference in $p(R_{\mathrm{E}}|\{d_i\},N)$ when using an astrophysical prior versus a uniform one. Specifically, the astrophysical prior has a strong influence over the eccentric rate. The reason for this that the uncertainty on the fraction of eccentric BBHs quoted in Sec. VI A is small compared to the uncertainty on the fraction of eccentric BBHs from GWs. The latter uncertainty can be seen by noticing that in Fig. 2, the majority of events have $-1 < \log_{10}\mathcal{B}_{\mathrm{EAS/QCAS}} < 1$ as opposed to $\log_{10}\mathcal{B}_{\mathrm{EAS/QCAS}} \ll -1$. In other words, if we just consider the data, it is hard to say the majority of events are definitely *not* eccentric. With better detector sensitivities, perhaps we can better separate the populations. This is also the reason that when using a uniform prior on the rate of eccentric and quasicircular BBHs, the mean of $p(R_{\mathrm{E}}|\{d_i\},N)$ is only larger than $p(R_{\mathrm{QC}}|\{d_i\},N)$ by 14% (361 events/yr).

In contrast, the astrophysical prior does not have the same effect on $p(R_{\mathrm{QC}}|\{d_i\},N)$. Here, $p(R_{\mathrm{QC}}|\{d_i\},N)$ is dominated by the information from the data. This effect can be attributed to the large uncertainty in the rate of quasicircular events from astrophysical simulations [266].

We can compute the probability that particular GWs are eccentric, $p_{\mathrm{ecc}}$, using Eq. (2.11). Again, due to the variety of glitch mitigation techniques in GW200129, we have a range of $p_{\mathrm{ecc}}$'s. This uncertainty now also propagates into events other than GW200129, as $p_{\mathrm{ecc}}$ for each event is also conditioned on the GW data from GW200129. When using an astrophysical prior on the rates, we obtain

$$\begin{aligned}p_{\mathrm{ecc}} &= 0.7490\text{–}0.9995 \quad \text{for GW200129},\\ &= 0.9763\text{–}0.9774 \quad \text{for GW190701},\\ &= 0.7197\text{–}0.7286 \quad \text{for GW200208\_22}.\end{aligned} \tag{6.5}$$

When using a uniform prior on the rates, we find that

$$\begin{aligned}p_{\mathrm{ecc}} &= 0.9800\text{–}0.99998 \quad \text{for GW200129},\\ &= 0.9986\text{–}0.9986 \quad \text{for GW190701},\\ &= 0.9769\text{–}0.9771 \quad \text{for GW200208\_22}.\end{aligned} \tag{6.6}$$

The value of $p_{\mathrm{ecc}}$ from the uniform prior provides a useful comparison to quantify the effect of the prior, while the value of $p_{\mathrm{ecc}}$ from the astrophysical prior, as explained above, is more realistic.

We can now compute the probability that there exists at least one event which is eccentric in the population. First, we give a back-of-the-envelope computation of $p_{\mathrm{ecc,pop}}$ using only $\mathcal{O}_{\mathrm{EAS/QCAS}}$. We stress that this is *not* a robust estimate, as it assumes that the inferred rate of eccentric and quasicircular BBHs is not influenced by GW observations. In addition, it does not marginalize over the astrophysical uncertainty on the rates. This calculation is meant to give an intuition and sanity check on the machinery in Sec. II B. We can use Eq. (2.12) to map the odds ratios of the analyzed events to the interval [0, 1]. We can then combine the events by computing

$$\tilde{p}_{\mathrm{ecc,pop}} = 1 - \prod_{i=1}^{N}[1-\tilde{p}_{\mathrm{ecc}}(i)]. \tag{6.7}$$

If we use `BayesWave A` glitch mitigation on GW200129, we recover $\tilde{p}_{\mathrm{ecc,pop}} = 99.8\%$. We can also perform the same calculation, but only use the three events that show signs of eccentricity. In this case, we find $\tilde{p}_{\mathrm{ecc,pop}} = 99.3\%$.

Finally, we can use the machinery in Eqs. (2.13), and (B1)–(B7) to robustly compute the probability that there is at least one eccentric event in the population. When using an astrophysical prior on the rates, we find

$$\begin{aligned}p_{\mathrm{ecc,pop}} &> 1\text{–}8.4\times10^{-8} \text{ using } \texttt{gwsubtract},\\ &> 1\text{–}4.7\times10^{-3} \text{ using } \texttt{BayesWave A}.\end{aligned} \tag{6.8}$$

Just for comparison, we also compute $p_{\mathrm{ecc,pop}}$ when using a uniform prior on the rates, as follows:

$$p_{\rm ecc,pop} > 1\text{–}7.6\times10^{-14}\ \text{using}\ \texttt{gwsubtract},$$
$$> 1\text{–}6.2\times10^{-11}\ \text{using}\ \texttt{BayesWave A}. \quad (6.9)$$

We can also perform leave-one-out studies to see how much impact each individual event has on the $p_{\rm ecc,pop}$. In the following, we only report the numbers when using an astrophysical prior on the rates. In addition, we report the results using the `BayesWave A` glitch mitigation, which is the most conservative case. We find

$$p_{\rm ecc,pop} > 1\text{–}1.7\times10^{-2}\ \text{leaving out GW200129},$$
$$p_{\rm ecc,pop} > 1\text{–}1.6\times10^{-1}\ \text{leaving out GW190701},$$
$$p_{\rm ecc,pop} > 1\text{–}1.6\times10^{-2}\ \text{leaving out GW200208\_22}.$$

## VII. CONCLUSION

In this paper, we performed an analysis of 57 GWs using the multipolar eccentric nonprecessing waveform model SEOBNRv4EHM [136]. This waveform model includes eccentricity corrections to the GW multipoles up to the 2PN order, and allows for sampling in both the eccentricity and relativistic anomalies. This large scale analysis was made possible with the normalizing flow approach available with Dingo [156].

We compare Dingo with pBilby [137] using two zero-noise injections, and find consistency between the samplers. The posteriors are completely consistent with JSDs in the one-dimensional marginals less than 0.002 bits. This gives us confidence that for eccentric BBHs, Dingo is as accurate as standard samplers while operating at a fraction of the computational cost.

There are signs of eccentricity in three candidate events: GW200129, GW190701, and GW200208_22. We find $\log_{10}$ eccentric aligned-spin against quasicircular aligned-spin Bayes factors of 1.84–4.75 for GW200129, 3.0 for GW190701, and 1.77 for GW200208_22. We cannot say conclusively that these three binaries are eccentric; however, the eccentric hypothesis fits the data better than the quasicircular aligned-spin and quasicircular spin-precessing hypotheses. These signs indicate that eccentricity is an integral consideration in future and current parameter-estimation studies.

To our knowledge, this is the first time GW200129 has been fully sampled with an eccentric waveform model. In the appendix of Ref. [20], the authors tried to sample this event using the reweighting technique introduced in Ref. [267] with the waveform from Ref. [172]. The reweighting in Ref. [267] involves taking a quasicircular proposal distribution and importance sampling to an eccentric target distribution. However, for this event, the reweighting led to an effective sample size of one. This may be the case for events where the quasicircular proposal is significantly biased by the presence of eccentricity. By directly performing inference on the eccentric parameter, we are able to obtain over 5000 effective samples across all priors, glitch mitigation techniques and waveform models for this event.

We do see very strong evidence for eccentricity in GW200129 when using `gwsubtract` glitch mitigation. But when taking into account the astrophysical prior odds and other methods of glitch mitigation, we cannot conclude that GW200129 is eccentric. In particular the $\log_{10}$ odds ratio between the eccentric aligned-spin and quasicircular aligned-spin waveform is between 0.2–3.11. This implies the importance of robust glitch mitigation techniques and thorough comparisons between said techniques is crucial in current and future observing runs [216–218,222,223].

We also see signs of eccentricity in GW190701. However, because $\log_{10}$ eccentric aligned-spin against quasicircular spin-precessing odds ratio for this event is $<3.5$, we cannot conclude this event is eccentric. This event also has a glitch in it; however, we only have one glitch draw from the `BayesWave` glitch posterior [219]. In future studies, it will be critical to explicitly marginalize over the glitch posterior for this event, as was done in Ref. [217]. Given the nature of Dingo, marginalizing over different glitch realizations is straightforward.

We also find signs of eccentricity in GW200208_22. This has been reported previously in Ref. [20]. We see mild support for eccentricity in GW190620, which has been flagged as potentially eccentric first in Ref. [20], and then in Ref. [23].

We do not observe evidence of eccentricity in GW190521 in the region $e_{10\,\rm Hz} < 0.5$. This is in contention with Ref. [21]. However, Ref. [23], which uses the `TEOBResumS-DALI` waveform model [152–154], finds similar results. It is at present unclear what the cause of this discrepancy is, and further work in this direction is needed. Note, our result is not immediately in contention with Ref. [113], which probes the parameter space of non-spinning hyperbolic captures which is separate from eccentric inspiral-merger-ringdown waveforms. It is also not immediately in contention with Ref. [110], which probes the eccentricity at merger with numerical relativity simulations and a maximum likelihood test.

We also see marginal support for eccentricity in GW190620_030421 and GW191109_010717, which is broadly in agreement with previous eccentric parameter estimation studies [20,23].

We also perform a study of the effect of higher modes beyond the $(\ell, m) = (2, 2)$ mode in eccentric waveform models. We find that there are biases in the intrinsic parameters when one neglects higher modes in parameter-estimation studies. In the quasicircular case, this has been found in Refs. [2,233–237]. Our contribution is to study the biases which occur in the presence of eccentricity. We have quantified this effect by comparing the loss of information accumulated when neglecting higher modes in eccentric waveforms with the loss of information accumulated when neglecting higher modes in quasicircular waveforms. We find with GW191109_010717 that ignoring higher

modes leads to biases in the eccentricity distribution of 0.025 bits. For context, with a Gaussian, an 0.007 bit difference corresponds to a 20% shift in the mean measured in standard deviations of the Gaussian. In addition, if we neglect higher modes in GW191109_010717, the $\log_{10}$ Bayes factor changes from 0.07 to 0.32. We do not find in the events analyzed that neglecting higher modes leads to incorrectly finding evidence for eccentricity.

We also investigated the systematic effects of ignoring eccentricity completely in parameter-estimation studies. Similar studies have been performed in Refs. [23,24,92–102]. Our new contribution is to report the bias in the masses and spins for real events with support for $e_{10\,\mathrm{Hz}} > 0.1$. We find that when ignoring eccentricity, the chirp mass is biased by 5.2% for GW200129, 3.6% for GW190701, and 11.8% GW200208_22 with respect to the aligned-spin quasicircular case. Similarly, the $\chi_{\mathrm{eff}}$ is biased by $-0.04$ for GW200129, 0.12 for GW190701, and $-0.19$ for GW200208_22 (again for the aligned-spin quasicircular case).

Finally, we have performed a computation to measure the probability that a GW event is eccentric. This method is more robust than simply considering odds ratios, as it combines information from the ensemble of GW events with astrophysical predictions. It is analogous to $p_{\mathrm{astro}}$ in LVK searches [134]. As more GWs are observed, this method will give tighter constraints on the rate of eccentric and quasicircular events than simply using an astrophysical prior. This will lead to smaller uncertainty on the probability that individual events are eccentric. Currently, this method is limited to differentiating eccentric aligned-spin and quasicircular aligned-spin binaries. This is because there are no population synthesis codes that coherently model eccentricity and spin precession, so we cannot put reasonable priors on the relative rate between eccentric aligned-spin versus quasicircular spin-precessing binaries. Thus, we caveat population statements with the fact that we neglect spin precession when reporting $p_{\mathrm{ecc}}$ and $p_{\mathrm{ecc,pop}}$. This issue will be addressed in future work.

We find that $p_{\mathrm{ecc}} = 0.7490$–$0.9995$ for GW200129, $p_{\mathrm{ecc}} = 0.9763$–$0.9774$ for GW190701, and $p_{\mathrm{ecc}} = 0.7197$–$0.7286$ for GW200208_22 when using astrophysical priors. We extend this formalism to evaluate the probability that there exists an eccentric event in the population. We find this to be $p_{\mathrm{ecc,pop}} > 1$–$4.7 \times 10^{-3}$ when using `BayesWave A` glitch mitigation on GW200129 and $p_{\mathrm{ecc,pop}} > 1$–$8.4 \times 10^{-8}$ when using `gwsubtract` glitch mitigation on GW200129.

The computational work for this manuscript was carried out on the compute clusters Saraswati, Lakshmi, and Hypatia at the Max Planck Institute for Gravitational Physics in Potsdam. Training of networks was also carried out on the Atlas cluster at the Max Planck Institute for Intelligent Systems in Tübingen. Dingo is publicly available through the PYTHON package dingo-gw at https://github.com/dingo-gw/dingo. Stable versions of Dingo are published through conda, and can be installed via conda install -c conda-forge dingo-gw.

## ACKNOWLEDGMENTS

It is our pleasure to thank Héctor Estellés for useful discussions during the project especially related to the computation of the kick velocity of GW200129. We would like to thank Alexandre Toubiana for providing the code to generate samples from the power-law-peak LVK distribution. We thank Vivien Raymond for chairing the LVK Collaboration internal review of Dingo. We thank Alan Knee and Jess McIver for their useful interactions in the early stages of this project. We would like to thank Arif Shaikh for the LSC Publication & Presentation Committee review of this manuscript. A. R. B. was supported in the last stages of this work by the Dutch Research Council (NWO) through the Veni project VI.Veni.222.396. This research has made use of data or software obtained from the Gravitational Wave Open Science Center (gwosc.org), a service of the LIGO Scientific Collaboration, the Virgo Collaboration, and KAGRA. This material is based upon work supported by NSF's LIGO Laboratory which is a major facility fully funded by the National Science Foundation, as well as the Science and Technology Facilities Council (STFC) of the United Kingdom, the Max-Planck-Society (MPS), and the State of Niedersachsen/Germany for support of the construction of Advanced LIGO and construction and operation of the GEO600 detector. Additional support for Advanced LIGO was provided by the Australian Research Council. Virgo is funded, through the European Gravitational Observatory (EGO), by the French Centre National de Recherche Scientifique (CNRS), the Italian Istituto Nazionale di Fisica Nucleare (INFN) and the Dutch Nikhef, with contributions by institutions from Belgium, Germany, Greece, Hungary, Ireland, Japan, Monaco, Poland, Portugal, and Spain. K. A. G. R. A. is supported by Ministry of Education, Culture, Sports, Science and Technology (MEXT), Japan Society for the Promotion of Science (JSPS) in Japan; National Research Foundation (NRF) and Ministry of Science and ICT (MSIT) in Korea; Academia Sinica (AS) and National Science and Technology Council (NSTC) in Taiwan. Virgo is funded, through the European Gravitational Observatory (EGO), by the French Centre National de Recherche Scientifique (CNRS), the Italian Istituto Nazionale di Fisica Nucleare (INFN) and the Dutch Nikhef, with contributions by institutions from Belgium, Germany, Greece, Hungary, Ireland, Japan, Monaco, Poland, Portugal, and Spain. K. A. G. R. A. is supported by Ministry of Education, Culture, Sports, Science and Technology (MEXT), Japan Society for the Promotion of Science (JSPS) in Japan; National Research Foundation (NRF) and Ministry of Science and ICT (MSIT) in Korea; Academia Sinica (AS) and National Science and Technology Council

(NSTC) in Taiwan. M. P. was supported by NSF Grants No. AST-2407453 and No. PHY-2512902.

## APPENDIX A: ECCENTRICITY ESTIMATES FROM SINGLE DETECTOR NETWORKS

GW200129 was detected in LIGO-Hanford, LIGO-Livingston, and VIRGO. In the main text, we perform inference using the combined data from LIGO-Hanford and LIGO-Livingston. However, due to the glitch in LIGO-Livingston, it is useful to seperate the analysis into single detector analyses. This was also performed in Ref. [217]. As shown in Fig. 11, the majority of evidence for eccentricity comes from LIGO-Livingston. There is still marginal support for eccentricity in the Hanford-only analysis with $\log_{10}\mathcal{B}_{\mathrm{EAS/QCAS}} = 0.86$. Interestingly, the maximum likelihood of the Hanford-only analysis peaks at $e_{10\ \mathrm{Hz}} = 0.40$.

The difference in the Bayes factors between Hanford and Livingston can be explained by the lack of SNR in Hanford. The SNR in Livingston is 22, whereas the SNR in Hanford is only 14. The difference in SNR is due to the particular antenna patterns for this event. We can take the max-likelihood waveform of GW200129 analyzed in both detectors and compute $F_+^2 + F_\times^2$ [145] to get an order of magnitude estimate of the impact of the detector projection.

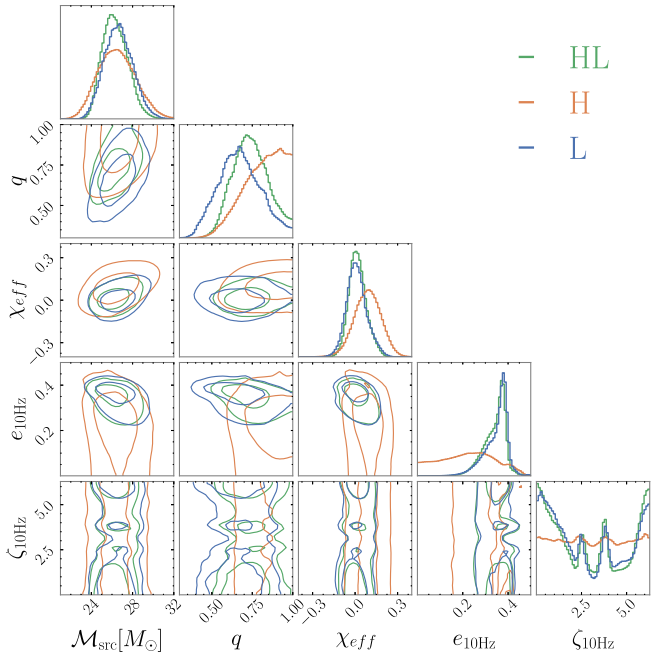


FIG. 11. Analysis of GW200129 using LIGO-Hanford and LIGO-Livingston (HL), LIGO Hanford (H), and LIGO-Livingston (L). We observe that the evidence for eccentricity comes largely from the LIGO-Livingston detector. The `gwsubtract` glitch subtraction is being used when using the Livingston detector. There is no glitch in the Hanford detector.

We find that for Hanford, $F_+^2 + F_\times^2 = 0.53$ and for Livingston, $F_+^2 + F_\times^2 = 0.92$.

We can then ask if the lack of evidence of eccentricity in Hanford is due to low SNR. To do this, we perform an injection recovery using the max-likelihood parameters of GW200129 analyzed with Hanford. The maximum likelihood point of the Hanford-only analysis peaks at $e_{10\ \mathrm{Hz}} = 0.40$. If we decrease $d_L$ of the injection to artificially set the SNR to 22, we see a peak in the eccentricity posterior. However, performing the same injection with lower SNR yields a eccentricity posterior much closer to the prior. This implies the reason there is only a small bump in the eccentricity in Hanford is due to the lack of SNR in the detector, rather than the lack of evidence for eccentricity.

## APPENDIX B: LOWER BOUND ON $p_{\mathrm{ecc,pop}}$

In order to compute $p_{\mathrm{ecc,pop}}$ we must compute $p(\{g_i = 0\}|\{d_i\}, N)$. However, to do this, we need to normalize the distribution $p(\{g_i\}|\{d_i\}, N)$. Note that

$$\begin{aligned} 1 &= \sum_{\{g_i\}} p(\{g_i\}|\{d_i\}, N) \\ &= \sum_{\{g_i\}} \int dR_{\mathrm{E}} dR_{\mathrm{QC}}\, p(\{g_i\}, R_{\mathrm{E}}, R_{\mathrm{QC}}|\{d_i\}, N). \end{aligned} \tag{B1}$$

We do not have the normalization over $p(\{g_i\}, R_{\mathrm{E}}, R_{\mathrm{QC}}|\{d_i\}, N)$, but we can rewrite Eq. (B1) as

$$\beta = \sum_{\{g_i\}} \left[\prod_{\{i|g_i=1\}}^{N_{\mathrm{E}}} Z_{\mathrm{E}}(d_i)\right]\left[\prod_{\{i|g_i=0\}}^{N_{\mathrm{QC}}} Z_{\mathrm{QC}}(d_i)\right] I(\{g_i\}), \tag{B2}$$

where $\beta$ is the normalization of $p(\{g_i\}, R_{\mathrm{E}}, R_{\mathrm{QC}}|\{d_i\}, N)$ and $I(\{g_i\})$ is an evidence independent integral over the rates

$$\begin{aligned} I(\{g_i\}) = \int dR_{\mathrm{E}} dR_{\mathrm{QC}} R_{\mathrm{E}}^{\sum g_i} R_{\mathrm{QC}}^{\sum (1-g_i)} \\ \times e^{-(\alpha_{\mathrm{E}} R_{\mathrm{E}} + \alpha_{\mathrm{QC}} R_{\mathrm{QC}})} p(R_{\mathrm{E}}, R_{\mathrm{QC}}), \end{aligned} \tag{B3}$$

which depends only on the number of eccentric and quasicircular flags and the prior over the rates.

In principle, we can compute the sum in Eq. (B2) exactly. However, the sum has $2^N$ elements, so if all the summands are important, this will become infeasible. Instead, if we can identify dominant terms in the sum, we can place a lower bound on $\beta$. Then we can put an upper bound on $p(\{g_i = 0\}|\{d_i\})$, which translates to a lower bound on $p_{\mathrm{ecc,pop}}$. So the larger the lower bound we can place on $\beta$, the larger the lower bound we can place on $p_{\mathrm{ecc,pop}}$. Thus, our goal is to now eliminate small terms from the sum to get as large a lower bound as possible.

There are two scenarios to consider: using a uniform prior or using an astrophysical prior. If we use a uniform

prior, each $I(\{g_i\})$ is of the same order in Eq. (B2). Thus the $\{g_i\}$ which contribute the most in the sum are those which select the events with $Z_{\rm E} \gg Z_{\rm QC}$ or $Z_{\rm E} \ll Z_{\rm QC}$. Given that we have no events with $Z_{\rm E} \ll Z_{\rm QC}$ (see Fig. 2), we focus on cases where $Z_{\rm E} \gg Z_{\rm QC}$. Let $\{j_1, \ldots j_{N_{\rm E}}\}$ be the indexes of the $N_{\rm E}$ events with $Z_{\rm E} \gg Z_{\rm QC}$. We can remove any terms in Eq. (B2) which do not have at least one event with $Z_{\rm E} \gg Z_{\rm QC}$. That is, we remove $\{g_i\}$ with

$$\sum_{i \in \{j_1, \ldots j_{N_{\rm E}}\}} g_i = 0, \tag{B4}$$

from the sum. The normalization $\beta$ becomes

$$\begin{aligned}\beta > & \sum_{k=1}^{N_{\rm E}} \sum_{\{j_k\}}^{\binom{N_{\rm E}}{k}} \left[ \prod_{j_l \in \{j_k\}} Z_{\rm E}(d_{j_l}) \right] \\ & \times \sum_{\{g_i | i \notin \{j_k\}\}} \left[ \prod_{\{i | g_i = 1 \wedge i \notin \{j_k\}\}} Z_{\rm E}(d_i) \right] \left[ \prod_{\{i | g_i = 0 \wedge i \notin \{j_k\}\}} Z_{\rm QC}(d_i) \right] \\ & \times I(\{g_i\}),\end{aligned} \tag{B5}$$

where it is implied that $I(\{g_i\})$ here explicitly sets the $j_l$ flags to 1. In the first sum, we sum over the number of flags, $k$, which are set to 1 and have $Z_{\rm E} \gg Z_{\rm QC}$. The second sum represents the sum over the $N_{\rm E}$ choose $k$ combinations of flags with $Z_{\rm E} \gg Z_{\rm QC}$. Each, $\{j_k\}$ is shorthand for creating a set choosing $k$ elements from $\{j_1, \ldots j_{N_{\rm E}}\}$. These first two sums serve to separate the events with $Z_{\rm E} \gg Z_{\rm QC}$ from the events with $Z_{\rm E} \sim Z_{\rm QC}$. Finally, the last sum is over the $\{g_i\}$ with $Z_{\rm E} \sim Z_{\rm QC}$.

This last sum is still intractable, but we can note that each term in the last sum of Eq. (B5) is at least greater than $I_s \prod_i Z_s(d_i)$ where $Z_s(d_i) = \min(Z_{\rm E}(d_i), Z_{\rm QC}(d_i))$ and $I_s = \min_{\{g_i\}} I(\{g_i\})$. $I_s$ can be computed directly from Eq. (B3). We find that $I(\{g_i\})$ is minimized when $\sum g_i = N$ (in the uniform prior case this is also equivalent to the case where all the $\sum g_i = 0$ via symmetry). Thus, we can place a bound on $\beta$ of

$$\beta > \sum_{k=1}^{N_{\rm E}} \sum_{\{j_k\}}^{\binom{N_{\rm E}}{k}} \left[ \prod_{j_l \in \{j_k\}} Z_{\rm E}(d_{j_l}) \right] 2^{N - N_{\rm E}} \left[ \prod_{i}^{N-k} Z_s(d_i) \right] I_s. \tag{B6}$$

Here, the $2^{N-N_{\rm E}}$ comes from counting the number of terms in the last sum of Eq. (B5). In our case with $N_{\rm E} = 3$, this is a sum over only $3 + 1 + 3 = 7$ elements.

However, if we use an astrophysical prior, note $R_{\rm QC}$ has support for values much larger than $R_{\rm E}$ in the prior (see top left of Fig. 10). Thus, since $I(\{g_i\})$ has terms like $R_{\rm QC}^{\sum 1 - g_i}$ in the integrand, the $\{g_i\}$ with the largest $\sum 1 - g_i$ will dominate Eq. (B2). Thus, we can group terms which have all $g_i = 0$, terms which have all but one $g_i = 0$, terms which have all but two $g_i = 0$, and so on. In each grouping, the terms which contribute the most are those with at least one $g_{j_l} = 1$ with $j_l \in \{j_1 \ldots j_k\}$. The lower bound then becomes

$$\beta > \sum_{k=0}^{N_{\rm E}} \sum_{\{j_k\}}^{\binom{N_{\rm E}}{k}} \left[ \prod_{j_l \in \{j_k\}} Z_{\rm E}(d_{j_l}) \right] \left[ \prod_{i \notin \{j_k\}} Z_{\rm QC}(d_i) \right] I(\{g_i\}). \tag{B7}$$

## APPENDIX C: BACKGROUND DISTRIBUTION OF BAYES FACTORS

We further characterize the significance level of our observations by comparing our measured Bayes factors to an astrophysical background distribution. This is useful for mitigating the effect of the choice of eccentricity prior in the analysis as the background distribution is subject to the same prior effects. We do this test by first drawing samples from the maximum likelihood of the power-law–peak mass distribution with the DEFAULT spin model of the LVK [13]. Then we apply the selection function described in Eq. (91) of Ref. [268] and Sec. II B to this injection set. Here, we are using a noneccentric selection function, since we want to simulate the effect of a noneccentric background distribution on noneccentric LVK searches. We draw 550 injections (after selection) as this allows us to put significance levels on GW200208_22 and GW200129. We then inject SEOBNRv4HM waveforms and recover the posterior with SEOBNRv4EHM. Finally, we use the Savage-Dickey ratio to compute the Bayes factor between SEOBNRv4HM and SEOBNRv4EHM[8] We show the cumulative distribution function (CDF) of the recovered Bayes factors in Fig. 12. By assessing where the measured Bayes factors intersect with the CDF of the population, we can compute how much of an outlier each event is with respect to a quasicircular aligned-spin population. We find GW200129 with `BayesWave A` glitch mitigation has a significance of $3.6 \times 10^{-3}$, GW200208_22 has a significance of $3.6 \times 10^{-3}$, and GW190521 has a significance of $1.3 \times 10^{-1}$. Due to the limited number of injections, we can only claim that GW200129 with `gwsubtract` glitch mitigation and GW190701 lie beyond the $1.8 \times 10^{-3}$ level.

We also attempted to inject a quasicircular precessing-spin population and recover the distribution of $\mathcal{B}_{\rm EAS/QCAS}$. This test would measure how much of an outlier the $\mathcal{B}_{\rm EAS/QCAS}$ of individual events are under the assumption that all events are actually spin precessing. However, because the SEOBNRv4EHM Dingo network is not trained on SEOBNRv4PHM waveforms, we fail to get $n_{\rm eff} > 5000$ for a subset (40%) of injections. As this may cause an incorrect

[8]We could also obtain the Bayes factors by analyzing the injections with SEOBNRv4HM; however, since we are only interested in the Bayes factor and not the posteriors for this test, the Savage-Dickey ratio gives us a cheap alternative. This is possible because SEOBNRv4HM is equivalent to SEOBNRv4EHM in the $e \to 0$ limit.

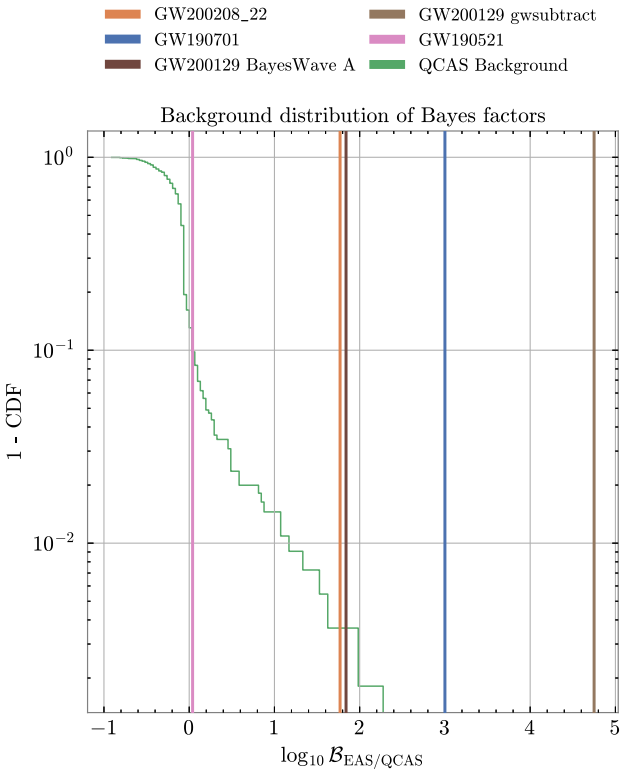


FIG. 12. Significance levels of GW200129, GW190701, and GW200208_22 based on a quasicircular aligned-spin background distribution. In green, we show 1 minus the CDF of 550 draws from the population distribution in Ref. [13]. By finding where the Bayes factors of the individual events intersect with the green line, we can compute the significance of each event.

estimate of the CDF of the background distribution, we leave this for future work.

## APPENDIX D: GAUSSIAN NOISE SYNTHETIC INJECTION

To verify the accuracy of Dingo in the presence of Gaussian noise, we perform a Gaussian noise injection using SEOBNRv4EHM. The cornerplot comparing Dingo-IS to pBilby is shown in Fig. 13. When comparing the pBilby posterior to the Dingo-IS posterior, we see all JSDs are less than $2 \times 10^{-3}$ bits. It may seem strange that the injected value of the chirp mass is at the 90% credible level for both pBilby and Dingo-IS. However, note that this is not unexpected as 10% of injections in Gaussian noise should fall outside the 90% interval of the marginal distribution.

## APPENDIX E: KICK VELOCITY OF GW200129

As discussed in the main text, when analyzing GW200129 with SEOBNRv4EHM we find a low kick velocity. We compute the kick velocity for SEOBNRv4EHM by integrating the momentum radiated throughout the orbit, $\boldsymbol{P}^{\mathrm{rad}}$, using the waveform modes $h_{lm}$ [269]. We then

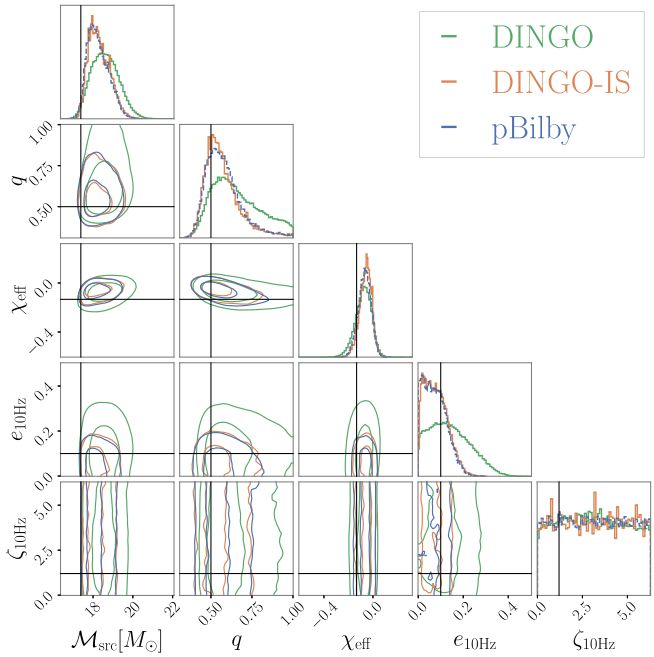


FIG. 13. Posterior distributions for a Gaussian noise injection with SEOBNRv4EHM with parameters $\chi_{\mathrm{eff}} = -0.13$, $\mathcal{M}_{\mathrm{src}} = 17.2M_\odot$, $q = 0.5$, $e_{10\ \mathrm{Hz}} = 0.1$, and $\zeta_{10\ \mathrm{Hz}} = 1.2$. The sample efficiency importance sampling on this event is 7%.

determine the remnant mass, $m_f$, using a fit to numerical relativity as described in Ref. [132]. Then the remnant kick velocity is simply $v_f = \boldsymbol{P}^{\mathrm{rad}}/m_f$. For NRSur7dq4, we can simply use the NRSur7dq4Remnant model from Ref. [132] with the surfinBH package to find $v_f$.

However, obtaining a low kick velocity when analyzing GW200129 with SEOBNRv4EHM does *not* prove that this event has a negligible kick. The large kicks in BBHs come from asymmetric momentum emission. The highest momentum asymmetry occurs with misaligned spins [270,271]. Thus, with an aligned-spin model like SEOBNRv4EHM or SEOBNRv4HM the recoil velocity has to be small *by construction*.[9] But if one were to include both eccentricity and spin-precession, we may find that GW200129 still has a measurable kick velocity. See Fig. 14 for the kick velocity distribution of GW200129.

## APPENDIX F: THE EFFECT OF THE OCCAM PENALTY

An eccentric aligned-spin model contains fewer degrees of freedom than a quasicircular spin-precessing model. Therefore, the Bayes factors will slightly favor the eccentric aligned-spin hypothesis, even if the true parameters of the event are quasicircular and aligned spin.[10] This is known as

[9]It has also been that in low eccentricity NR simulations, kicks are only ∼25% larger than the quasicircular case [272].

[10]We note the Occam penalty should also cause $\log_{10} \mathcal{B}_{\mathrm{EAS/QCAS}}$ to favor the quasicircular aligned-spin model by the same argument.

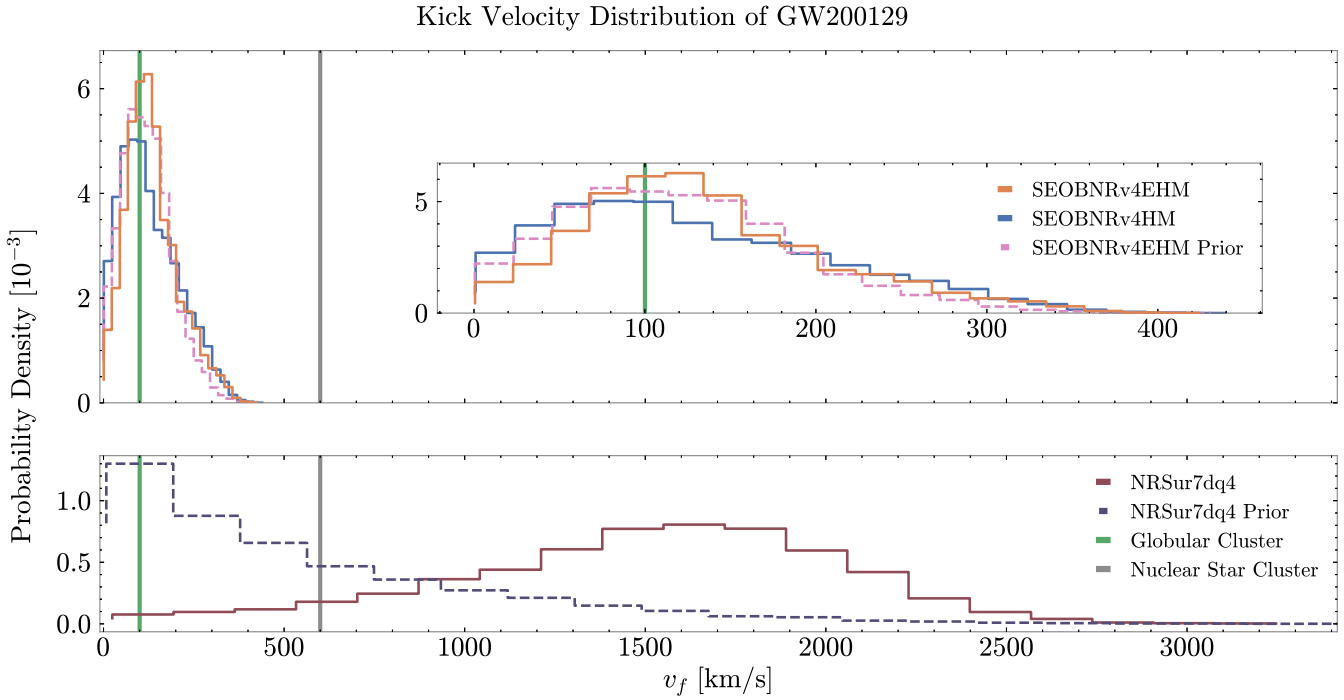


FIG. 14. Kick velocity of GW200129 in km/s. Shown on the top (bottom) figure is the posterior distribution of the kick velocity using samples from the SEOBNRv4EHM and SEOBNRv4HM (NRSur7dq4) analyses using `gwsubtract` glitch mitigation. The green (gray) vertical lines show the typical escape velocity of a globular (nuclear) cluster as shown in Ref. [215].

the Occam penalty, and it is a feature of Bayesian model comparison. We stress that one should not try to cancel out the Occam penalty; it quantifies the fact that if the data are uninformative, the model with fewer degrees of freedom should be preferred (this is also sometimes called Occam's razor).

Nonetheless, we can compute the expected $\mathcal{B}_{\mathrm{EAS/QCP}}$ had the true event parameters been quasicircular aligned-spin. If these are similar to the $\mathcal{B}_{\mathrm{EAS/QCP}}$ reported in Table I, we know that the $\mathcal{B}_{\mathrm{EAS/QCP}}$ are driven by the fact that the eccentric aligned-spin model has fewer degrees of freedom and rather than information from the data.

We perform three zero-noise injections using the maximum likelihood parameters of GW200129, GW190701, and GW200208_22 analyzed with SEOBNRv4EHM but setting the eccentricity to zero. We then compute $\log_{10}\mathcal{B}_{\mathrm{EAS/QCP}}$ for these injections. We find that $\log_{10}\mathcal{B}_{\mathrm{EAS/QCP}} = 0.1$, 0.06, and 0.07 for GW200129, GW190701, and GW200208_22, respectively. In all cases, we see that there is a minor preference for the eccentric aligned-spin hypothesis. We note that this mild preference for the eccentric aligned-spin hypothesis is orders of magnitude smaller than the Bayes factors reported in Table I and Fig. 12. This indicates that the prior volume difference alone cannot account for the observed Bayes factors.

## APPENDIX G: PRECESSING INJECTIONS WITH ECCENTRIC RECOVERY AND VICE VERSA

Due to the possibility that eccentricity could be confused for spin precession in short signals [126,127], we perform an injection recovery campaign using SEOBNRv4EHM and NRSur7dq4. In this case, we are most interested in GW200129. Therefore, we first analyze GW200129 with `gwsubtract` using both SEOBNRv4EHM and NRSur7dq4. We then find the maximum likelihood point from each analysis. Finally, we inject a precessing NRSur7dq4 waveform with the maximum likelihood parameters and recover it with SEOBNRv4EHM (and vice versa). The results of this analysis are shown in Fig. 15. With the parameters considered here, we do not find evidence that spin precession can be mistaken for eccentricity (or vice versa).

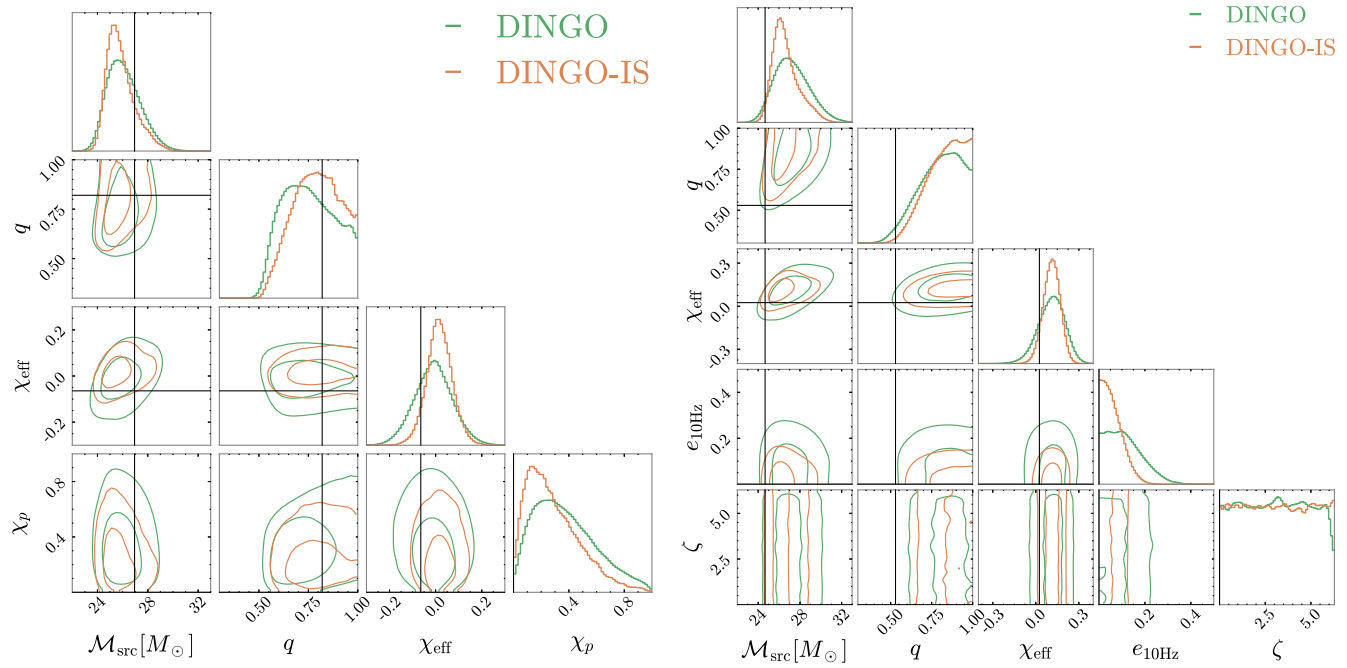


FIG. 15. Posterior distributions obtained with NRSur7dq4 (left) and SEOBNRv4EHM (right) when injecting SEOBNRv4EHM (left) or NRSur7dq4 (right). The injection parameters were chosen to be the maximum likelihood point of GW200129 with `gwsubtract` glitch mitigation analyzed with SEOBNRv4EHM (left) and NRSur7dq4 (right).

## APPENDIX H: TABLE III, GW EVENTS ANALYZED

Table of Bayes factors, $p_{\rm ecc}$ and FARs for the events analyzed in this paper.

TABLE III. The set of all BBHs analyzed. When available, we report the results using higher modes. However, for a few of the events, we do not achieve greater than 5000 effective samples using higher modes and therefore we report these results using only the 22 mode. We report the minimum FAR for each event following Ref. [13].

| Event name | $\mathrm{FAR}_{\rm min}$ ($\mathrm{yr}^{-1}$) | $p_{\rm ecc}$ | $\log_{10}\mathcal{B}^{22}_{\rm EAS/QCAS}$ | $\log_{10}\mathcal{B}^{\rm HM}_{\rm EAS/QCAS}$ | $e_{10\ \rm Hz}$ | $n_{\rm eff}$ | $n_{\rm eff}/N\times 100$ |
|---|---|---|---|---|---|---|---|
| GW150914 | $<1.00\times10^{-5}$ | 0.02 | ⋯ | −0.44 | $0.07^{+0.11}_{-0.07}$ | 21668 | 4.3% |
| GW170104 | $<1.00\times10^{-5}$ | <0.01 | −0.31 | −0.78 | $0.17^{+0.22}_{-0.17}$ | 8868 | 1.8% |
| GW170729 | $1.80\times10^{-1}$ | 0.01 | −0.18 | −0.65 | $0.19^{+0.23}_{-0.19}$ | 22520 | 4.6% |
| GW170809 | $<1.00\times10^{-5}$ | 0.01 | −0.30 | −0.73 | $0.17^{+0.22}_{-0.17}$ | 17561 | 3.6% |
| GW170814 | $<1.00\times10^{-5}$ | 0.10 | −0.27 | 0.66 | $0.09^{+0.13}_{-0.09}$ | 5280 | 0.6% |
| GW170818 | $<1.00\times10^{-5}$ | 0.01 | −0.30 | −0.68 | $0.17^{+0.23}_{-0.17}$ | 39222 | 8.1% |
| GW170823 | $<1.00\times10^{-5}$ | 0.01 | −0.18 | −0.61 | $0.19^{+0.23}_{-0.19}$ | 27691 | 5.7% |
| GW190408_181802 | $<1.00\times10^{-5}$ | 0.02 | −0.45 | −0.48 | $0.16^{+0.15}_{-0.16}$ | 14498 | 3.3% |
| GW190413_052954 | $8.20\times10^{-1}$ | 0.09 | −0.10 | 0.25 | $0.20^{+0.19}_{-0.20}$ | 31394 | 1.0% |
| GW190413_134308 | $1.81\times10^{-1}$ | 0.10 | −0.08 | 0.32 | $0.23^{+0.22}_{-0.23}$ | 138986 | 2.8% |
| GW190421_213856 | $2.83\times10^{-3}$ | 0.03 | −0.27 | −0.25 | $0.15^{+0.22}_{-0.15}$ | 76219 | 15.6% |
| GW190503_185404 | $<1.00\times10^{-5}$ | 0.06 | ⋯ | 0.04 | $0.23^{+0.17}_{-0.23}$ | 6037 | 2.1% |
| GW190512_180714 | $<1.00\times10^{-5}$ | 0.02 | −0.37 | −0.40 | $0.11^{+0.17}_{-0.11}$ | 69513 | 14.2% |
| GW190513_205428 | $<1.00\times10^{-5}$ | 0.11 | 0.30 | 0.36 | $0.26^{+0.14}_{-0.24}$ | 6546 | 0.3% |
| GW190514_065416 | $2.80\times10^{0}$ | 0.10 | −0.01 | 0.32 | $0.23^{+0.21}_{-0.23}$ | 295948 | 6.3% |
| GW190517_055101 | $3.47\times10^{-4}$ | 0.02 | −0.29 | −0.21 | $0.19^{+0.20}_{-0.19}$ | 13103 | 2.7% |
| GW190519_153544 | $<1.00\times10^{-5}$ | 0.02 | −0.43 | −0.41 | $0.15^{+0.25}_{-0.15}$ | 44089 | 9.4% |

*(Table continued)*

TABLE III. *(Continued)*

| Event name | $\mathrm{FAR}_{\mathrm{min}}$ ($\mathrm{yr}^{-1}$) | $p_{\mathrm{ecc}}$ | $\log_{10}\mathcal{B}^{22}_{\mathrm{EAS/QCAS}}$ | $\log_{10}\mathcal{B}^{\mathrm{HM}}_{\mathrm{EAS/QCAS}}$ | $e_{10\ \mathrm{Hz}}$ | $n_{\mathrm{eff}}$ | $n_{\mathrm{eff}}/N \times 100$ |
|---|---|---|---|---|---|---|---|
| GW190521 | $<1.00 \times 10^{-5}$ | 0.04 | ⋯ | −0.04 | $0.15^{+0.15}_{-0.13}$ | 261513 | 26.7% |
| GW190521_074359 | $1.00 \times 10^{-2}$ | 0.04 | −0.00 | −0.13 | $0.15^{+0.08}_{-0.14}$ | 148692 | 30.4% |
| GW190527_092055 | $2.28 \times 10^{-1}$ | 0.05 | 0.08 | 0.01 | $0.33^{+0.17}_{-0.29}$ | 29131 | 6.2% |
| GW190602_175927 | $<1.00 \times 10^{-5}$ | 0.04 | −0.19 | −0.15 | $0.19^{+0.21}_{-0.19}$ | 75130 | 15.7% |
| GW190620_030421 | $1.12 \times 10^{-2}$ | 0.15 | ⋯ | 0.56 | $0.32^{+0.18}_{-0.21}$ | 32211 | 6.6% |
| GW190630_185205 | $<1.00 \times 10^{-5}$ | 0.02 | ⋯ | −0.45 | $0.09^{+0.12}_{-0.09}$ | 5580 | 1.1% |
| GW190701_203306 | $5.71 \times 10^{-3}$ | 0.98 | 2.72 | 3.00 | $0.46^{+0.04}_{-0.04}$ | 19337 | 1.0% |
| GW190706_222641 | $<1.00 \times 10^{-5}$ | ⋯ | 0.37 | ⋯ | $0.46^{+0.04}_{-0.41}$ | 14690 | 1.5% |
| GW190719_215514 | $6.30 \times 10^{-1}$ | 0.11 | −0.18 | 0.37 | $0.18^{+0.23}_{-0.18}$ | 15033 | 0.8% |
| GW190727_060333 | $<1.00 \times 10^{-5}$ | 0.10 | −0.33 | 0.31 | $0.12^{+0.19}_{-0.12}$ | 5833 | 1.2% |
| GW190731_140936 | $3.30 \times 10^{-1}$ | 0.09 | −0.20 | 0.26 | $0.17^{+0.23}_{-0.17}$ | 10976 | 2.2% |
| GW190803_022701 | $7.32 \times 10^{-2}$ | 0.09 | −0.21 | 0.27 | $0.17^{+0.22}_{-0.17}$ | 5154 | 1.1% |
| GW190828_063405 | $<1.00 \times 10^{-5}$ | 0.10 | 0.28 | 0.31 | $0.25^{+0.13}_{-0.22}$ | 68326 | 14.0% |
| GW190828_065509 | $<1.00 \times 10^{-5}$ | ⋯ | 0.31 | ⋯ | $0.31^{+0.18}_{-0.24}$ | 8007 | 0.2% |
| GW190910_112807 | $2.87 \times 10^{-3}$ | 0.0 | ⋯ | 0.08 | $0.16^{+0.14}_{-0.16}$ | 14053 | 4.7% |
| GW190915_235702 | $<1.00 \times 10^{-5}$ | 0.02 | −0.45 | −0.55 | $0.23^{+0.14}_{-0.22}$ | 40476 | 9.0% |
| GW190916_200658 | $4.70 \times 10^{0}$ | 0.10 | −0.18 | 0.33 | $0.17^{+0.22}_{-0.17}$ | 5965 | 1.2% |
| GW190926_050336 | $1.10 \times 10^{0}$ | 0.09 | −0.03 | 0.25 | $0.23^{+0.21}_{-0.23}$ | 5257 | 1.1% |
| GW190929_012149 | $<1.00 \times 10^{-5}$ | 0.04 | −0.34 | −0.09 | $0.20^{+0.22}_{-0.20}$ | 157953 | 3.6% |
| GW191109_010717 | $1.80 \times 10^{-4}$ | 0.06 | 0.33 | 0.15 | $0.26^{+0.24}_{-0.22}$ | 15211 | 7.9% |
| GW191127_050227 | $2.49 \times 10^{-1}$ | ⋯ | 0.06 | ⋯ | $0.30^{+0.20}_{-0.27}$ | 7193 | 0.7% |
| GW191204_110529 | $<1.00 \times 10^{-5}$ | 0.03 | −0.29 | −0.34 | $0.12^{+0.21}_{-0.12}$ | 21785 | 4.5% |
| GW191215_223052 | $<1.00 \times 10^{-5}$ | ⋯ | 0.12 | ⋯ | $0.28^{+0.17}_{-0.27}$ | 9083 | 0.9% |
| GW191222_033537 | $<1.00 \times 10^{-5}$ | ⋯ | −0.30 | ⋯ | $0.13^{+0.20}_{-0.13}$ | 1720155 | 35.1% |
| GW191230_180458 | $5.02 \times 10^{-2}$ | 0.10 | −0.21 | 0.32 | $0.16^{+0.23}_{-0.16}$ | 8923 | 0.3% |
| GW200112_155838 | $2.04 \times 10^{-1}$ | 0.02 | ⋯ | −0.51 | $0.08^{+0.13}_{-0.08}$ | 38358 | 7.7% |
| GW200128_022011 | $4.29 \times 10^{-3}$ | 0.10 | −0.21 | 0.32 | $0.16^{+0.18}_{-0.16}$ | 7198 | 1.5% |
| GW200129_065458 | $<1.00 \times 10^{-5}$ | $1 - 5 \times 10^{-3}$ | 4.57 | 4.75 | $0.34^{+0.11}_{-0.06}$ | 6204 | 0.1% |
| GW200208_130117 | $3.11 \times 10^{-4}$ | 0.03 | −0.25 | −0.22 | $0.15^{+0.21}_{-0.15}$ | 7732 | 1.6% |
| GW200208_222617 | $4.80 \times 10^{0}$ | 0.73 | 1.25 | 1.77 | $0.4^{+0.08}_{-0.15}$ | 31246 | 0.5% |
| GW200209_085452 | $4.60 \times 10^{-2}$ | 0.13 | 0.07 | 0.42 | $0.25^{+0.23}_{-0.23}$ | 45766 | 0.9% |
| GW200216_220804 | $3.50 \times 10^{-1}$ | 0.12 | 0.00 | 0.41 | $0.26^{+0.19}_{-0.26}$ | 1538557 | 15.4% |
| GW200219_094415 | $9.94 \times 10^{-4}$ | 0.05 | −0.36 | −0.03 | $0.14^{+0.22}_{-0.14}$ | 6297 | 0.6% |
| GW200220_124850 | $3.00 \times 10^{1}$ | 0.09 | −0.07 | 0.27 | $0.21^{+0.24}_{-0.21}$ | 7529 | 0.8% |
| GW200224_222234 | $<1.00 \times 10^{-5}$ | 0.03 | −0.27 | −0.29 | $0.13^{+0.14}_{-0.13}$ | 135039 | 27.6% |
| GW200225_060421 | $<1.00 \times 10^{-5}$ | <0.00 | −1.19 | −1.18 | $0.18^{+0.20}_{-0.18}$ | 5797 | 0.2% |
| GW200302_015811 | $1.12 \times 10^{-1}$ | 0.07 | ⋯ | 0.24 | $0.15^{+0.21}_{-0.15}$ | 20635 | 4.1% |
| GW200306_093714 | $2.40 \times 10^{1}$ | 0.04 | −0.12 | −0.12 | $0.17^{+0.22}_{-0.17}$ | 37297 | 7.8% |
| GW200308_173609 | $2.40 \times 10^{0}$ | 0.03 | −0.27 | 0.07 | $0.14^{+0.25}_{-0.14}$ | 126454 | 3.3% |
| GW200311_115853 | $<1.00 \times 10^{-5}$ | 0.02 | −0.50 | −0.50 | $0.09^{+0.15}_{-0.09}$ | 160548 | 32.9% |

[1] B. P. Abbott *et al.* (LIGO Scientific and Virgo Collaborations), GWTC-1: A gravitational-wave transient catalog of compact binary mergers observed by LIGO and Virgo during the first and second observing runs, Phys. Rev. X **9**, 031040 (2019).

[2] R. Abbott *et al.* (LIGO Scientific and Virgo Collaborations), GWTC-2: Compact binary coalescences observed by LIGO and Virgo during the first half of the third observing run, Phys. Rev. X **11**, 021053 (2021).

[3] B. P. Abbott *et al.* (LIGO Scientific and Virgo Collaborations), Observation of gravitational waves from a binary black hole merger, Phys. Rev. Lett. **116**, 061102 (2016).

[4] R. Abbott *et al.* (LIGO Scientific and Virgo Collaborations), GWTC-2.1: Deep extended catalog of compact binary coalescences observed by LIGO and Virgo during the first half of the third observing run, Phys. Rev. D **109**, 022001 (2024).

[5] A. H. Nitz, C. D. Capano, S. Kumar, Y.-F. Wang, S. Kastha, M. Schäfer, R. Dhurkunde, and M. Cabero, 3-OGC: Catalog of gravitational waves from compact-binary mergers, Astrophys. J. **922**, 76 (2021).

[6] S. Olsen, T. Venumadhav, J. Mushkin, J. Roulet, B. Zackay, and M. Zaldarriaga, New binary black hole mergers in the LIGO-Virgo O3a data, Phys. Rev. D **106**, 043009 (2022).

[7] T. Akutsu *et al.* (KAGRA Collaboration), KAGRA: 2.5 Generation interferometric gravitational wave detector, Nat. Astron. **3**, 35 (2019).

[8] T. Akutsu *et al.* (KAGRA Collaboration), Overview of KAGRA: Detector design and construction history, Prog. Theor. Exp. Phys. **2021**, 05A101 (2021).

[9] T. Islam, A. Vajpeyi, F. H. Shaik, C.-J. Haster, V. Varma, S. E. Field, J. Lange, R. O'Shaughnessy, and R. Smith, Analysis of GWTC-3 with fully precessing numerical relativity surrogate models, Phys. Rev. D **112**, 044001 (2025).

[10] A. H. Nitz, S. Kumar, Y.-F. Wang, S. Kastha, S. Wu, M. Schäfer, R. Dhurkunde, and C. D. Capano, 4-ogc: Catalog of gravitational waves from compact binary mergers, Astrophys. J. **946**, 59 (2023).

[11] J. Aasi *et al.* (LIGO Scientific Collaboration), Advanced LIGO, Classical Quantum Gravity **32**, 074001 (2015).

[12] F. Acernese *et al.* (Virgo Collaboration), Advanced Virgo: A second-generation interferometric gravitational wave detector, Classical Quantum Gravity **32**, 024001 (2015).

[13] R. Abbott *et al.* (LIGO Scientific, Virgo, and KAGRA Collaborations), The population of merging compact binaries inferred using gravitational waves through GWTC-3, Phys. Rev. X **13**, 011048 (2023).

[14] S. Galaudage, C. Talbot, T. Nagar, D. Jain, E. Thrane, and I. Mandel, Building better spin models for merging binary black holes: evidence for nonspinning and rapidly spinning nearly aligned subpopulations, Astrophys. J. Lett. **921**, L15 (2021).

[15] H. Tong, S. Galaudage, and E. Thrane, Population properties of spinning black holes using the gravitational-wave transient catalog 3, Phys. Rev. D **106**, 103019 (2022).

[16] W. M. Farr, S. Stevenson, M. Coleman Miller, I. Mandel, B. Farr, and A. Vecchio, Distinguishing spin-aligned and isotropic black hole populations with gravitational waves, Nature (London) **548**, 426 (2017).

[17] V. Tiwari, S. Fairhurst, and M. Hannam, Constraining black-hole spins with gravitational wave observations, Astrophys. J. **868**, 140 (2018).

[18] K. Belczynski, D. E. Holz, T. Bulik, and R. O'Shaughnessy, The first gravitational-wave source from the isolated evolution of two stars in the 40–100 solar mass range, Nature (London) **534**, 512 (2016).

[19] C. Hoy, S. Fairhurst, M. Hannam, and V. Tiwari, Understanding how fast black holes spin by analyzing data from the second gravitational-wave catalogue, Astrophys. J. **928**, 75 (2022).

[20] I. M. Romero-Shaw, P. D. Lasky, and E. Thrane, Four eccentric mergers increase the evidence that LIGO–Virgo–KAGRA's binary black holes form dynamically, Astrophys. J. **940**, 171 (2022).

[21] I. M. Romero-Shaw, P. D. Lasky, E. Thrane, and J. C. Bustillo, GW190521: Orbital eccentricity and signatures of dynamical formation in a binary black hole merger signal, Astrophys. J. Lett. **903**, L5 (2020).

[22] I. M. Romero-Shaw, P. D. Lasky, and E. Thrane, Searching for eccentricity: Signatures of dynamical formation in the first gravitational-wave transient catalogue of LIGO and Virgo, Mon. Not. R. Astron. Soc. **490**, 5210 (2019).

[23] H. L. Iglesias *et al.*, Eccentricity estimation for five binary black hole mergers with higher-order gravitational wave modes, Astrophys. J. **972**, 65 (2024).

[24] A. Ramos-Buades, A. Buonanno, and J. Gair, Bayesian inference of binary black holes with inspiral-merger-ringdown waveforms using two eccentric parameters, Phys. Rev. D **108**, 124063 (2023).

[25] E. Maggio, H. O. Silva, A. Buonanno, and A. Ghosh, Tests of general relativity in the nonlinear regime: A parametrized plunge-merger-ringdown gravitational waveform model, Phys. Rev. D **108**, 024043 (2022).

[26] A. K. Mehta, A. Buonanno, R. Cotesta, A. Ghosh, N. Sennett, and J. Steinhoff, Tests of general relativity with gravitational-wave observations using a flexible theory-independent method, Phys. Rev. D **107**, 044020 (2023).

[27] R. Abbott *et al.* (LIGO Scientific and Virgo Collaborations), Tests of general relativity with binary black holes from the second LIGO-Virgo gravitational-wave transient catalog, Phys. Rev. D **103**, 122002 (2021).

[28] B. P. Abbott *et al.* (LIGO Scientific and Virgo Collaborations), Tests of general relativity with GW150914, Phys. Rev. Lett. **116**, 221101 (2016); **121**, 129902(E) (2018).

[29] N. Cornish, L. Sampson, N. Yunes, and F. Pretorius, Gravitational wave tests of general relativity with the parameterized post-Einsteinian framework, Phys. Rev. D **84**, 062003 (2011).

[30] M. Isi, K. Chatziioannou, and W. M. Farr, Hierarchical test of general relativity with gravitational waves, Phys. Rev. Lett. **123**, 121101 (2019).

[31] M. Zevin, I. M. Romero-Shaw, K. Kremer, E. Thrane, and P. D. Lasky, Implications of eccentric observations on

binary black hole formation channels, Astrophys. J. Lett. **921**, L43 (2021).
[32] K. Belczynski, Z. Doctor, M. Zevin, A. Olejak, S. Banerje, and D. Chattopadhyay, Black Hole–Black Hole Total Merger Mass and the Origin of LIGO/Virgo Sources, Astrophys. J. **935**, 126 (2022).
[33] E. D. Kovetz, I. Cholis, P. C. Breysse, and M. Kamionkowski, Black hole mass function from gravitational wave measurements, Phys. Rev. D **95**, 103010 (2017).
[34] G. Fragione, I. Ginsburg, and B. Kocsis, Gravitational waves and Intermediate-mass black hole retention in globular clusters, Astrophys. J. **856**, 92 (2018).
[35] S. Banerjee, Stellar-mass black holes in young massive and open stellar clusters and their role in gravitational-wave generation—II, Mon. Not. R. Astron. Soc. **473**, 909 (2018).
[36] C. Kimball *et al.*, Evidence for hierarchical black hole mergers in the second LIGO–Virgo gravitational wave catalog, Astrophys. J. Lett. **915**, L35 (2021).
[37] C. D. Bailyn, R. K. Jain, P. Coppi, and J. A. Orosz, The mass distribution of stellar black holes, Astrophys. J. **499**, 367 (1998).
[38] C. L. Fryer, Mass limits for black hole formation, Astrophys. J. **522**, 413 (1999).
[39] H. A. Bethe and G. E. Brown, Evolution of binary compact objects which merge, Astrophys. J. **506**, 780 (1998).
[40] B. Carr, F. Kuhnel, and M. Sandstad, Primordial black holes as dark matter, Phys. Rev. D **94**, 083504 (2016).
[41] P. C. Peters, Gravitational radiation and the motion of two point masses, Phys. Rev. **136**, B1224 (1964).
[42] I. Mandel and A. Farmer, Merging stellar-mass binary black holes, Phys. Rep. **955**, 1 (2022).
[43] K. Belczynski, V. Kalogera, and T. Bulik, A comprehensive study of binary compact objects as gravitational wave sources: Evolutionary channels, rates, and physical properties, Astrophys. J. **572**, 407 (2001).
[44] K. Belczynski, T. Ryu, R. Perna, E. Berti, T. L. Tanaka, and T. Bulik, On the likelihood of detecting gravitational waves from population III compact object binaries, Mon. Not. R. Astron. Soc. **471**, 4702 (2017).
[45] K. Belczynski *et al.*, The effect of pair-instability mass loss on black hole mergers, Astron. Astrophys. **594**, A97 (2016).
[46] M. Dominik, K. Belczynski, C. Fryer, D. Holz, E. Berti, T. Bulik, I. Mandel, and R. O'Shaughnessy, Double compact objects I: The significance of the common envelope on merger rates, Astrophys. J. **759**, 52 (2012).
[47] N. Mennekens and D. Vanbeveren, Massive double compact object mergers: Gravitational wave sources and r-process-element production sites, Astron. Astrophys. **564**, A134 (2014).
[48] J. W. Barrett, S. M. Gaebel, C. J. Neijssel, A. Vigna-Gómez, S. Stevenson, C. P. L. Berry, W. M. Farr, and I. Mandel, Accuracy of inference on the physics of binary evolution from gravitational-wave observations, Mon. Not. R. Astron. Soc. **477**, 4685 (2018).
[49] N. Giacobbo and M. Mapelli, The progenitors of compact-object binaries: Impact of metallicity, common envelope and natal kicks, Mon. Not. R. Astron. Soc. **480**, 2011 (2018).
[50] I. Mandel and S. E. de Mink, Merging binary black holes formed through chemically homogeneous evolution in short-period stellar binaries, Mon. Not. R. Astron. Soc. **458**, 2634 (2016).
[51] S. E. de Mink and I. Mandel, The chemically homogeneous evolutionary channel for binary black hole mergers: Rates and properties of gravitational-wave events detectable by Advanced LIGO, Mon. Not. R. Astron. Soc. **460**, 3545 (2016).
[52] K. Belczynski, T. Bulik, and B. Rudak, First stellar binary black holes: Strongest gravitational wave burst sources, Astrophys. J. Lett. **608**, L45 (2004).
[53] F. Antonini, S. Toonen, and A. S. Hamers, Binary black hole mergers from field triples: Properties, rates and the impact of stellar evolution, Astrophys. J. **841**, 77 (2017).
[54] G. Fragione and J. Silk, Repeated mergers and ejection of black holes within nuclear star clusters, Mon. Not. R. Astron. Soc. **498**, 4591 (2020).
[55] K. Silsbee and S. Tremaine, Lidov-Kozai cycles with gravitational radiation: Merging black holes in isolated triple systems, Astrophys. J. **836**, 39 (2017).
[56] M. Arca-Sedda, G. Li, and B. Kocsis, Order in the chaos—Eccentric black hole binary mergers in triples formed via strong binary–binary scatterings, Astron. Astrophys. **650**, A189 (2021).
[57] A. Vigna-Gómez, S. Toonen, E. Ramirez-Ruiz, N. W. C. Leigh, J. Riley, and C.-J. Haster, Massive stellar triples leading to sequential binary black-hole mergers in the field, Astrophys. J. Lett. **907**, L19 (2021).
[58] H. von Zeipel, Sur l'application des séries de M. Lindstedt à l'étude du mouvement des comètes périodiques, Astron. Nachr. **183**, 345 (1910).
[59] Y. Kozai, Secular perturbations of asteroids with high inclination and eccentricity, Astron. J. **67**, 591 (1962).
[60] M. L. Lidov, The evolution of orbits of artificial satellites of planets under the action of gravitational perturbations of external bodies, Planet. Space Sci. **9**, 719 (1962).
[61] G. E. Giacaglia, Notes on von Zeipel's method, Publications **1**, 196 (1964).
[62] T. O. Kimpson, M. Spera, M. Mapelli, and B. M. Ziosi, Hierarchical black hole triples in young star clusters: Impact of Kozai–Lidov resonance on mergers, Mon. Not. R. Astron. Soc. **463**, 2443 (2016).
[63] L. Wen, On the eccentricity distribution of coalescing black hole binaries driven by the kozai mechanism in globular clusters, Astrophys. J. **598**, 419 (2003).
[64] M. Zevin, J. Samsing, C. Rodriguez, C.-J. Haster, and E. Ramirez-Ruiz, Eccentric black hole mergers in dense star clusters: The role of binary–binary encounters, Astrophys. J. **871**, 91 (2019).
[65] J. Samsing and E. Ramirez-Ruiz, On the assembly rate of highly eccentric binary black hole mergers, Astrophys. J. Lett. **840**, L14 (2017).
[66] J. Samsing, M. MacLeod, and E. Ramirez-Ruiz, The formation of eccentric compact binary inspirals and the role of gravitational wave emission in binary-single stellar encounters, Astrophys. J. **784**, 71 (2014).

[67] M. C. Miller and D. P. Hamilton, Production of intermediate-mass black holes in globular clusters, Mon. Not. R. Astron. Soc. **330**, 232 (2002).
[68] D. C. Heggie, Binary evolution in stellar dynamics, Mon. Not. R. Astron. Soc. **173**, 729 (1975).
[69] S. Sigurdsson and L. Hernquist, Primordial black holes in globular clusters, Nature (London) **364**, 423 (1993).
[70] S. F. Kulkarni, S. McMillan, and P. Hut, Stellar black holes in globular clusters, Nature (London) **364**, 421 (1993).
[71] S. Sigurdsson and E. S. Phinney, Dynamics and interactions of binaries and neutron stars in globular clusters, Astrophys. J. Suppl. Ser. **99**, 609 (1995).
[72] S. Sigurdsson and E. S. Phinney, Binary–Single star interactions in globular clusters, Astrophys. J. **415**, 631 (1993).
[73] S. F. Portegies Zwart and S. McMillan, Black hole mergers in the universe, Astrophys. J. Lett. **528**, L17 (2000).
[74] K. Gultekin, M. Coleman Miller, and D. P. Hamilton, Three-body dynamics with gravitational wave emission, Astrophys. J. **640**, 156 (2006).
[75] F. Antonini, S. Chatterjee, C. L. Rodriguez, M. Morscher, B. Pattabiraman, V. Kalogera, and F. A. Rasio, Black hole mergers and blue stragglers from hierarchical triples formed in globular clusters, Astrophys. J. **816**, 65 (2016).
[76] R. M. O'Leary, F. A. Rasio, J. M. Fregeau, N. Ivanova, and R. W. O'Shaughnessy, Binary mergers and growth of black holes in dense star clusters, Astrophys. J. **637**, 937 (2006).
[77] L. Gondán, B. Kocsis, P. Raffai, and Z. Frei, Eccentric black hole gravitational-wave capture sources in galactic nuclei: Distribution of binary parameters, Astrophys. J. **860**, 5 (2018).
[78] B.-M. Hoang, S. Naoz, B. Kocsis, F. A. Rasio, and F. Dosopoulou, Black hole mergers in galactic nuclei induced by the eccentric Kozai–Lidov effect, Astrophys. J. **856**, 140 (2018).
[79] G. Fragione, N. Leigh, and R. Perna, Black hole and neutron star mergers in galactic nuclei: The role of triples, Mon. Not. R. Astron. Soc. **488**, 2825 (2019).
[80] J. Takátsy, B. Bécsy, and P. Raffai, Eccentricity distributions of eccentric binary black holes in galactic nuclei, Mon. Not. R. Astron. Soc. **486**, 570 (2019).
[81] R. M. O'Leary, B. Kocsis, and A. Loeb, Gravitational waves from scattering of stellar-mass black holes in galactic nuclei, Mon. Not. R. Astron. Soc. **395**, 2127 (2009).
[82] D. Britt, B. Johanson, L. Wood, M. C. Miller, and E. Michaely, Binary black hole mergers from hierarchical triples in open clusters, Mon. Not. R. Astron. Soc. **505**, 3844 (2021).
[83] M. Punturo *et al.*, The Einstein telescope: A third-generation gravitational wave observatory, Classical Quantum Gravity **27**, 194002 (2010).
[84] D. Reitze *et al.*, Cosmic explorer: The U.S. Contribution to gravitational-wave astronomy beyond LIGO, Bull. Am. Astron. Soc. **51**, 035 (2019).
[85] P. Amaro-Seoane *et al.* (LISA Collaboration), Laser interferometer space antenna, arXiv:1702.00786.
[86] A. Vijaykumar, A. G. Hanselman, and M. Zevin, Consistent eccentricities for gravitational wave astronomy: Resolving discrepancies between astrophysical simulations and waveform models, Astrophys. J. **969**, 132 (2024).
[87] C. L. Rodriguez, P. Amaro-Seoane, S. Chatterjee, K. Kremer, F. A. Rasio, J. Samsing, C. S. Ye, and M. Zevin, Post-Newtonian dynamics in dense star clusters: Formation, masses, and merger rates of highly-eccentric black hole binaries, Phys. Rev. D **98**, 123005 (2018).
[88] C. L. Rodriguez, P. Amaro-Seoane, S. Chatterjee, and F. A. Rasio, Post-Newtonian dynamics in dense star clusters: Highly-eccentric, highly-spinning, and repeated binary black hole mergers, Phys. Rev. Lett. **120**, 151101 (2018).
[89] H. Tagawa, B. Kocsis, Z. Haiman, I. Bartos, K. Omukai, and J. Samsing, Eccentric black hole mergers in active galactic nuclei, Astrophys. J. Lett. **907**, L20 (2021).
[90] J. Samsing, I. Bartos, D. J. D'Orazio, Z. Haiman, B. Kocsis, N. W. C. Leigh, B. Liu, M. E. Pessah, and H. Tagawa, AGN as potential factories for eccentric black hole mergers, Nature (London) **603**, 237 (2022).
[91] L. Gondán and B. Kocsis, High eccentricities and high masses characterize gravitational-wave captures in galactic nuclei as seen by Earth-based detectors, Mon. Not. R. Astron. Soc. **506**, 1665 (2021).
[92] H.-S. Cho, Systematic bias due to eccentricity in parameter estimation for merging binary neutron stars, Phys. Rev. D **105**, 124022 (2022).
[93] Divyajyoti, S. Kumar, S. Tibrewal, I. M. Romero-Shaw, and C. K. Mishra, Blind spots and biases: The dangers of ignoring eccentricity in gravitational-wave signals from binary black holes, Phys. Rev. D **109**, 043037 (2024).
[94] A. Bonino, R. Gamba, P. Schmidt, A. Nagar, G. Pratten, M. Breschi, P. Rettegno, and S. Bernuzzi, Inferring eccentricity evolution from observations of coalescing binary black holes, Phys. Rev. D **107**, 064024 (2023).
[95] S. Wu, Z. Cao, and Z.-H. Zhu, Measuring the eccentricity of binary black holes in GWTC-1 by using the inspiral-only waveform, Mon. Not. R. Astron. Soc. **495**, 466 (2020).
[96] M. E. Lower, E. Thrane, P. D. Lasky, and R. Smith, Measuring eccentricity in binary black hole inspirals with gravitational waves, Phys. Rev. D **98**, 083028 (2018).
[97] E. O'Shea and P. Kumar, Correlations in gravitational-wave reconstructions from eccentric binaries: A case study with GW151226 and GW170608, Phys. Rev. D **108**, 104018 (2023).
[98] M. Favata, C. Kim, K. G. Arun, J. Kim, and H. W. Lee, Constraining the orbital eccentricity of inspiralling compact binary systems with Advanced LIGO, Phys. Rev. D **105**, 023003 (2022).
[99] M. Favata, Systematic parameter errors in inspiraling neutron star binaries, Phys. Rev. Lett. **112**, 101101 (2014).
[100] B. Sun, Z. Cao, Y. Wang, and H.-C. Yeh, Parameter estimation of eccentric inspiraling compact binaries using an enhanced post circular model for ground-based detectors, Phys. Rev. D **92**, 044034 (2015).
[101] K. J. Wagner and R. O'Shaughnessy, Parameter estimation for low-mass eccentric black hole binaries, Phys. Rev. D **110**, 124024 (2024).
[102] B. P. Abbott *et al.* (LIGO Scientific and Virgo Collaborations), Effects of waveform model systematics on the

interpretation of GW150914, Classical Quantum Gravity **34**, 104002 (2017).
[103] P. Dutta Roy and P. Saini, Impact of unmodeled eccentricity on the tidal deformability measurement and implications for gravitational wave physics inference, Phys. Rev. D **110**, 024002 (2024).
[104] P. Saini, S. A. Bhat, M. Favata, and K. G. Arun, Eccentricity-induced systematic error on parametrized tests of general relativity: Hierarchical Bayesian inference applied to a binary black hole population, Phys. Rev. D **109**, 084056 (2024).
[105] S. A. Bhat, P. Saini, M. Favata, and K. G. Arun, Systematic bias on the inspiral-merger-ringdown consistency test due to neglect of orbital eccentricity, Phys. Rev. D **107**, 024009 (2023).
[106] S. Ma and N. Yunes, Improved constraints on modified gravity with eccentric gravitational waves, Phys. Rev. D **100**, 124032 (2019).
[107] P. Narayan, N. K. Johnson-McDaniel, and A. Gupta, Effect of ignoring eccentricity in testing general relativity with gravitational waves, Phys. Rev. D **108**, 064003 (2023).
[108] M. A. Shaikh, S. A. Bhat, and S. J. Kapadia, A study of the inspiral-merger-ringdown consistency test with gravitational-wave signals from compact binaries in eccentric orbits, Phys. Rev. D **110**, 024030 (2024).
[109] P. Saini, M. Favata, and K. G. Arun, Systematic bias on parametrized tests of general relativity due to neglect of orbital eccentricity, Phys. Rev. D **106**, 084031 (2022).
[110] V. Gayathri, J. Healy, J. Lange, B. O'Brien, M. Szczepanczyk, I. Bartos, M. Campanelli, S. Klimenko, C. O. Lousto, and R. O'Shaughnessy, Eccentricity estimate for black hole mergers with numerical relativity simulations, Nat. Astron. **6**, 344 (2022).
[111] A. K. Lenon, A. H. Nitz, and D. A. Brown, Measuring the eccentricity of GW170817 and GW190425, Mon. Not. R. Astron. Soc. **497**, 1966 (2020).
[112] A. Ramos-Buades, S. Husa, G. Pratten, H. Estellés, C. García-Quirós, M. Mateu-Lucena, M. Colleoni, and R. Jaume, First survey of spinning eccentric black hole mergers: Numerical relativity simulations, hybrid waveforms, and parameter estimation, Phys. Rev. D **101**, 083015 (2020).
[113] R. Gamba, M. Breschi, G. Carullo, S. Albanesi, P. Rettegno, S. Bernuzzi, and A. Nagar, GW190521 as a dynamical capture of two nonspinning black holes, Nat. Astron. **7**, 11 (2023).
[114] P. McMillin, K. J. Wagner, G. Ficarra, C. O. Lousto, and R. O'Shaughnessy, Parameter estimation for GW200208_22 with targeted eccentric numerical-relativity simulations, arXiv:2507.22862.
[115] G. Morras, G. Pratten, and P. Schmidt, Orbital eccentricity in a neutron star—black hole binary, arXiv:2503.15393.
[116] M. d. L. Planas, A. Ramos-Buades, C. García-Quirós, H. Estellés, S. Husa, and M. Haney, Eccentric or circular? A reanalysis of binary black hole gravitational wave events for orbital eccentricity signatures, arXiv:2504.15833.
[117] T. A. Clarke, I. M. Romero-Shaw, P. D. Lasky, and E. Thrane, Gravitational-wave inference for eccentric binaries: The argument of periapsis, Mon. Not. R. Astron. Soc. **517**, 3778 (2022).
[118] M. Dax, S. R. Green, J. Gair, M. Pürrer, J. Wildberger, J. H. Macke, A. Buonanno, and B. Schölkopf, Neural importance sampling for rapid and reliable gravitational-wave inference, Phys. Rev. Lett. **130**, 171403 (2022).
[119] M. Dax, J. Wildberger, S. Buchholz, S. R. Green, J. H. Macke, and B. Schölkopf, Flow matching for scalable simulation-based inference, arXiv:2305.17161.
[120] A. Bohé *et al.*, Improved effective-one-body model of spinning, nonprecessing binary black holes for the era of gravitational-wave astrophysics with advanced detectors, Phys. Rev. D **95**, 044028 (2017).
[121] R. Cotesta, A. Buonanno, A. Bohé, A. Taracchini, I. Hinder, and S. Ossokine, Enriching the symphony of gravitational waves from binary black holes by tuning higher harmonics, Phys. Rev. D **98**, 084028 (2018).
[122] A. Ramos-Buades, A. Buonanno, M. Khalil, and S. Ossokine, Effective-one-body multipolar waveforms for eccentric binary black holes with nonprecessing spins, Phys. Rev. D **105**, 044035 (2022).
[123] M. Khalil, A. Buonanno, J. Steinhoff, and J. Vines, Radiation-reaction force and multipolar waveforms for eccentric, spin-aligned binaries in the effective-one-body formalism, Phys. Rev. D **104**, 024046 (2021).
[124] B. P. Abbott *et al.* (LIGO Scientific and Virgo Collaborations), Binary black hole population properties inferred from the first and second observing runs of Advanced LIGO and Advanced Virgo, Astrophys. J. Lett. **882**, L24 (2019).
[125] R. Abbott *et al.* (KAGRA, Virgo, and LIGO Scientific Collaborations), GWTC-3: Compact binary coalescences observed by LIGO and Virgo during the second part of the third observing run, Phys. Rev. X **13**, 041039 (2023).
[126] I. M. Romero-Shaw, D. Gerosa, and N. Loutrel, Eccentricity or spin precession? distinguishing subdominant effects in gravitational-wave data, Mon. Not. R. Astron. Soc. **519**, 5352 (2023).
[127] J. Calderón Bustillo, N. Sanchis-Gual, A. Torres-Forné, and J. A. Font, Confusing head-on collisions with precessing intermediate-mass binary black hole mergers, Phys. Rev. Lett. **126**, 201101 (2021).
[128] A. Buonanno, Y. Chen, and T. Damour, Transition from inspiral to plunge in precessing binaries of spinning black holes, Phys. Rev. D **74**, 104005 (2006).
[129] Y. Pan, A. Buonanno, A. Taracchini, L. E. Kidder, A. H. Mroué, H. P. Pfeiffer, M. A. Scheel, and B. Szilágyi, Inspiral-merger-ringdown waveforms of spinning, precessing black-hole binaries in the effective-one-body formalism, Phys. Rev. D **89**, 084006 (2014).
[130] S. Babak, A. Taracchini, and A. Buonanno, Validating the effective-one-body model of spinning, precessing binary black holes against numerical relativity, Phys. Rev. D **95**, 024010 (2017).
[131] S. Ossokine *et al.*, Multipolar effective-one-body waveforms for precessing binary black holes: Construction and validation, Phys. Rev. D **102**, 044055 (2020).
[132] V. Varma, S. E. Field, M. A. Scheel, J. Blackman, D. Gerosa, L. C. Stein, L. E. Kidder, and H. P. Pfeiffer, Surrogate models for precessing binary black hole simulations with unequal masses, Phys. Rev. Res. **1**, 033015 (2019).

[133] X. Liu, Z. Cao, and Z.-H. Zhu, Effective-one-body numerical-relativity waveform model for eccentric spin-precessing binary black hole coalescence, arXiv:2310.04552.
[134] W. M. Farr, J. R. Gair, I. Mandel, and C. Cutler, Counting and confusion: Bayesian rate estimation with multiple populations, Phys. Rev. D **91**, 023005 (2015).
[135] M. A. Shaikh, V. Varma, H. P. Pfeiffer, A. Ramos-Buades, and M. van de Meent, Defining eccentricity for gravitational wave astronomy, Phys. Rev. D **108**, 104007 (2023).
[136] A. Ramos-Buades, M. van de Meent, H. P. Pfeiffer, H. R. Rüter, M. A. Scheel, M. Boyle, and L. E. Kidder, Eccentric binary black holes: Comparing numerical relativity and small mass-ratio perturbation theory, Phys. Rev. D **106**, 124040 (2022).
[137] R. J. E. Smith, G. Ashton, A. Vajpeyi, and C. Talbot, Massively parallel Bayesian inference for transient gravitational-wave astronomy, Mon. Not. R. Astron. Soc. **498**, 4492 (2020).
[138] T. Damour, Coalescence of two spinning black holes: An effective one-body approach, Phys. Rev. D **64**, 124013 (2001).
[139] E. Racine, Analysis of spin precession in binary black hole systems including quadrupole-monopole interaction, Phys. Rev. D **78**, 044021 (2008).
[140] L. Santamaria *et al.*, Matching post-Newtonian and numerical relativity waveforms: Systematic errors and a new phenomenological model for non-precessing black hole binaries, Phys. Rev. D **82**, 064016 (2010).
[141] P. Ajith *et al.*, Inspiral-merger-ringdown waveforms for black-hole binaries with non-precessing spins, Phys. Rev. Lett. **106**, 241101 (2011).
[142] P. Schmidt, F. Ohme, and M. Hannam, Towards models of gravitational waveforms from generic binaries II: Modelling precession effects with a single effective precession parameter, Phys. Rev. D **91**, 024043 (2015).
[143] B. Farr, E. Ochsner, W. M. Farr, and R. O'Shaughnessy, A more effective coordinate system for parameter estimation of precessing compact binaries from gravitational waves, Phys. Rev. D **90**, 024018 (2014).
[144] A. Buonanno, Y.-b. Chen, and M. Vallisneri, Detecting gravitational waves from precessing binaries of spinning compact objects: Adiabatic limit, Phys. Rev. D **67**, 104025 (2003); **74**, 029904(E) (2006).
[145] B. F. Schutz, Networks of gravitational wave detectors and three figures of merit, Classical Quantum Gravity **28**, 125023 (2011).
[146] P. A. R. Ade *et al.* (Planck Collaboration), Planck 2015 results. XIII. Cosmological parameters, Astron. Astrophys. **594**, A13 (2016).
[147] I. Mandel, W. M. Farr, and J. R. Gair, Extracting distribution parameters from multiple uncertain observations with selection biases, Mon. Not. R. Astron. Soc. **486**, 1086 (2019).
[148] Y.-F. Wang and A. H. Nitz, Prospects for detecting gravitational waves from eccentric subsolar mass compact binaries, Astrophys. J. **912**, 53 (2021).
[149] A. H. Nitz, A. Lenon, and D. A. Brown, Search for eccentric binary neutron star mergers in the first and second observing runs of Advanced LIGO, Astrophys. J. **890**, 1 (2019).
[150] B. P. Abbott *et al.* (LIGO Scientific and Virgo Collaborations), Search for eccentric binary black hole mergers with Advanced LIGO and Advanced Virgo during their first and second observing runs, Astrophys. J. **883**, 149 (2019).
[151] A. G. Abac *et al.* (LIGO Scientific, Virgo, and KAGRA Collaborations), Search for eccentric black hole coalescences during the third observing run of LIGO and Virgo, Astrophys. J. **973**, 132 (2024).
[152] A. Nagar, A. Bonino, and P. Rettegno, Effective one-body multipolar waveform model for spin-aligned, quasicircular, eccentric, hyperbolic black hole binaries, Phys. Rev. D **103**, 104021 (2021).
[153] A. Nagar *et al.*, Time-domain effective-one-body gravitational waveforms for coalescing compact binaries with nonprecessing spins, tides and self-spin effects, Phys. Rev. D **98**, 104052 (2018).
[154] S. Albanesi, A. Placidi, A. Nagar, M. Orselli, and S. Bernuzzi, New avenue for accurate analytical waveforms and fluxes for eccentric compact binaries, Phys. Rev. D **105**, L121503 (2022).
[155] M. Dax, S. R. Green, J. Gair, M. Deistler, B. Schölkopf, and J. H. Macke, Group equivariant neural posterior estimation, in *International conference on learning representations* (2022).
[156] M. Dax, S. R. Green, J. Gair, J. H. Macke, A. Buonanno, and B. Schölkopf, Real-time gravitational wave science with neural posterior estimation, Phys. Rev. Lett. **127**, 241103 (2021).
[157] S. R. Green and J. Gair, Complete parameter inference for GW150914 using deep learning, Mach. Learn. Sci. Tech. **2**, 03LT01 (2021).
[158] I. Kobyzev, S. J. D. Prince, and M. A. Brubaker, Normalizing flows: An introduction and review of current methods, IEEE Trans. Pattern Anal. Mach. Intell. **43**, 3964 (2021).
[159] G. Papamakarios, E. Nalisnick, D. J. Rezende, S. Mohamed, and B. Lakshminarayanan, Normalizing flows for probabilistic modeling and inference, arXiv:1912.02762.
[160] K. Augustine, A note on importance sampling using standardized weights, Department of Statistics, 348, 1992.
[161] J. S. Speagle, dynesty: A dynamic nested sampling package for estimating Bayesian posteriors and evidences, Mon. Not. R. Astron. Soc. **493**, 3132 (2020).
[162] S. Brooks, A. Gelman, G. Jones, and X.-L. Meng, *Handbook of Markov Chain Monte Carlo* (CRC Press, Boca Raton, 2011).
[163] J. Veitch *et al.*, Parameter estimation for compact binaries with ground-based gravitational-wave observations using the lalinference software library, Phys. Rev. D **91**, 042003 (2015).
[164] G. Ashton *et al.*, Bilby: A user-friendly Bayesian inference library for gravitational-wave astronomy, Astrophys. J. Suppl. Ser. **241**, 27 (2019).
[165] I. M. Romero-Shaw *et al.*, Bayesian inference for compact binary coalescences with Bilby: Validation and application to the first LIGO–Virgo gravitational-wave transient catalogue, Mon. Not. R. Astron. Soc. **499**, 3295 (2020).

[166] G. Ashton and C. Talbot, Bilby-MCMC: An MCMC sampler for gravitational-wave inference, Mon. Not. R. Astron. Soc. **507**, 2037 (2021).
[167] K. W. K. Wong, M. Isi, and T. D. P. Edwards, Fast gravitational-wave parameter estimation without compromises, Astrophys. J. **958**, 129 (2023).
[168] H. Gabbard, C. Messenger, I. S. Heng, F. Tonolini, and R. Murray-Smith, Bayesian parameter estimation using conditional variational autoencoders for gravitational-wave astronomy, Nat. Phys. **18**, 112 (2022).
[169] G. Casella and E. I. George, Explaining the Gibbs sampler, Am. Stat. **46**, 167 (1992).
[170] E. A. Huerta *et al.*, Eccentric, nonspinning, inspiral, Gaussian-process merger approximant for the detection and characterization of eccentric binary black hole mergers, Phys. Rev. D **97**, 024031 (2018).
[171] I. Hinder, L. E. Kidder, and H. P. Pfeiffer, Eccentric binary black hole inspiral-merger-ringdown gravitational waveform model from numerical relativity and post-Newtonian theory, Phys. Rev. D **98**, 044015 (2018).
[172] Z. Cao and W.-B. Han, Waveform model for an eccentric binary black hole based on the effective-one-body-numerical-relativity formalism, Phys. Rev. D **96**, 044028 (2017).
[173] Y. Setyawati and F. Ohme, Adding eccentricity to quasi-circular binary-black-hole waveform models, Phys. Rev. D **103**, 124011 (2021).
[174] A. Nagar and S. Albanesi, Toward a gravitational self-force-informed effective-one-body waveform model for nonprecessing, eccentric, large-mass-ratio inspirals, Phys. Rev. D **106**, 064049 (2022).
[175] T. Islam, V. Varma, J. Lodman, S. E. Field, G. Khanna, M. A. Scheel, H. P. Pfeiffer, D. Gerosa, and L. E. Kidder, Eccentric binary black hole surrogate models for the gravitational waveform and remnant properties: Comparable mass, nonspinning case, Phys. Rev. D **103**, 064022 (2021).
[176] X. Liu, Z. Cao, and L. Shao, Upgraded waveform model of eccentric binary black hole based on effective-one-body-numerical-relativity for spin-aligned binary black holes, Int. J. Mod. Phys. D **32**, 2350015 (2023).
[177] X. Liu, Z. Cao, and Z.-H. Zhu, Effective-one-body numerical-relativity waveform model for eccentric spin-precessing binary black hole coalescence, Classical Quantum Gravity **41**, 195019 (2024).
[178] D. Chiaramello and A. Nagar, Faithful analytical effective-one-body waveform model for spin-aligned, moderately eccentric, coalescing black hole binaries, Phys. Rev. D **101**, 101501 (2020).
[179] A. Gamboa *et al.*, Accurate waveforms for eccentric, aligned-spin binary black holes: The multipolar effective-one-body model SEOBNRv5EHM, Phys. Rev. D **112**, 044038 (2025).
[180] M. d. L. Planas, A. Ramos-Buades, C. García-Quirós, H. Estellés, S. Husa, and M. Haney, Time-domain phenomenological multipolar waveforms for aligned-spin binary black holes in elliptical orbits, arXiv (2025).
[181] T. Islam, Straightforward mode hierarchy in eccentric binary black hole mergers and associated waveform model, arXiv:2403.15506.
[182] T. Islam and T. Venumadhav, Universal phenomenological relations between spherical harmonic modes in nonprecessing eccentric binary black hole merger waveforms, Phys. Rev. D **111**, L081503 (2025).
[183] T. Islam, G. Khanna, and S. E. Field, Adding higher-order spherical harmonics in nonspinning eccentric binary black hole merger waveform models, Phys. Rev. D **111**, 124023 (2025).
[184] T. Islam, T. Venumadhav, A. K. Mehta, I. Anantpurkar, D. Wadekar, J. Roulet, J. Mushkin, B. Zackay, and M. Zaldarriaga, gwharmone: first data-driven surrogate for eccentric harmonics in binary black hole merger waveforms, arXiv:2504.12420.
[185] K. Paul, A. Maurya, Q. Henry, K. Sharma, P. Satheesh, Divyajyoti, P. Kumar, and C. K. Mishra, Eccentric, spinning, inspiral-merger-ringdown waveform model with higher modes for the detection and characterization of binary black holes, Phys. Rev. D **111**, 084074 (2025).
[186] G. Morras, G. Pratten, and P. Schmidt, Improved post-Newtonian waveform model for inspiralling precessing-eccentric compact binaries, Phys. Rev. D **111**, 084052 (2025).
[187] A. Buonanno and T. Damour, Effective one-body approach to general relativistic two-body dynamics, Phys. Rev. D **59**, 084006 (1999).
[188] A. Buonanno and T. Damour, Transition from inspiral to plunge in binary black hole coalescences, Phys. Rev. D **62**, 064015 (2000).
[189] T. Damour, P. Jaranowski, and G. Schaefer, On the determination of the last stable orbit for circular general relativistic binaries at the third post-Newtonian approximation, Phys. Rev. D **62**, 084011 (2000).
[190] S. Akcay, R. Gamba, and S. Bernuzzi, Hybrid post-Newtonian effective-one-body scheme for spin-precessing compact-binary waveforms up to merger, Phys. Rev. D **103**, 024014 (2021).
[191] R. Gamba, S. Akçay, S. Bernuzzi, and J. Williams, Effective-one-body waveforms for precessing coalescing compact binaries with post-Newtonian twist, Phys. Rev. D **106**, 024020 (2022).
[192] L. Pompili *et al.*, Laying the foundation of the effective-one-body waveform models seobnrv5: Improved accuracy and efficiency for spinning nonprecessing binary black holes, Phys. Rev. D **108**, 124035 (2023).
[193] A. Ramos-Buades, A. Buonanno, H. Estellés, M. Khalil, D. P. Mihaylov, S. Ossokine, L. Pompili, and M. Shiferaw, Next generation of accurate and efficient multipolar precessing-spin effective-one-body waveforms for binary black holes, Phys. Rev. D **108**, 124037 (2023).
[194] M. van de Meent, A. Buonanno, D. P. Mihaylov, S. Ossokine, L. Pompili, N. Warburton, A. Pound, B. Wardell, L. Durkan, and J. Miller, Enhancing the SEOBNRV5 effective-one-body waveform model with second-order gravitational self-force fluxes, Phys. Rev. D **108**, 124038 (2023).
[195] I. Hinder, B. Vaishnav, F. Herrmann, D. M. Shoemaker, and P. Laguna, Circularization and final spin in eccentric binary-black-hole inspirals, Phys. Rev. D **77**, 081502 (2008).

[196] E. A. Huerta *et al.*, Physics of eccentric binary black hole mergers: A numerical relativity perspective, Phys. Rev. D **100**, 064003 (2019).
[197] P. Schmidt, I. W. Harry, and H. P. Pfeiffer, Numerical relativity injection infrastructure, arXiv:1703.01076.
[198] V. Varma, D. Gerosa, L. C. Stein, F. Hébert, and H. Zhang, High-accuracy mass, spin, and recoil predictions of generic black-hole merger remnants, Phys. Rev. Lett. **122**, 011101 (2019).
[199] L. Blanchet, Gravitational radiation from post-Newtonian sources and inspiralling compact binaries, Living Rev. Relativity **17**, 2 (2014).
[200] A. Ramos-Buades, S. Husa, and G. Pratten, Simple procedures to reduce eccentricity of binary black hole simulations, Phys. Rev. D **99**, 023003 (2019).
[201] A. Ciarfella, J. Healy, C. O. Lousto, and H. Nakano, Eccentricity estimation from initial data for numerical relativity simulations, Phys. Rev. D **106**, 104035 (2022).
[202] T. Hinderer and S. Babak, Foundations of an effective-one-body model for coalescing binaries on eccentric orbits, Phys. Rev. D **96**, 104048 (2017).
[203] N. Warburton, S. Akcay, L. Barack, J. R. Gair, and N. Sago, Evolution of inspiral orbits around a Schwarzschild black hole, Phys. Rev. D **85**, 061501 (2012).
[204] T. Osburn, N. Warburton, and C. R. Evans, Highly eccentric inspirals into a black hole, Phys. Rev. D **93**, 064024 (2016).
[205] M. Van De Meent and N. Warburton, Fast self-forced inspirals, Classical Quantum Gravity **35**, 144003 (2018).
[206] A. J. K. Chua, M. L. Katz, N. Warburton, and S. A. Hughes, Rapid generation of fully relativistic extreme-mass-ratio-inspiral waveform templates for LISA data analysis, Phys. Rev. Lett. **126**, 051102 (2021).
[207] S. A. Hughes, N. Warburton, G. Khanna, A. J. K. Chua, and M. L. Katz, Adiabatic waveforms for extreme mass-ratio inspirals via multivoice decomposition in time and frequency, Phys. Rev. D **103**, 104014 (2021); **107**, 089901(E) (2023).
[208] M. L. Katz, A. J. Chua, L. Speri, N. Warburton, and S. A. Hughes, Fast extreme-mass-ratio-inspiral waveforms: New tools for millihertz gravitational-wave data analysis, Phys. Rev. D **104**, 064047 (2021).
[209] P. Lynch, M. van de Meent, and N. Warburton, Eccentric self-forced inspirals into a rotating black hole, Classical Quantum Gravity **39**, 145004 (2022).
[210] A. Buonanno, L. E. Kidder, A. H. Mroue, H. P. Pfeiffer, and A. Taracchini, Reducing orbital eccentricity of precessing black-hole binaries, Phys. Rev. D **83**, 104034 (2011).
[211] T. Islam and T. Venumadhav, Post-Newtonian theory-inspired framework for characterizing eccentricity in gravitational waveforms, arXiv:2502.02739.
[212] SEOBNRv4EHM, SEOBNRv4HM and SEOBNRv4PHM O3 DINGO networks, https://zenodo.org/records/13292108 ().
[213] M. Dax *et al.*, Real-time inference for binary neutron star mergers using machine learning, Nature (London) **639**, 49 (2025).
[214] M. Hannam *et al.*, General-relativistic precession in a black-hole binary, Nature (London) **610**, 652 (2022).
[215] V. Varma, S. Biscoveanu, T. Islam, F. H. Shaik, C.-J. Haster, M. Isi, W. M. Farr, S. E. Field, and S. Vitale, Evidence of large recoil velocity from a black hole merger signal, Phys. Rev. Lett. **128**, 191102 (2022).
[216] D. Davis, T. B. Littenberg, I. M. Romero-Shaw, M. Millhouse, J. McIver, F. Di Renzo, and G. Ashton, Subtracting glitches from gravitational-wave detector data during the third LIGO-Virgo observing run, Classical Quantum Gravity **39**, 245013 (2022).
[217] E. Payne, S. Hourihane, J. Golomb, R. Udall, R. Udall, D. Davis, and K. Chatziioannou, Curious case of GW200129: Interplay between spin-precession inference and data-quality issues, Phys. Rev. D **106**, 104017 (2022).
[218] D. Davis, T. J. Massinger, A. P. Lundgren, J. C. Driggers, A. L. Urban, and L. K. Nuttall, Improving the sensitivity of Advanced LIGO using noise subtraction, Classical Quantum Gravity **36**, 055011 (2019).
[219] N. J. Cornish and T. B. Littenberg, BayesWave: Bayesian inference for gravitational wave bursts and instrument glitches, Classical Quantum Gravity **32**, 135012 (2015).
[220] S. Hourihane, K. Chatziioannou, M. Wijngaarden, D. Davis, T. Littenberg, and N. Cornish, Accurate modeling and mitigation of overlapping signals and glitches in gravitational-wave data, Phys. Rev. D **106**, 042006 (2022).
[221] Glitch mitigated frames for GW200129, https://zenodo.org/record/7250495 ().
[222] R. Macas and A. Lundgren, Sensitive test of non-Gaussianity in gravitational-wave detector data, Phys. Rev. D **108**, 063016 (2023).
[223] R. Macas, A. Lundgren, and G. Ashton, Revisiting GW200129 with machine learning noise mitigation: It is (still) precessing, Phys. Rev. D **109**, 062006 (2024).
[224] S. Husa, S. Khan, M. Hannam, M. Pürrer, F. Ohme, X. Jiménez Forteza, and A. Bohé, Frequency-domain gravitational waves from nonprecessing black-hole binaries. I. New numerical waveforms and anatomy of the signal, Phys. Rev. D **93**, 044006 (2016).
[225] S. Khan, S. Husa, M. Hannam, F. Ohme, M. Pürrer, X. Jiménez Forteza, and A. Bohé, Frequency-domain gravitational waves from nonprecessing black-hole binaries. II. A phenomenological model for the advanced detector era, Phys. Rev. D **93**, 044007 (2016).
[226] B. P. Abbott *et al.* (LIGO Scientific and Virgo Collaborations), A guide to LIGO–Virgo detector noise and extraction of transient gravitational-wave signals, Classical Quantum Gravity **37**, 055002 (2020).
[227] A. Gamboa *et al.*, Accurate waveforms for eccentric, aligned-spin binary black holes: The multipolar effective-one-body model SEOBNRv5EHM, Phys. Rev. D **112**, 044038 (2025).
[228] A. Nitz *et al.*, gwastro/pycbc: v2.1.0 release of pycbc (2023).
[229] Y.-F. Wang and A. H. Nitz, Search for gravitational waves from eccentric binary black holes with an effective-one-body template, arXiv:2508.05018.
[230] N. Sanchis-Gual, C. Herdeiro, J. A. Font, E. Radu, and F. Di Giovanni, Head-on collisions and orbital mergers of Proca stars, Phys. Rev. D **99**, 024017 (2019).
[231] M. J. Graham *et al.*, Candidate electromagnetic counterpart to the binary black hole merger gravitational wave event S190521G, Phys. Rev. Lett. **124**, 251102 (2020).

[232] H. Tagawa, B. Kocsis, Z. Haiman, I. Bartos, K. Omukai, and J. Samsing, Mass-gap mergers in active galactic nuclei, Astrophys. J. **908**, 194 (2021).
[233] C. Capano, Y. Pan, and A. Buonanno, Impact of higher harmonics in searching for gravitational waves from nonspinning binary black holes, Phys. Rev. D **89**, 102003 (2014).
[234] V. Varma, P. Ajith, S. Husa, J. C. Bustillo, M. Hannam, and M. Pürrer, Gravitational-wave observations of binary black holes: Effect of nonquadrupole modes, Phys. Rev. D **90**, 124004 (2014).
[235] C. Van Den Broeck and A. S. Sengupta, Binary black hole spectroscopy, Classical Quantum Gravity **24**, 1089 (2007).
[236] C. Van Den Broeck and A. S. Sengupta, Phenomenology of amplitude-corrected post-Newtonian gravitational waveforms for compact binary inspiral. I. Signal-to-noise ratios, Classical Quantum Gravity **24**, 155 (2007).
[237] T. B. Littenberg, J. G. Baker, A. Buonanno, and B. J. Kelly, Systematic biases in parameter estimation of binary black-hole mergers, Phys. Rev. D **87**, 104003 (2013).
[238] M. Dall'Amico, M. Mapelli, S. Torniamenti, and M. A. Sedda, Eccentric black hole mergers via three-body interactions in young, globular and nuclear star clusters, Astron. Astrophys. **683**, A186 (2024).
[239] J. Samsing, Eccentric black hole mergers forming in globular clusters, Phys. Rev. D **97**, 103014 (2018).
[240] J. N. Bahcall and R. A. Wolf, Star distribution around a massive black hole in a globular cluster, Astrophys. J. **209**, 214 (1976).
[241] J. N. Bahcall and R. Wolf, The star distribution around a massive black hole in a globular cluster. ii unequal star masses, Astrophys. J. **216**, 883 (1977).
[242] J. Miralda-Escude and A. Gould, A cluster of black holes at the galactic center, Astrophys. J. **545**, 847 (2000).
[243] C. J. Hailey, K. Mori, F. E. Bauer, M. E. Berkowitz, J. Hong, and B. J. Hord, A density cusp of quiescent x-ray binaries in the central parsec of the galaxy, Nature (London) **556**, 70 (2018).
[244] I. Bartos, B. Kocsis, Z. Haiman, and S. Márka, Rapid and bright stellar-mass binary black hole mergers in active galactic nuclei, Astrophys. J. **835**, 165 (2017).
[245] N. C. Stone, B. D. Metzger, and Z. Haiman, Assisted inspirals of stellar mass black holes embedded in AGN discs: Solving the 'final au problem', Mon. Not. R. Astron. Soc. **464**, 946 (2017).
[246] B. McKernan, K. E. S. Ford, and R. O'Shaughnessy, Black hole, neutron star, and white dwarf merger rates in AGN discs, Mon. Not. R. Astron. Soc. **498**, 4088 (2020).
[247] C. Rowan, T. Boekholt, B. Kocsis, and Z. Haiman, Black hole binary formation in AGN discs: From isolation to merger, Mon. Not. R. Astron. Soc. **524**, 2770 (2023).
[248] M. Rozner, A. Generozov, and H. B. Perets, Binary formation through gas-assisted capture and the implications for stellar, planetary, and compact object evolution, Mon. Not. R. Astron. Soc. **521**, 866 (2023).
[249] J. Li, A. M. Dempsey, H. Li, D. Lai, and S. Li, Hydrodynamical simulations of black hole binary formation in AGN disks, Astrophys. J. Lett. **944**, L42 (2023).
[250] K. E. S. Ford and B. McKernan, Binary black hole merger rates in AGN discs versus nuclear star clusters: Loud beats quiet, Mon. Not. R. Astron. Soc. **517**, 5827 (2022).
[251] A. Rasskazov and B. Kocsis, The rate of stellar mass black hole scattering in galactic nuclei, Astrophys. J. **881**, 20 (2019).
[252] L. Gondán and B. Kocsis, Measurement accuracy of inspiraling eccentric neutron star and black hole binaries using gravitational waves, Astrophys. J. **871**, 178 (2019).
[253] D. Chattopadhyay, J. Stegmann, F. Antonini, J. Barber, and I. M. Romero-Shaw, Double black hole mergers in nuclear star clusters: eccentricities, spins, masses, and the growth of massive seeds, Mon. Not. R. Astron. Soc. **526**, 4908 (2023).
[254] P. Amaro-Seoane and X. Chen, Relativistic mergers of black hole binaries have large, similar masses, low spins and are circular, Mon. Not. R. Astron. Soc. **458**, 3075 (2016).
[255] J. M. Antognini, B. J. Shappee, T. A. Thompson, and P. Amaro-Seoane, Rapid eccentricity oscillations and the mergers of compact objects in hierarchical triples, Mon. Not. R. Astron. Soc. **439**, 1079 (2014).
[256] M. C. Miller and V. M. Lauburg, Mergers of stellar-mass black holes in nuclear star clusters, Astrophys. J. **692**, 917 (2009).
[257] C. Petrovich and F. Antonini, Greatly enhanced merger rates of compact-object binaries in non-spherical nuclear star clusters, Astrophys. J. **846**, 146 (2017).
[258] C. L. Rodriguez and A. Loeb, Redshift evolution of the black hole merger rate from globular clusters, Astrophys. J. Lett. **866**, L5 (2018).
[259] C. L. Rodriguez, K. Kremer, S. Chatterjee, G. Fragione, A. Loeb, F. A. Rasio, N. C. Weatherford, and C. S. Ye, The observed rate of binary black hole mergers can be entirely explained by globular clusters, Res. Notes AAS **5**, 19 (2021).
[260] K. Kremer, C. S. Ye, N. Z. Rui, N. C. Weatherford, S. Chatterjee, G. Fragione, C. L. Rodriguez, M. Spera, and F. A. Rasio, Modeling dense star clusters in the milky way and beyond with the CMC cluster catalog, Astrophys. J. Suppl. Ser. **247**, 48 (2020).
[261] U. N. Di Carlo *et al.*, Binary black holes in young star clusters: The impact of metallicity, Mon. Not. R. Astron. Soc. **498**, 495 (2020).
[262] S. Banerjee, Merger rate density of stellar-mass binary black holes from young massive clusters, open clusters, and isolated binaries: Comparisons with LIGO-Virgo-KAGRA results, Phys. Rev. D **105**, 023004 (2022).
[263] F. Santoliquido, M. Mapelli, Y. Bouffanais, N. Giacobbo, U. N. Di Carlo, S. Rastello, M. C. Artale, and A. Ballone, The cosmic merger rate density evolution of compact binaries formed in young star clusters and in isolated binaries, Astrophys. J. **898**, 152 (2020).
[264] M. Mapelli, N. Giacobbo, E. Ripamonti, and M. Spera, The cosmic merger rate of stellar black hole binaries from the illustris simulation, Mon. Not. R. Astron. Soc. **472**, 2422 (2017).
[265] L. A. C. van Son, S. E. de Mink, T. Callister, S. Justham, M. Renzo, T. Wagg, F. S. Broekgaarden, F. Kummer, R. Pakmor, and I. Mandel, The redshift evolution of the

binary black hole merger rate: A weighty matter, Astrophys. J. **931**, 17 (2022).

[266] M. Mapelli, Y. Bouffanais, F. Santoliquido, M. A. Sedda, and M. C. Artale, The cosmic evolution of binary black holes in young, globular, and nuclear star clusters: Rates, masses, spins, and mixing fractions, Mon. Not. R. Astron. Soc. **511**, 5797 (2022).

[267] E. Payne, C. Talbot, and E. Thrane, Higher order gravitational-wave modes with likelihood reweighting, Phys. Rev. D **100**, 123017 (2019).

[268] E. Thrane and C. Talbot, An introduction to Bayesian inference in gravitational-wave astronomy: Parameter estimation, model selection, and hierarchical models, Pub. Astron. Soc. Aust. **36**, e010 (2019); **37**, e036(E) (2020).

[269] M. Ruiz, R. Takahashi, M. Alcubierre, and D. Nunez, Multipole expansions for energy and momenta carried by gravitational waves, Gen. Relativ. Gravit. **40**, 2467 (2008).

[270] M. Campanelli, C. O. Lousto, Y. Zlochower, and D. Merritt, Maximum gravitational recoil, Phys. Rev. Lett. **98**, 231102 (2007).

[271] B. Bruegmann, J. A. Gonzalez, M. Hannam, S. Husa, and U. Sperhake, Exploring black hole superkicks, Phys. Rev. D **77**, 124047 (2008).

[272] M. Radia, U. Sperhake, E. Berti, and R. Croft, Anomalies in the gravitational recoil of eccentric black-hole mergers with unequal mass ratios, Phys. Rev. D **103**, 104006 (2021).